# General Disclaimer

One or more of the Following Statements may affect this Document

- This document has been reproduced from the best copy furnished by the organizational source. It is being released in the interest of making available as much information as possible.

- This document may contain data, which exceeds the sheet parameters. It was furnished in this condition by the organizational source and is the best copy available.

- This document may contain tone-on-tone or color graphs, charts and/or pictures, which have been reproduced in black and white.

- This document is paginated as submitted by the original source.

- Portions of this document are not fully legible due to the historical nature of some of the material. However, it is the best reproduction available from the original submission.
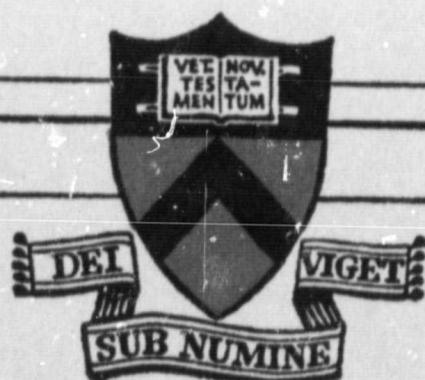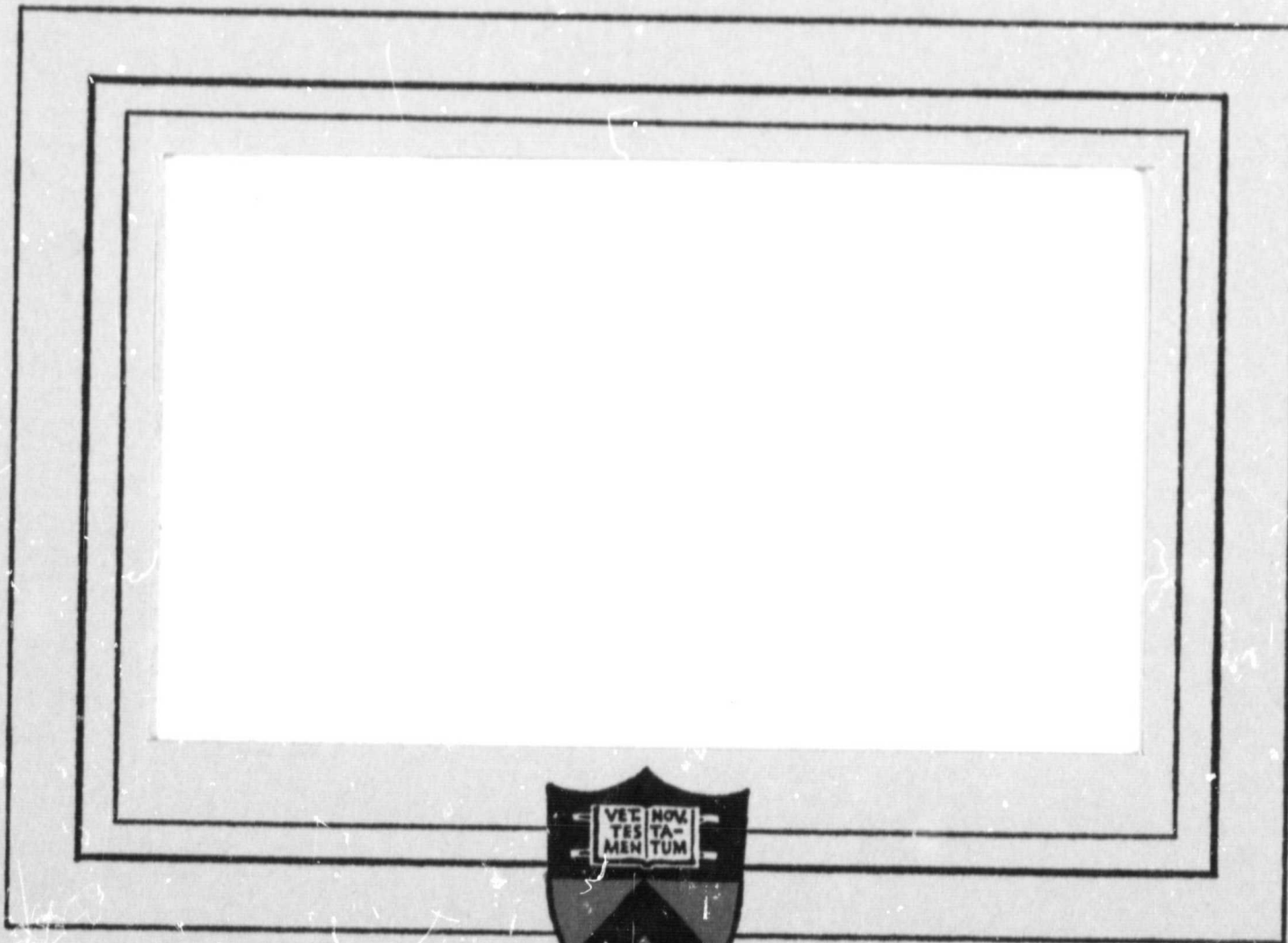
Produced by the NASA Center for Aerospace Information (CASI)

PRINCETON UNIVERSITY

DEPARTMENT OF

AEROSPACE AND MECHANICAL SCIENCES

Prepared for
National Aeronautics
and Space Administration

PRESSURE DISTRIBUTION IN

THE STRUCTURE OF A

PROPAGATING CURRENT SHEET

Report 853*

Prepared by _____ *Thomas M. York*
            Thomas M. York

Approved by _____ *Robert G. Jahn*
            Robert G. Jahn
            Professor of Aerospace Sciences
            and Research Leader

*This report is a reproduction in entirety of the Ph.D. disser-
tation of Mr. Thomas M. York. It is submitted to the sponsor
and to the distribution list in this form both as a presentation
of the technical material, and as an indication of the academic
program supported by this Grant.

December 1968

School of Engineering and Applied Science
Department of Aerospace and Mechanical Sciences
Guggenheim Aerospace Propulsion Laboratories
PRINCETON UNIVERSITY
Princeton, New Jersey

ABSTRACT

The structure of a current sheet propagating into ambient argon is studied experimentally and analytically. The current sheet in a linear z-pinch device is examined experimentally with a specialized high-speed pressure transducer, magnetic, electric and voltage probes, along with the photography of discharge luminosity. The pressure probe is used to measure profiles of axial and radial pressure at a single point in the chamber; this data is time-correlated with electric and magnetic field profiles.

The experimental results indicate a discontinuous compression followed by a sharp expansion within the sheet structure. From reduced profiles of pressure, current density, along with electric and magnetic fields, several distinct zones are definable within the sheet; in sequence, regions of electron current conduction (I), mass accumulation (II), and induced flow of unswept gas (III) are dominant. Profiles of particle density, temperature, and velocity are evaluated. From these results, ions are identified as the current carriers in the rear of the sheet (II). The current sheet is found to entrain a large percentage of gas. A balance of momentum and energy is carried out, with the resultant identification of loss mechanisms. The distributions of current and mass densities within the sheet do not agree with proposed piston-shock wave models; however, they do indicate the dominant mechanisms within each of the sheet regions, providing a more exact basis for theoretical analysis of current sheet structure.

TABLE OF CONTENTS

LIST OF ILLUSTRATIONS

LIST OF ILLUSTRATIONS--contd.

1

CHAPTER 1

INTRODUCTION

The techniques of pulsed plasma acceleration have demonstrated unique potential for application to the problem of high performance space propulsion. The development of such a propulsion system, however, will require a detailed understanding of the interaction of a transient electromagnetic discharge with a low density gas. The difficulties involved in reaching this understanding are perhaps most clearly illustrated by noting similarities of the pulsed electric propulsion problem with those of the yet unsolved controlled thermonuclear reaction problem. Clearly, the goals of the fusion effort are the containment and heating of a gas, whereas gas acceleration and ejection are the objectives in any propulsion system. Yet both of these applications utilize the same type of electromagnetic mechanism: large discharge currents interacting with their self-induced magnetic fields. The objective of a transient plasma propulsion device is to attempt to exploit the inherently rapid transfer of stored electrical energy to a gas propellant in such a manner that will optimize the energy in directed gas motion.

A number of both pinch and rail devices have been developed in order to study the electromagnetic interaction

mechanism. Typically these devices produce a diffuse "sheet"
discharge which propagates through the ambient gas, but the de-
tails of this sweeping process are not yet clearly understood.
For an accelerator system the critical questions are how the
current sheet interacts with the overrun gas and, most impor-
tantly, how much ambient gas becomes entrained within the sweep-
ing sheet. These are the questions to which this work is
addressed.

Earlier work directed toward analyzing current sheet
interaction has progressed from the consideration of overall
sheet dynamics, to internal sheet structure, to the combined
structure and dynamics problem. In each of these cases a model
was presumed that predicted mass distribution within the sheet
system, but exact experimental confirmation of this important
variable was not possible because of the resolution of avail-
able instruments. Specifically, the earliest model, proposed
by Rosenbluth [1], was that of the current sheet acting as an
impermeable piston. As such, it was envisioned as sweeping up
all the gas it encountered and compressing it into a thin layer
on the piston surface; this has been picturesquely referred to
as the "snowplow" model. It allows for conservation of mass
to be satisfied and uses conservation of momentum to relate the
driving j x B mechanism to sheet dynamics. For all its sim-
plicity, it has been found to be in general agreement with ex-
perimental sheet trajectories. With this agreement came accep-
tance of the concept of a current sheet piston; the logical
extension of the model to include finite compressibility of the

gas and the related piston driven shock waves was also developed (e.g., [2]). However, some experimental evidence of mass distribution became available [3] with the declassification of fusion research and publication of Russian work in this field. Attempts at measuring pressures in a dynamic z-pinch experiment using piezoelectric probes did not indicate pressure discontinuities preceding the current sheet but _following_ the current conduction zone, at variance with the concept of a current sheet piston driving a shock. The current sheet interaction problem received more careful attention from such workers as Lovberg (e.g., [4,5]), who attempted to develop a more consistent experimental-analytical sheet structure model. However, in this work mass distribution was still inferred from electromagnetic measurements. In an attempt to develop a more compatible sheet structure, the pressure sensing technique mentioned earlier [3] was incorporated into a generally self-consistent study of current sheets by Vlases [6,7], Sorrell [8], and Hoffman [9]. The instruments used suffered from lack of absolute resolution and only time of arrival of the pressure discontinuity was felt to be acceptable. The approach used was one of varying gas type and discharge parameters affecting the sheet dynamics in an attempt to achieve sheet-shock separation. A broad consideration of the current sheet interaction problem has also been carried out at Princeton by Jahn and his group (e.g., [10 to 14]). Specifically, the work of Black [12] established the relevance of the snowplow formulation for dis-

charges driven by pulse-forming networks. A detailed experimental study using electric and magnetic probes provided the basis for a sheet structure model proposed by Burton [13]. Further, an experimental study of the current sheet using reflected microwave measurements resulted in a prediction of current partition by Ellis [14].

While the understanding of dynamic electrical discharges has been significantly enhanced by recent efforts, it is clear that no approach is yet self-consistently complete. Rather, it is evident from each analysis that a knowledge of mass distribution would immeasurably aid the proper formulation of the sheet structure. Unfortunately, as implied above, standard density sensing techniques are not satisfactory for sheet diagnostics, typically because of such effects as the high degree of nonequilibrium or probing sensitivity to electron rather than heavy particle behavior.

In this perspective, the application of pressure sensing technique to the mass distribution problem appears most promising. The significance of determining the distribution of pressure within the current sheet lies clearly in its relationship to particle density and velocity distributions. Accordingly, the work to be presented will detail the development of a pressure sensing device with satisfactory resolution, its use in probing the current sheet environment, and the development of a current sheet model that is consistent with the observed distributions of pressure.

CHAPTER 2

APPARATUS AND EXPERIMENTAL PARAMETERS

2.1 INTRODUCTION

The study of dynamic current sheets will be based on
detailed experimental results. While a number of devices are
capable of providing gas accelerating discharges [15], the
large-radius linear pinch discharge was chosen for the present
investigation because of its conceptual simplicity and experi-
mental convenience. The discharge chamber was of a cylindri-
cal shape with electrode end walls and insulator sidewalls.
A voltage applied across the electrodes produced a uniform
cylindrical discharge at the outer radius which collapsed
toward the center by self-field j x B interaction. This device
has been shown to provide a vigorous highly-reproducible dis-
charge pattern, an optimum configuration for conservation of
magnetic flux, accessibility of the current sheet to probing,
and a discharge geometry that is analytically simple.

2.2 DISCHARGE APPARATUS

The main components of the discharge apparatus were
the cylindrical discharge chamber mentioned above, a gas-trig-
gered switch, and a capacitor bank distributed along a trans-
mission line. The particular system used during the experiments

resulted from a study of pulse-forming networks and has been described in detail elsewhere [12]. The ability to alter the circuit current waveform in this machine from the standard lumped bank sinusoidal waveform was a significant element in generating an optimum current sheet for study. Briefly, (Fig. 2-1), the discharge chamber was 8 inches in diameter and 2 inches high. The electrodes of 3/4-in. thick aluminum were separated by a 1/4-in. thick Pyrex sidewall. Both the outer (ground) electrode and the sidewalls were fitted to accept various internal probes. The switch unit [16] was also a pinch chamber, similar to that of the main discharge except for a Plexiglas insert to inhibit complete pinching. The switch operated by providing an open circuit when the internal pressure was maintained below a few microns; the discharge was initiated by injecting a puff of gas which allowed switch breakdown and transfer of the bank potential to the main chamber. The electrical energy was stored in a bank of 20 capacitor units with nominal 2.5 µf capacitance and 15 nh inductance, rated to 10 kv. The apparatus utilized a transmission line consisting of a pair of opposed sets of parallel plates to which the capacitors were connected. The transmission line was fitted with 40 linearly spaced capacitor stations so that the circuit current waveform could be controlled by varying circuit inductance through capacitor positions.

2.3 SUPPORTING EQUIPMENT

The operation of the pinch discharge apparatus required
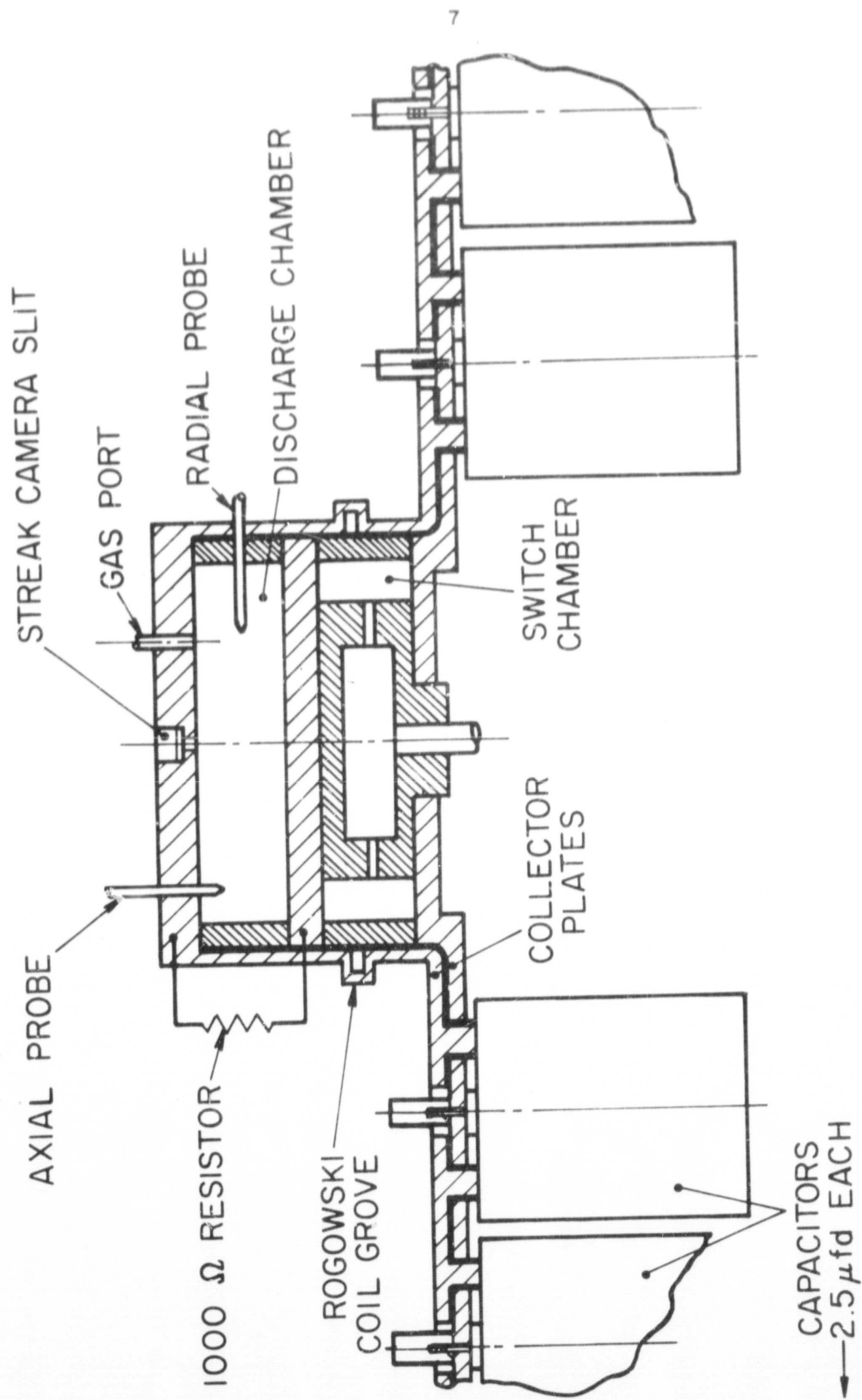
EXPERIMENTAL APPARATUS (SCHEMATIC)

FIGURE 2-1

AP25 - 4250 - 67

several support components. The system was operated at low
pressures and the vacuum was maintained by a mechanical pump;
a working limit of several microns was standard. System pres-
sures were monitored with a standard Pirani gauge with a range
of 1 to 2000 μ Hg; it was periodically calibrated against a
McLeod gauge to insure its accuracy. Data was generally re-
corded photographically from Tektronix Type 555 dual-beam os-
cilloscopes using Type L and G plug-in units to preamplify the
signals.

The intensity of the discharge resulted in the radi-
ation of high-frequency "noise" signals and lower frequency
shifts in ground potential. In order to record undistorted
data, a number of precautions had to be taken. Generally, all
probe leads were shielded coaxial cable having characteristic
impedances of 50, 93, or 185 ohms. The use of termination
with these cables to avoid spurious internal oscillations was
determined by signal strength and signal-to-noise ratio. The
oscilloscopes themselves had to be shielded from this spurious
radiation by enclosing them within a metal-screened Faraday
cage. In order to maintain an absolute ground, it was necessary
to connect both the discharge chamber and screen room to sepa-
rate, direct ground connections. Further, to avoid a low-fre-
quency ground circuit oscillation, the chamber and screen room
were connected by a short length of solid #8 cable, effectively
substituting as a ground plane connection.

2.4 GAS DISCHARGE CONDITIONS

The selection of an appropriate gas and ambient chamber pressure was carried out essentially on the basis of particle energy considerations. In order to clearly establish the possible modes of internal energy absorption and excitation, the atomic noble gases are more appropriate than molecular gases. Further, on the basis of the plasma propulsion application, the relatively high molecular weight of argon and low ionization potential (15.75 ev) makes it an attractive choice. Regarding the pressure range of interest, it was found [12 to 14] that discharges of the 50 µf capacitor bank charged to 10 kv into ambient argon of 100 µ Hg ambient pressure produced discharges with sharply peaked current density profiles and 3 to 5 µsec pinch times; and accordingly, these conditions were selected as most appropriate.

2.5 GENERAL CIRCUIT CHARACTERISTICS

The characteristics of the discharge apparatus can be described most clearly by comparing the average circuit parameters for the components. As summarized by Black [13] for a low pressure argon discharge:

Unit capacitance.	2.5 µf
Inductance of capacitor unit.	15 nanohenry
Line station-to-station inductance. .	12 nanohenry
Switch and network resistance	5 milliohm
Discharge plus switch inductance. . .	5 nanohenry
Discharge impedance	5 milliohm

The capacitor units were connected into the transmission line to form an LC ladder network with an impedance of approximately 100 nanohenry. Clearly, the effective inductance of the network was primarily reactive rather than resistive. Further, because the network inductance far exceeded the chamber inductance, the circuit behavior was effectively decoupled from the dynamics of the pinch discharge.

The shot-to-shot behavior of the discharge circuit was monitored by recording measurements of circuit current waveform with a Rogowski coil of standard design [17]. The coil was placed around the outer circumference of the discharge chamber and so produced a signal proportional to dI/dt, the time rate of change of circuit current. Circuit current was then obtained by use of a passive RC integrator circuit. The calibration of the Rogowski coil was carried out by discharging a lumped capacitor configuration to produce a damped RLC circuit. From known voltage and capacitance and measured frequency and damping constant, the calibration factor was inferred.

2.6 THE CIRCUIT CURRENT WAVEFORM

As noted above, the discharge of a lumped capacitor bank into the pinch discharge chamber would produce a damped sinusoidal ringdown of the familiar RLC circuit. However, it is possible for the pinch time to be greater than the half cycle of the ringdown, depending upon the gas type and pressure in the chamber. It has been shown [12] that if the circuit current reverses during the current sheet implosion, a secondary

breakdown will occur at the outer radius and decouple the primary sheet from the driving circuit. It has further been noted [12] that a slowly-rising driving waveform does not produce an intense, vigorous discharge. On this basis, a fast-rising waveform that does not reverse prior to pinch is required to study actively driving sheets. It is possible to meet these restrictions with a low-inductance lumped-bank discharging into a small (5 in.) diameter chamber with 120 μ argon as demonstrated by Burton [13]. For a larger diameter chamber, it is necessary to distort the sinusoidal waveform to avoid "crowbarring" a second sheet. The μ-wave current sheet study carried out by Ellis [14] in an 8-in. diameter machine with 100 μ argon driven by a 50 μf pulse-forming network utilized a constant-current waveform. While the constant current waveform is analytically convenient, it has been found to result in severe distortions of the imploding sheet. Specifically, the anode foot, or bifurcation, phenomenon [18] is dominant with this pulse, along with a high degree of irreproducibility in time of arrival of the current sheet [14]. An indication of such behavior can be seen by considering the expression for constant total (circuit) current as a function of sheet thickness (δ) and current density (j),

$$I \approx 2\pi R \cdot \delta \cdot j$$

For an imploding sheet, R decreases with time, and accordingly δ and/or j must increase with time; experimental evidence indicates a significant broadening of the current sheet with radius.

In order to avoid such difficulties, the pulse-forming network was used to drive a circuit current that first rose sharply and then decreased linearly until pinch (Fig. 2-2). This waveform was found to produce a thin, intense sheet that maintained approximately constant current density profiles over its incursion at constant velocity. Such behavior indicates $I \propto R$, and so the constant current density profile is in complete agreement with the above analytical outline. The detailed behavior of this current sheet will be considered again in a more appropriate context.

$I(1.78 \times 10^5 \text{ AMP/Div})$

$\frac{dI}{dt} (6.0 \times 10^{11} \frac{\text{AMP/SEC}}{\text{DIV}})$

T-3641

1 μsec

CIRCUIT CURRENT WAVE FORM

FIGURE 2-2
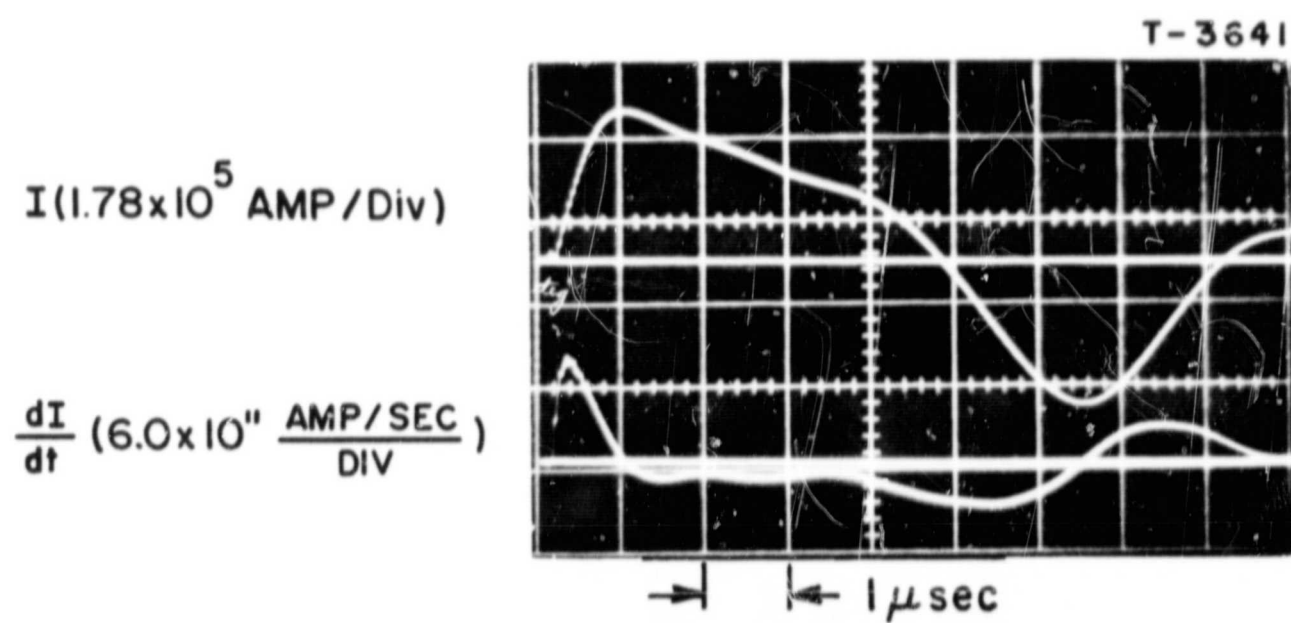
CHAPTER 3

PRESSURE PROBE DEVELOPMENT

3.1 INTRODUCTION

A pressure sensing device that can be used within an electrical discharge apparatus must meet several stringent requirements. It must be electrically insulated from the plasma environment and yet be capable of providing a signal free of stress distortion; further, it must produce a signal of sufficient strength so that it will not be distorted by spurious electromagnetic pickup. Using standard transducing techniques, there are several types of instruments that can possibly be used in this environment. A state-of-the-art survey of this subject has recently been published by Jones and Vlases [19] and so a detailed discussion of the mechanical characteristics of each will not be presented here. However, it is of interest to evaluate the performance of these probes for possible application.

The event that is being investigated has been found to occur [13,14] on the time and space scales of 1 μsec and 1 cm, i.e., sheet velocities of the order of 10^4 m/sec. Strong shock wave approximations for a shock driven under these conditions indicate static pressure changes on the order of one atmosphere. In order to probe such a discontinuity effectively,

measurements both transverse and normal to the sweeping sheet
are necessary. Ideally then, a probe with a dimension of 1 mm
and rise time of 0.1 µsec is indicated. Needless to say, such
a device is not commercially available and so design of a
specialized instrument must be considered.

The capacitive gauge noted by Vlases [19] has a satis-
factory rise time and response period, but was designed for use
normal to a discontinuity and would not be useful to probe a
transversely sweeping sheet because of induced internal stresses.
Further, experiments with a 1/2-in. diameter capacitive device
indicated a poor signal-to-noise ratio.

The pressure-bar gauge as a plasma sensing device was
first utilized by Stern and Dacus [20]. The active transducing
element is a wafer of piezoelectric material bonded between rods
of acoustically matched material. The pressure pulse is picked
up at the end of a cylindrical rod, transmitted along the rod
to the crystal, and passes through to the backing rod section.
This gauge has a very significant advantage of small electro-
magnetic pickup due to the crystal-discharge separation, but
also suffers the severe disadvantage of signal delay and dis-
persion within the initial section of the acoustically conduct-
ing bar. Some limits on the distortion due to three-dimensional
effects have been noted in the literature [17], and the distor-
tion due to thermal stresses have been analyzed by Measures [21].
The use of such a device in an inverse pinch has been reported
by Katsaros [22]. In any case, in order to resolve the internal

structure of a current sheet by simultaneous measurements, the probes must operate with acceptable real-time delays of less than 10^{-7} sec and so the pressure bar probe cannot meet the demands of the present application.

In order to meet the above requirements on time resolution, the sensing element must obviously be in close contact with the plasma. Accordingly, the direct-contact piezo-pressure gauge appears most appropriate for sheet diagnostics. The difficulties associated with this type of probe remain those of providing adequate insulation and of generating sufficient signal strength. Specifically, the sensing surface has usually been insulated by relatively thick coverings of Pyrex [6,23] or metal and insulator [24], resulting in real-time signal delays on the order of several tenths of microseconds and internal stress oscillations that distort the signal beyond time of arrival [19]. However, if it were possible to control and predict the internal probe oscillations and if an insulation were developed that produced negligible signal delay, the direct contact probe could be used to provide the desired record of pressures within the current sheet. With this objective, the direct-contact piezo-pressure probe was selected for detailed study and development.

3.2 PROBE CONSTRUCTION AND CIRCUITRY

The general configuration for the direct-contact pressure probe has been discussed in the literature cited and will simply be summarized here. Further, for the details of the

physics of the piezoelectric effect and typical applications, the interested reader is referred to the arch ve literature [25,26]. Again, the basic components of this device are a piezoelectric element, a backing rod, an outer conductor shell, and an outer insulator shell (Fig. 3-1). The construction is completely coaxial with the piezo element enclosed within a grounded shell to avoid spurious signal pickup.

The transducing element in the probe system is the piezo-electric element. Basically, a piezoelectric material responds to a change in the stress (pressure) applied to its surface by generating a proportionate electrical charge over certain crystal faces. For the present application, a piezo element was chosen that produces charge separation across the 1—2 plane (Fig. 3-1) due to pressures normal to that surface. The charge generated can be expressed as

$$Q_s = d_{33} \cdot A_p \cdot \Delta P \qquad (3-1)$$

where d_{33} is the piezoelectric modulus (a material constant) and A_p is the crystal surface area on which ΔP is applied. Accordingly, the piezoelectric material, together with the two conducting surfaces, constitutes a capacitor with

$$C_s = \frac{\epsilon A_s}{d} = \frac{(K_s \cdot \epsilon_o) A_s}{d} \qquad (3-2)$$

where ϵ is the crystal permittivity, K_s is the dielectric constant, d is the crystal thickness and A_s is the surface area of the capacitor (crystal) electrodes. The equivalent electrical
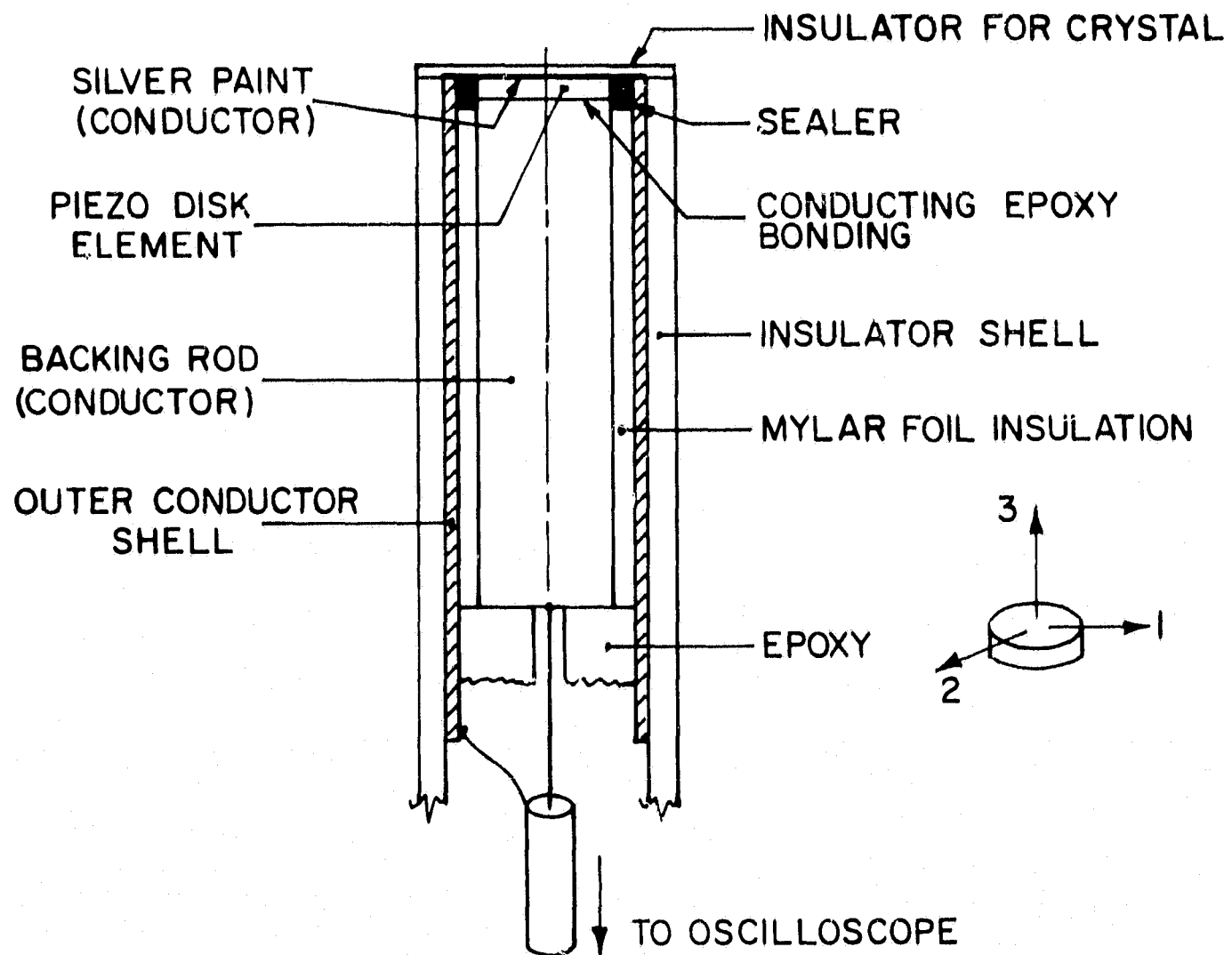
SCHEMATIC OF PIEZOELECTRIC PRESSURE TRANSDUCER

FIGURE 3-1

circuit for the piezo element is represented in Fig. 3-2 as a source across a crystal capacitance, C_s, and shunt leakage resistance, R_s. Accordingly, the crystal appears as a generator of emf across its terminals, as

$$V_s = \frac{Q_s}{C_s} = g_{33} \cdot d \cdot \Delta P \cdot \frac{A_p}{A_s} \tag{3-3}$$

where $g_{33} = d_{33}/\in$ is a "reduced" piezoelectric modulus. The probe can be represented in its circuit with a length of coaxial cable (subscript c) and oscilloscope input parameters (subscript L) as shown in Fig. 3-3. The output of the complete probe-cable-oscilloscope system can then be expressed as

$$V_L = V_s \cdot \frac{C_s}{C_s + C_L + C_c} = V_s \times F_R \tag{3-4}$$

where F_R is defined as an effective output reduction factor. From the above outline, it can be seen that while crystal output is directly proportional to thickness, the measurable system output also has a direct relationship to the crystal area through the capacitance. The crystal thickness must be dictated by the desirable rise-time which is directly related to acoustic velocity and thickness in the one-dimensional approximation, i.e., $t(\text{rise-time}) = d/a_s$. Accordingly, the surface area of the sensing surface must be compromised for signal output. On the basis of an attractively high piezoelectric constant, the ceramic material PZT-5 (lead, zirconate, titanate) was selected as optimum from the number of materials available from Clevite Corporation, Piezoelectric Division. The relevant crystal
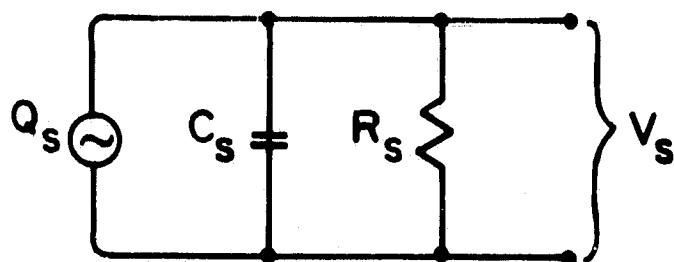
EQUIVALENT CIRCUIT OF PIEZOELECTRIC ELEMENT

FIGURE 3-2
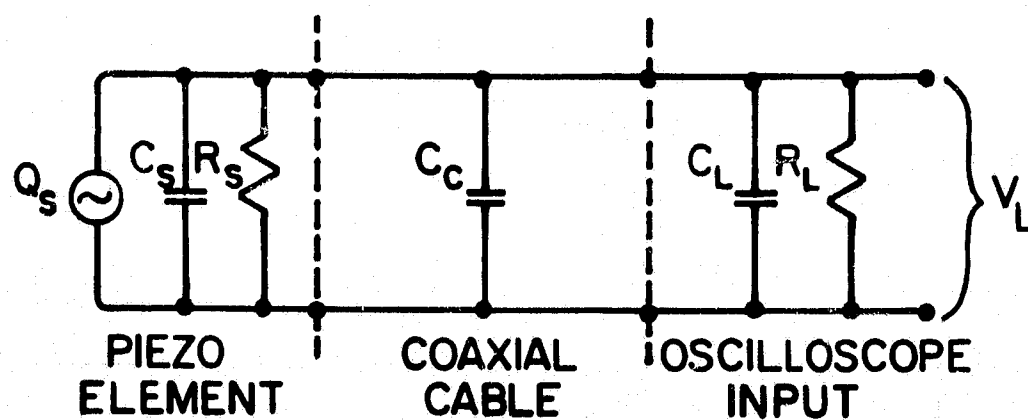
EQUIVALENT CIRCUIT OF PIEZO PROBE SYSTEM

FIGURE 3-3

properties as summarized from specifications [27] are

Piezoelectric
coefficient. . . . . . $g_{33} = 24.8 \times 10^{-3}$ volt-m/newton

Dielectric
constant . . . . $K_3 = 1700$

Youngs modulus . . . . . $Y_{33} = 5.3 \times 10^{10}$ newton/m^2

Poisson's ratio. . . . . $\nu = 0.30$

Density. . . . . $\rho = 7.7 \times 10^3$ kg/m^3

Resistivity. . . . . . . $\rho_R > 10^{11}$ ohm-m

With the above parameters the following calculations can be

made to determine the appropriate crystal dimensions:

Acoustic
velocity . . . . $a_s = (Y_{33}/\rho)^{\frac{1}{2}} = 2.63 \times 10^3$ m/sec

Crystal
thickness. . . . $d = t \cdot a_s = 2.63 \times 10^{-4}$ m = 0.0104 in.

                            for t = 0.1 μsec rise-time

Crystal output
(ideal). . . . . $V_s/\triangle P = g_{33} \cdot d = 0.64$ volts/atm

Cable capacitance. $C_c = 150$ μ μf for 5 ft of RG-58

Oscilloscope
capacitance. . . $C_L = 50$ μ μf for G preamp

Since the effective crystal capacitance and crystal output were

found to diminish by a factor of 2 in the process of probe fab-

rication, an acceptable reduction factor, $F_R = 0.66$ was chosen

to fix the probe system output at, $V_L/\triangle P = 0.2$ v/atm. Then

C_s (effective) . . . . . $= 400$ μ μf for $F_R = 0.66$

C_s (ideal) . . . . . . $= 2 C_s$ (effective) = 800 μ μf

so

$$A_s = \frac{C_s \cdot d}{K_s \cdot \epsilon_o} = 1.4 \times 10^{-5} \ m^2$$

and

$$Diam.(s) = 4 \ mm = 5/32 \ inches$$

Further, the effective time constant for the equivalent circuit can be estimated, RC(effective) $\approx$ 600 μsec, considerably exceeding the requirements for a several microsecond event.

Regarding the resolution of the above device, it is evident that a sensing element of this size is not optimum for probing the anticipated 1.8 cm thick current sheet. However, it is within reasonable limits for establishing general profiles when the anticipated transverse and normal orientations can be used in conjunction. Further, should the anticipated discontinuity in the density appear within the current sheet, the resolution of the probe could be extended by the proportionality of the output to the applied force with an estimation of the area swept by the discontinuity.

3.3 PROBE RESPONSE AND INTERNAL STRESS DYNAMICS

The response of a piezoelectric pressure probe is directly proportional to the stress within the sensing element. The use of such a device in a transient loading situation requires a knowledge of the internal stress dynamics, i.e., a knowledge of the dynamics of stress waves that will propagate within the probe structure itself. The archive literature

[28, 29] may be consulted for details of such considerations. Ideally, in the one-dimensional approximation (Fig. 3-4), a stress, σ , applied at the surface of a solid rod will produce a compression that will be transmitted along the rod with velocity $a_1 = (E_1/\rho_1)^{1/2}$, inducing particle velocity $v_1 = a_1 \sigma E^{-1} = \sigma(E_1 \rho_1)^{-1/2}$. The variable, $(E_1 \rho_1)^{1/2} \equiv z_1$, has been termed the acoustic impedance. Such a stress wave propagating from medium 1 to medium 2 must satisfy the boundary conditions at the interface that $\sigma_1 = \sigma_2$ and $v_1 = v_2$. Accordingly, it can be shown [25] that the ratio of the reflected to the transmitted stress can be expressed

$$\frac{\sigma_{1R}}{\sigma_{1T}} = \frac{r - 1}{r + 1} \qquad \text{where} \quad r = \frac{z_2}{z_1} \qquad (3-5)$$

In the present application, the function of the backing rod, 2, is to allow the stress wave to propagate completely out of the crystal, 1, and so to avoid internal stress oscillations. On the basis of the above analysis, this should be accomplished by matching the acoustic impedance of the two elements, a basic criterion which has been applied to piezo-probes since their introduction [3].

In an attempt to determine basic probe response and to evaluate the interaction between the piezo element and the backing rod material, probes were constructed using both brass and tin as backing rod materials. Brass matched the crystal impedance only roughly, while tin provided a much more exact
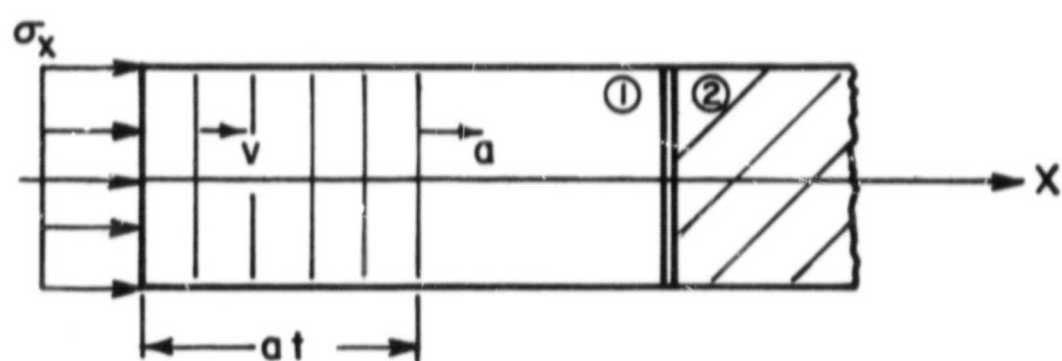
ONE−DIMENSIONAL STRESS MODEL

FIGURE 3− 4

CRYSTAL .020" THICK
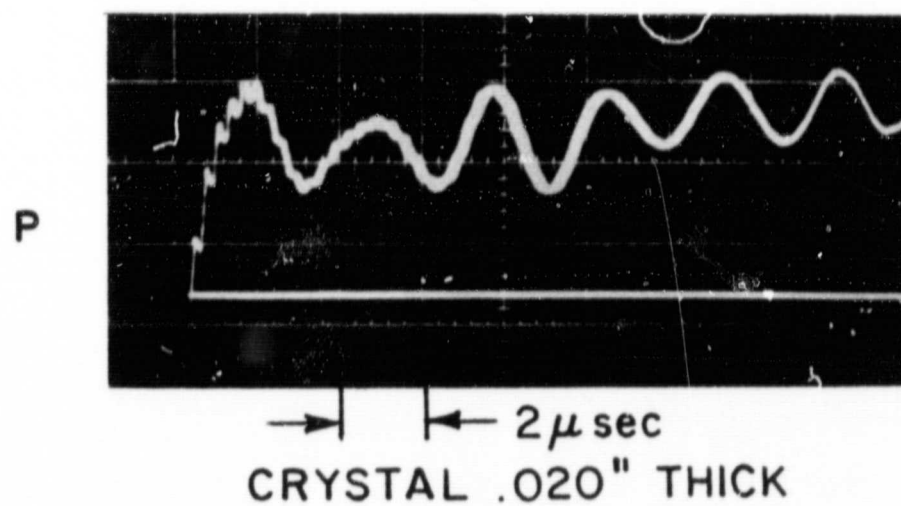
RESPONSE OF BRASS BACKED PIEZO PROBE
TO A REFLECTED SHOCK WAVE

FIGURE 3−5

match. The response of a brass-backed probe to a reflected
shock wave in a shock tube is presented in Fig. 3-5 as a typ-
ical reaction to a pressure discontinuity. It can be seen
that the response is not ideal for several reasons: the ini-
tial signal does not rise to the constant pressure reservoir
value until about 2 μsec due to the superposition and inter-
action of two modes of internal stress oscillations. The high-
frequency oscillation is a longitudinal mode across the crystal
thickness and the lower frequency oscillation is a radial mode.
Only the initial rise occurs with the desired 0.1 μsec and so
such a device cannot be used for determining magnitudes on a
submicrosecond time scale. A similar probe with a tin backing
rod responded with comparable thickness oscillations but, sur-
prisingly, with a much more severe radial oscillation which did
not damp out for hundreds of microseconds. In order to provide
a perfect match, a depolarized PZT-5 cylinder was incorporated
into a probe housing. This design resulted in exaggerated
radial oscillations and there was little improvement in match-
ing effect. This behavior could not be explained by the sim-
plified one-dimensional approximation, and so a more exact con-
sideration, including three-dimensional effects, was attempted.

For simplicity, the three-dimensional system will be
considered with a rectangular, rather than circular, cross
section. Fundamentally, if a uniform axial stress is applied
over the end of a bar (Fig. 3-6), there will be axial as well
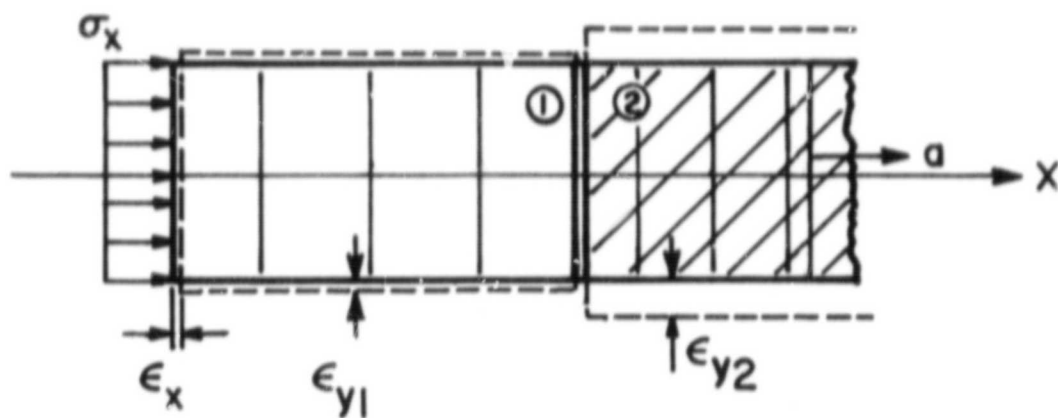
THREE-DIMENSIONAL STRESS WAVE MODEL

FIGURE 3-6
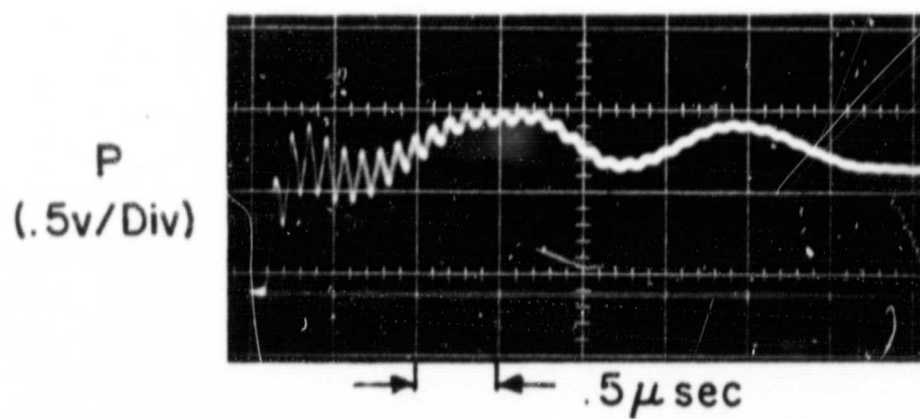
CRYSTAL .010" THICK

RESPONSE OF STAINLESS STEEL BACKED PIEZO PROBE
TO A REFLECTED SHOCK WAVE

FIGURE 3-7

as lateral strains, expressible as

$$\epsilon_x = \frac{\sigma_x}{E} \; , \qquad \epsilon_y = -\nu \frac{\sigma_x}{E} \; , \qquad \epsilon_z = -\nu \frac{\sigma_x}{E} \qquad (3\text{-}6)$$

where ν is Poisson's ratio and isotropic behavior has been assumed. In terms of these variables, the general stress equations can be written

$$\sigma_x = \lambda e + 2 G \epsilon_x$$

$$\sigma_y = \lambda e + 2 G \epsilon_y \qquad (3\text{-}7)$$

$$\sigma_z = \lambda e + 2 G \epsilon_z$$

where $\lambda = \dfrac{\nu E}{(1 + \nu)(1 - 2\nu)}$

$e = \epsilon_x + \epsilon_y + \epsilon_z$

$G = \dfrac{E}{2(1 + \nu)}$

The solutions of the above system of equations are strongly dependent on the boundary conditions that are applied, but in any case they indicate the strong interrelationship between axial and lateral behavior. For example, in order to attain the ideal one-dimensional acoustic approximation, the lateral strain components, ϵ_y and ϵ_z, are equated to zero. However, to accomplish this requires the uniform application of stresses

$$\sigma_y = \sigma_z = \left(\frac{\nu}{1 - \nu} \right) \sigma_x$$

with ratios of $\sigma_y / \sigma_x = 0.4$ for typical materials. Need-
less to say, the implementation of such a stress scheme gen-
erally is unreasonable. Further, a realistic evaluation of
the stress conditions within the complete probe structure
must consider a rod surrounded by other reacting materials.
Any axial stress will result in lateral stress generation in
the rod from both internal and external sources due to lateral
strain. The situation is further complicated when the inter-
face between crystal, 1, and backing rod, 2, is considered
since boundary conditions on the lateral particle displace-
ments and stresses must now also be satisfied. A complete
theoretical analysis of the probe structure behavior in the
context of the above outline would clearly be excessive, and
outside the scope of the present work. Rather, what is de-
sired is a determination of the source of the radial oscil-
lations in the crystal, and this effect should now be evident
on properly analyzing the probe response. Specifically,
since the normal boundary conditions at the interface are not
critical, the lateral boundary conditions must control the
behavior. The lateral strain can be expressed as

$$\in_{y,z} \; = \; - \, \frac{\nu}{E} \; \sigma_x \; = \; fn\!\left(\frac{\nu}{E}\right)$$

with the normal stress condition assumed satisfied. Accord-
ingly, the value of the parameter, ν/E, was tabulated for

the crystal and different backing rod materials used:

Material	ν/E	Back rod performance
PZT-5	5.7×10^{-12} m^2/n	Poor
Tin	8.0×10^{-12}	Unsatisfactory
Brass	3.0×10^{-12}	Generally satisfactory

The above tabulation can be reduced to the following reasoning:
Since $\epsilon \sim (\nu/E) \cdot \sigma$, the backing rod material that will allow
the smallest lateral strain for a given axial stress will pro-
vide the best transient oscillatory response. Physically,
this can be interpreted as an indication that the backing rod
should function to damp radial oscillations within the crystal.
To corroborate this hypothesis, a material was selected to pro-
vide a limiting value for the damping parameter; stainless
steel ($\nu/E = 1.6 \times 10^{-12}$ m^2/n) was chosen as optimum. The
response of such a probe to a reflected shock wave is presented
in Fig. 3-7; such a device can be considered to meet satis-
factorily the requirements on stress oscillations for a submi-
crosecond pressure probe.

3.4 ELECTRICAL INSULATION AND PROBE CONFIGURATIONS

The problem of developing an insulating covering for
the piezo element that would produce no signal delay nor in-
troduce any extraneous stress conditions presented difficulties.
Because of the inherent delay introduced by any covering due to
stress propagation, an effective real-time probe must utilize
an extremely thin covering so that this delay will not appear

on the time scale of the event. Typical insulator properties indicate acceptable delays of 10^{-8} sec for a thickness of approximately 10^{-2} mm. In order to meet this requirement, the use of a number of lacquers and liquid insulating compounds was attempted as insulators with little success. However, the utilization of a thin, polyester base, electrical insulator tape proved quite satisfactory. Specifically, the application of one layer of 1 mil (0.001 in.) thick #74 Scotch insulating tape was found to hold off 5,000 volts when properly applied. A single, thinned layer of Zapon lacquer over this was also found to be beneficial. Theoretically, this tape would produce only several nanoseconds delay; detailed shock tube experiments confirmed that there was no noticeable delay or dispersion of the pressure probe response.

The electrical insulation of the outer conductor shell was accomplished by fitting the internal probe circuitry into either machined nylon or Pyrex tubes. The mechanical properties of each of these materials, along with those of the conducting shell, were related to a low-frequency radial oscillation that appeared in the probe output. It was found that this oscillation could be controlled by utilizing acoustically absorbent materials outside the backing rod. Practically, this involved using beeswax adjacent to the crystal as an insulator-sealer and using brass for the conducting shell. The tailoring of the shell thickness and material to control the low-frequency oscillation resulted in the two configurations shown in Fig. 3-8.

SILVER PAINT
MYLAR TAPE
SEALER
PZT-5 DISC
MYLAR
S.S. BACKING ROD
NYLON HOLDER
BRASS SHELL

PYREX TUBE

EPOXY

50 Ω COAXIAL CABLE

TO OSCILLOSCOPE

RADIAL PROBE

AXIAL PROBE

BNC CONNECTOR

MODIFICATIONS OF FAST RESPONSE PIEZOELECTRIC
TRANSDUCER : a) AXIAL PROBE ; b) RADIAL PROBE

FIGURE 3-8

AP 25 4330 G7
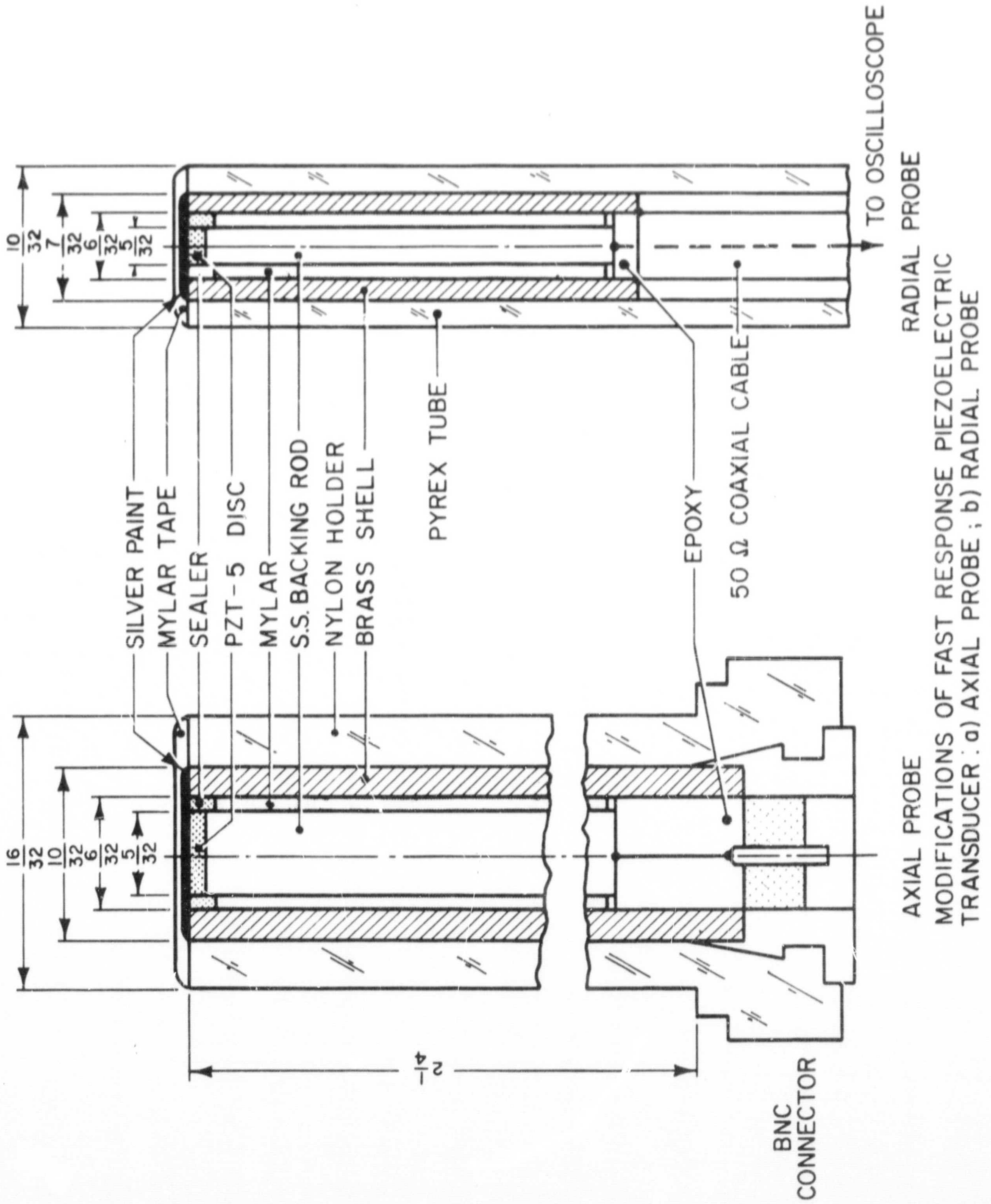
3.5 PROBE PERFORMANCE AND CALIBRATION

The evaluation of probe performance and probe calibration was carried out using reflected shock waves in simple shock tubes. Before proceeding to a detailed discussion of probe calibration, it is of interest to consider some general aspects of probe system behavior.

A general-purpose, pressure-burst shock tube was used to evaluate basic performance. The 7/8-in.-i.d. tube had a 21-in. driven section with 1 atm air and a 22-in. driver section filled with 4 atm of helium, both at room temperature. The response of the present design pressure probe is presented in Fig. 3-9. On such records it is of interest to identify the constant pressure plateau, the rarefaction arrival, and the twice reflected shock arrival for time correlation. Before interpreting this response, consideration should again be given to the circuit time constants. It has been noted that, for the basic probe circuit, RC(effective) = 600 μsec. Accordingly, for time up to 60 μsec, the probe signal will be directly proportional to pressure and so the exact equilibrium plateau will be sensed for calibration purposes, but at later times the signal will reflect RC decay. In fact, such behavior was evident when a 10 megohm resistance was temporarily inserted in series with the load resistance; decay was considerably reduced, but the onset of both the rarefaction and reflected shock were clearly indicated at the apparent times in Fig. 3-9. Returning to a consideration of probe performance, it is evident that the
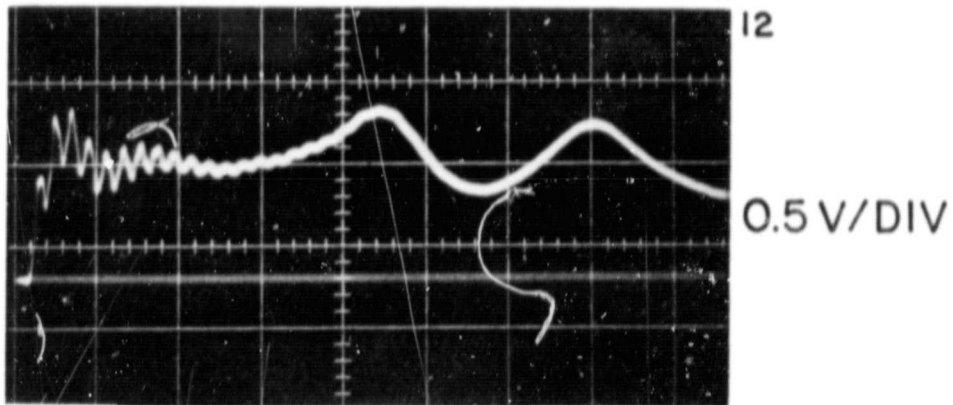
a) 0.5 μsec/DIV

b) 1.0 μsec/DIV

c) 2.0 μsec/DIV

d) 10 μsec/DIV

e) 100 μsec/DIV

f) 500 μsec/DIV

0.5 V/DIV
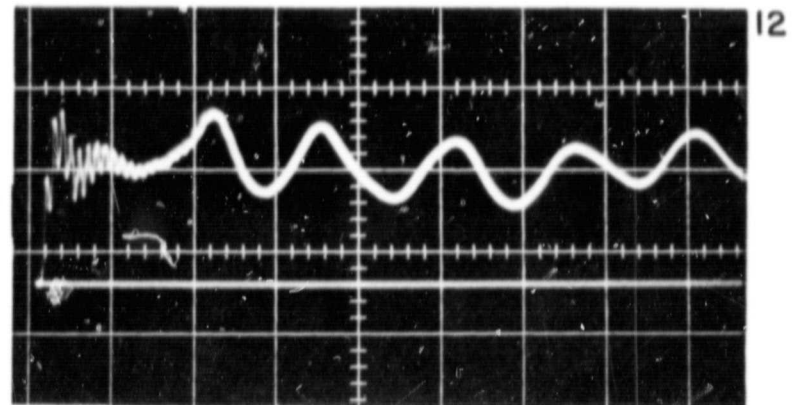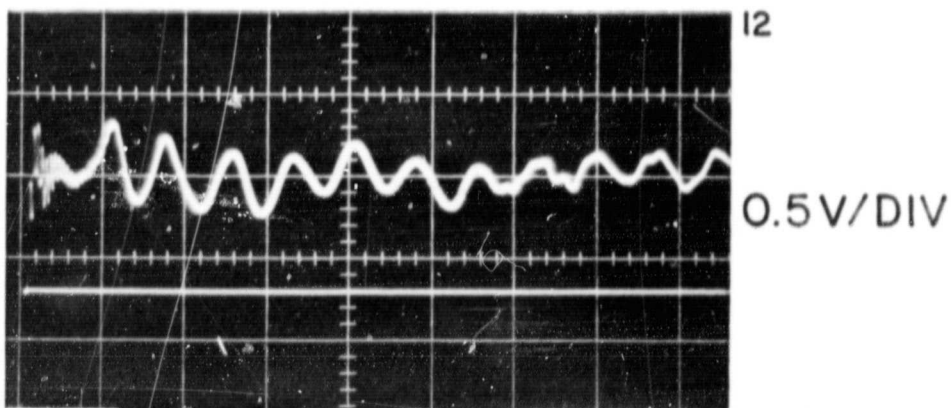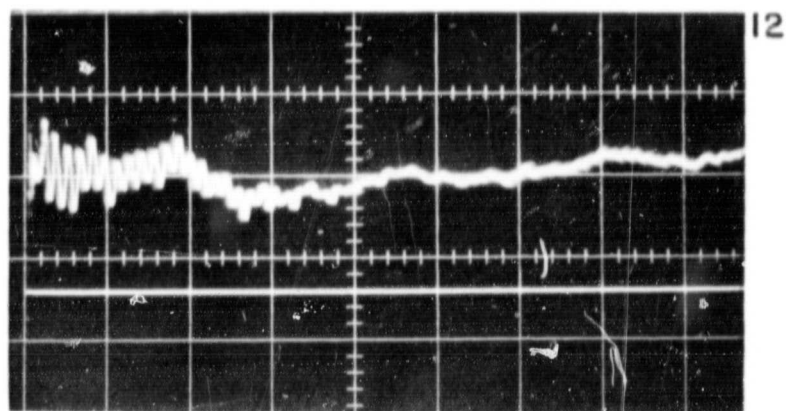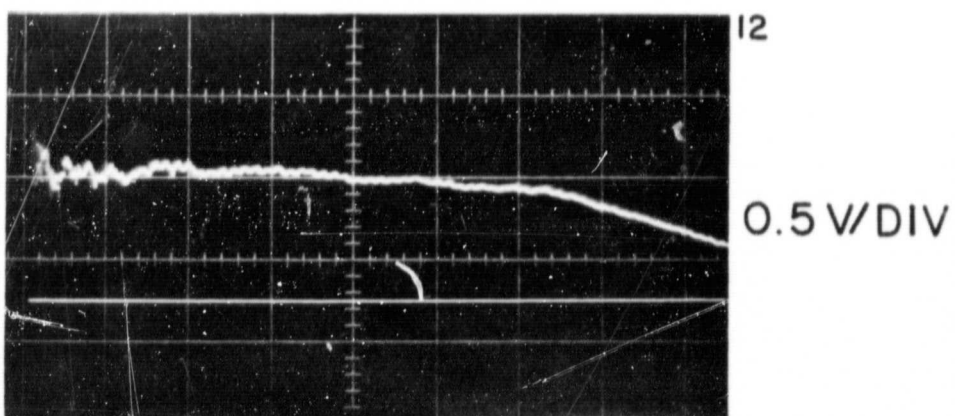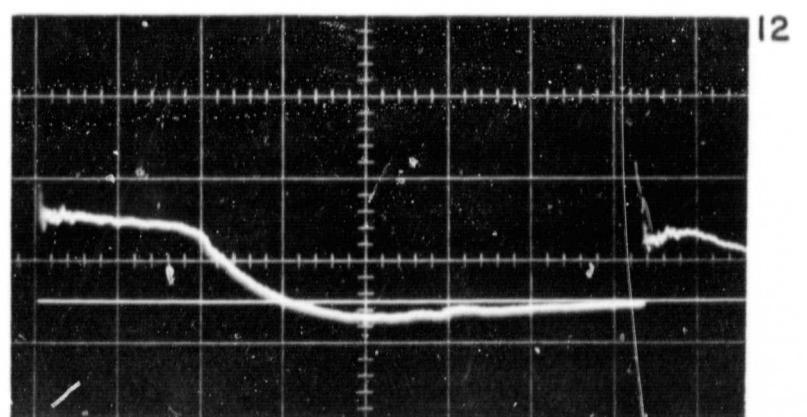
PRESSURE PROBE RESPONSE TO A REFLECTED SHOCK IN
SHOCK TUBE

probe responds to within ten percent of mean pressure on the first pulse, i.e., less than 0.1 μsec.

The pressure probe calibration was carried out using simple, single-diaphragm, constant area shock tubes. This method was chosen because it is highly reproducible, it provides an impulse on the desired su:'microsecond time scale, and it permits calibration over a reasonable operating range. In particular, it was desired to calibrate the probes over a range of pressures that included the ambient discharge pressure of 100 μ and over as large a range of pressure increment as possible. This was carried out by subjecting the probe to the head-on reflection of the shock from the tube end wall. Regarding the low density calibration, it is well-known [30] that shock tube behavior diverges from classical inviscid behavior because of boundary layer effects in this density regime. So, rather than embark on a lengthy data reduction scheme for low density calibration, it was decided to utilize experimental low density shock-tube data presented by Duff [31], by constructing a shock tube with exactly the same internal dimensions as his device. Accordingly, a shock tube with 1 1/8-in. i.d., 3-ft driver, and 7-ft driven section was assembled; the diaphragm was manually burst. Using Duff's data on shock Mach number for given initial pressure and diaphragm pressure ratio, reflected shock data was taken over an ambient pressure range from 500 μ to 300 mm Hg argon with argon driver gas. This range was extended to ambient pressures of 1.0 atm argon with

a 21-in. driven section driven by both argon and helium drivers.
Corresponding pressure jumps across the reflected shock of from
0.01 to 5.3 atm were calculated. Within experimental limits,
the probe output voltage was found to vary linearly with pres-
sure increment. Specifically, for the axial probe $V_s /\triangle P = 0.25$
volts/atm, and for the radial probe $V_s /\triangle P = 0.30$ volts/atm.

3.6 PROBE PERFORMANCE WITHIN THE PINCH DISCHARGE

The use of the pressure sensing device developed above
within a plasma environment has some inherent difficulties that
should be considered. The active probe element will respond to
momentum transfer imparted to the insulator surface, but because
of the particle energies in the plasma, the insulator itself may
participate in the momentum transfer through ablation and sec-
ondary emission. These effects have been examined both theo-
retically and experimentally by Friedman [32] for high energy
thermalized plasmas and found to be unimportant for pressures
in the neighborhood of 0.1 atmosphere. For the slightly higher
pressures of the present highly transient experiment, these
effects can be considered insignificant.

The problem of determining, discriminating, and elimi-
nating other extraneous signals in the pressure probe circuit,
however, did require careful attention. First, the proximity
of the probe to the discharge initiation subjects the probe
circuit to the related burst of intense electromagnetic radi-
ation; the resulting spurious signal is evidenced by a decaying
"noise" oscillation within the cable. This signal can effec-

tively be eliminated in a low impedance circuit, such as for a magnetic probe [14], by properly terminating the coaxial cable at both ends. However, in the present case, with a high impedance device and small output signal this troublesome signal required the design and application of a cathode follower amplifier to allow for satisfactory probing. Cathode follower design has been well documented in the archive literature [33], and so will not be discussed in detail. Rather, the design will simply be presented (Fig. 3-10) and the high-frequency performance noted. The follower was driven by a battery source and completely enclosed within a grounded box, but it was still found necessary to operate the device only inside the oscilloscope screen room because of extraneous pickup. The frequency response of this device was experimentally evaluated using an electronic square-wave pulse generator. Typical overlays of circuit response with and without follower are presented in Fig. 3-11; it can be seen that the response was satisfactory, with a voltage reduction factor (0.945) that was in agreement with theory.

In order to discriminate between pickup and real pressure signals, a number of techniques were employed such as reversing crystal polarity, reversing machine polarity, and rotation about the probe axis. However, the most useful technique involved placing a layer of 1 mil insulating tape over the outer piezo element surface and assembling as before. The insulation excluded any real pressure signal and thus allowed
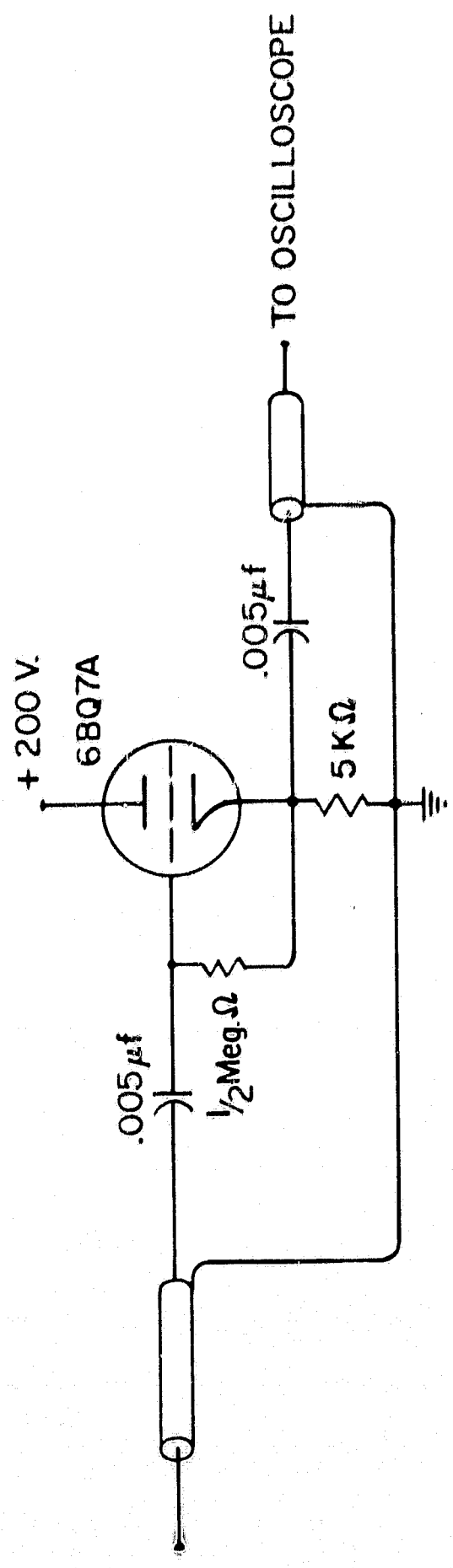
CATHODE FOLLOWER CIRCUIT

FIGURE 3-10

+ 200 V.

6BQ7A

TO OSCILLOSCOPE

.005 µf

.005 µf

½ Meg. Ω

5 KΩ

V_{OUTPUT}

(2.v/ Div)

V_{OUTPUT}

(10.v/ Div)

5. VOLT INPUT	30. VOLT INPUT
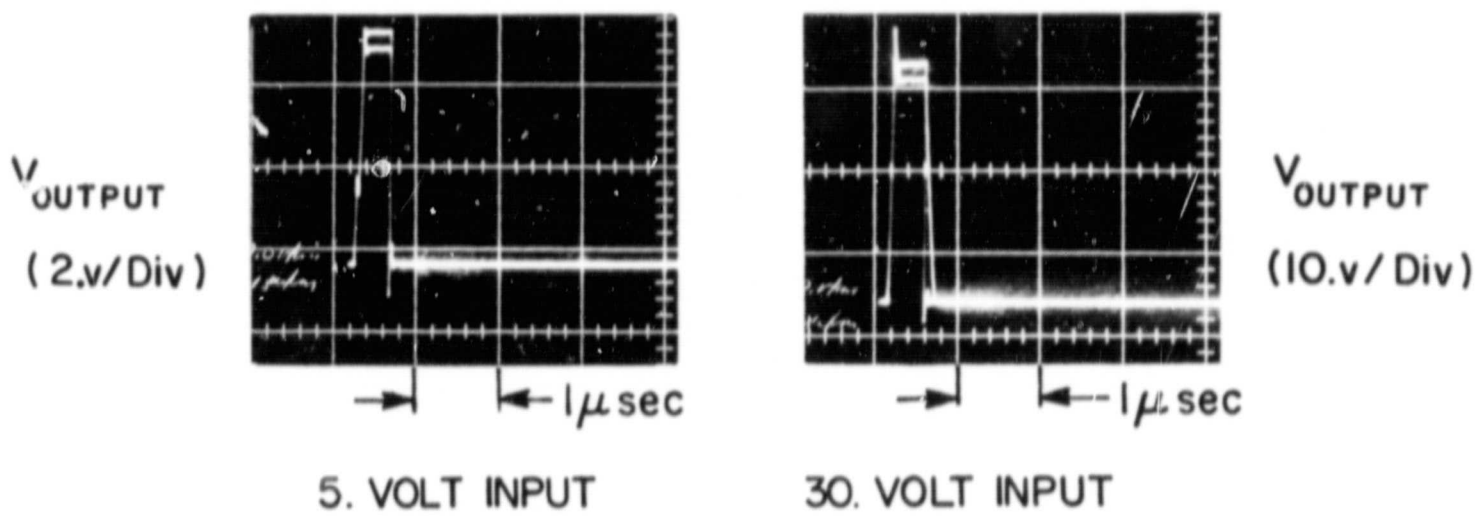
CATHODE FOLLOWER RESPONSE TO SQUARE WAVE

FIGURE 3-11

T-3400

$\dot{B}_\theta$ (10.v/ Div)

P (.5 v/ Div)
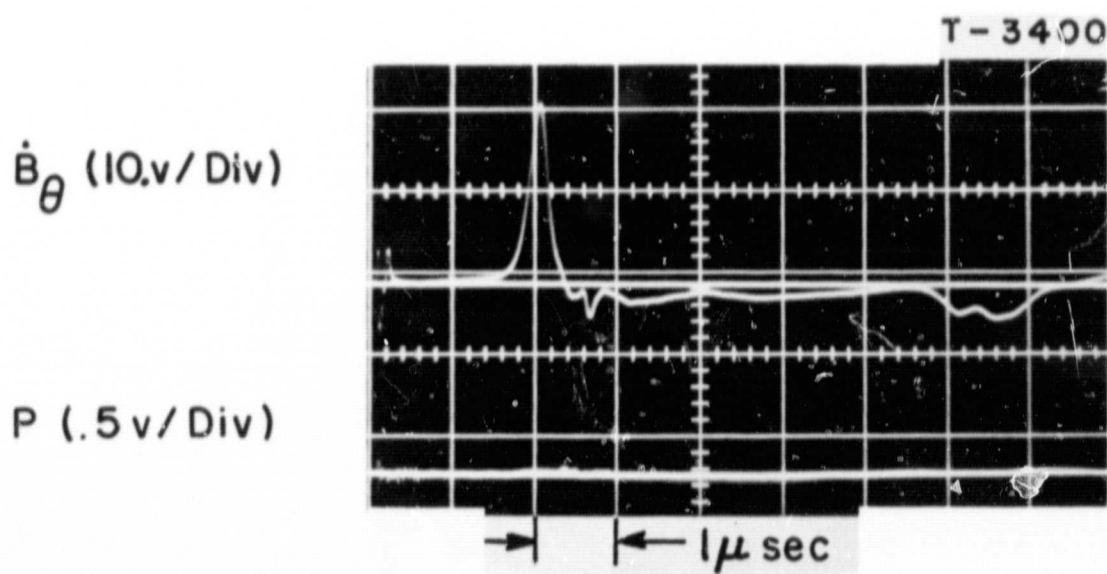
PRESSURE PROBE RESPONSE WITH INACTIVE ELEMENT

FIGURE 3-12

identification of all extraneous signals; the resulting "null" signal for the pressure probe circuit is presented in Fig. 3-12.

With the above mentioned refinements in the pressure probe circuitry, the probes were inserted into the pinch discharge chamber; the typical responses shown in Fig. 3-13 were observed. The simultaneous record of $\dot{B}_\theta \sim j$ (Appendix A) included with each pressure history was recorded for time reference within the sheet structure; the magnetic probe was mounted on the pressure probe structure to insure exact time correlation.

T-3624

$\dot{B}_\theta$

P_R
(20v/Div)

|← 1 μsec
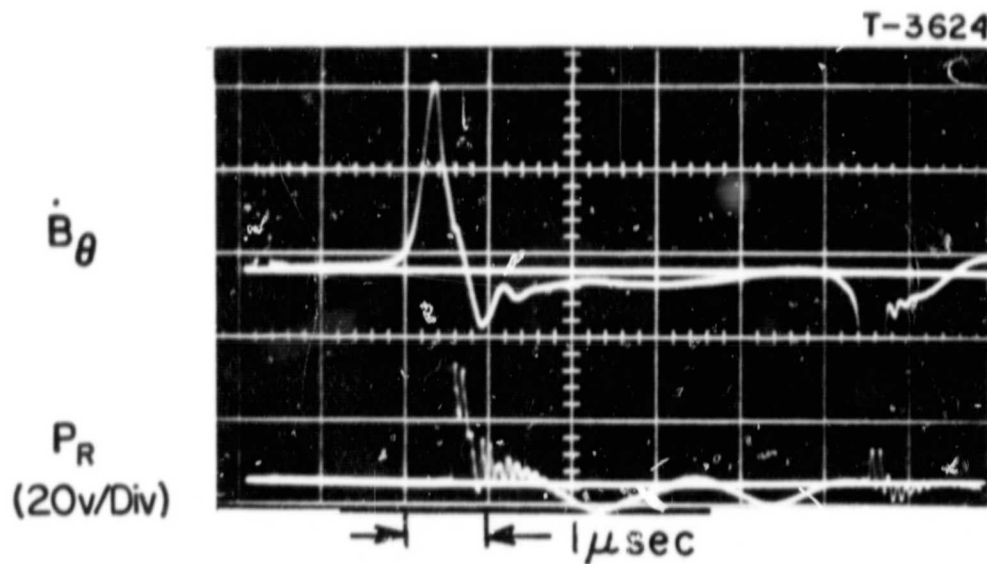
a) RADIAL PROBE (HEAD ON SHEET INTERACTION)

T-3639

$\dot{B}_\theta$

P_z (C)
(.5v/Div)

|← 1 μsec
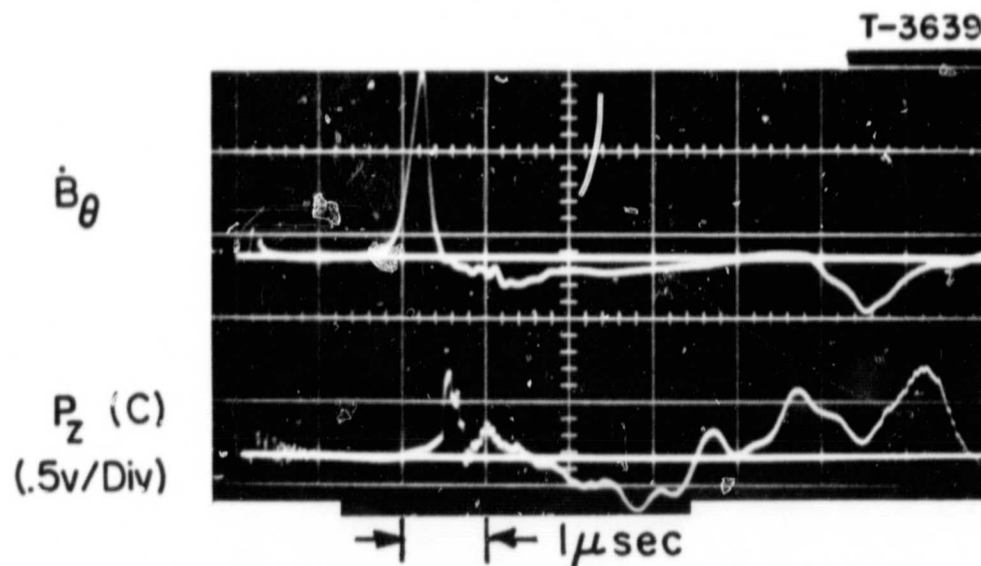
b) AXIAL PROBE MOUNTED ON CATHODE

T-3579

$\dot{B}_\theta$

P_z (A)
(.5v/Div)

|← 1 μsec
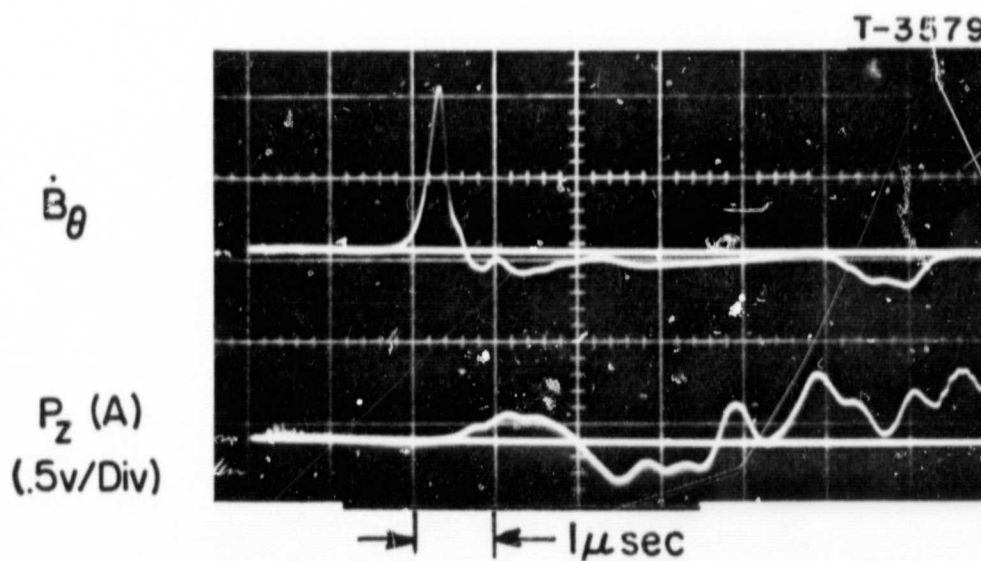
c) AXIAL PROBE MOUNTED ON ANODE

TYPICAL PRESSURE PROBE RESPONSE IN PINCH DISCHARGE
R = 2" , h = 1"

CHAPTER 4

PRESSURE PROBE—CURRENT SHEET INTERACTIONS

4.1 INTRODUCTION

The useful application of pressure probes to the diagnostics of current sheet structure requires a detailed knowledge of undisturbed current sheet behavior and a knowledge of the interaction between the current sheet and the probe structure. Accordingly, the discharge was examined with local magnetic field probes and high-speed photographic techniques, with the intention of determining the optimum configuration for probing the current sheet structure.

4.2 CURRENT SHEET PROFILES IN THE PINCH DISCHARGE

The variation of total circuit current with time has been presented earlier, however, the discharge chamber can conduct this current with a number of possible current density distributions depending upon electrode material, electrode configuration, etc. Studies of current sheet profiles in specific devices have been presented in the literature [8, 12 to 14], but generally serve to illustrate the diversity of conduction modes that can be generated. Ideally, the current conduction between the pinch chamber electrodes would take place within a thin cylindrical sheet that was axially and azimuthally uniform.

The work of Burton [13] clearly identified the experimental characteristics of such a current sheet as a diffuse layer or "foot" on the anode, an evident tilt of the central current sheet region, and a distortion of the current sheet near the cathode. However, the sheets produced in that device were well-defined and satisfactory for study. The magnetic probe study of the constant-current, large-diameter pinch presented by Ellis [14] indicated a less satisfactory sheet, as these effects were more dominant.

As a first step toward defining current sheet behavior with the present waveform, luminosity profiles of the imploding current sheet were examined with photographs taken in a radial view Kerr-cell arrangement (Fig. 4-1). The photographic line-of-sight was established by removing a section of the outer chamber conductor while inserting heavy bolts to allow satisfactory current flow. Typical photographs of the luminosity of the imploding current sheet are shown in Fig. 4-2, where the diffuse anode, sheet tilt, and cathode region distortion, along with the degeneracy of the sheet at small radii, can be seen. However, luminosity profiles do not necessarily define current profiles, and in order to identify that parameter, a magnetic probe study of the chamber was made.

The magnetic induction loop as a device for probing transient discharges has been well documented in the literature [17], and so will not be analyzed in detail here. A discussion of the relevant parameters for the present appli-
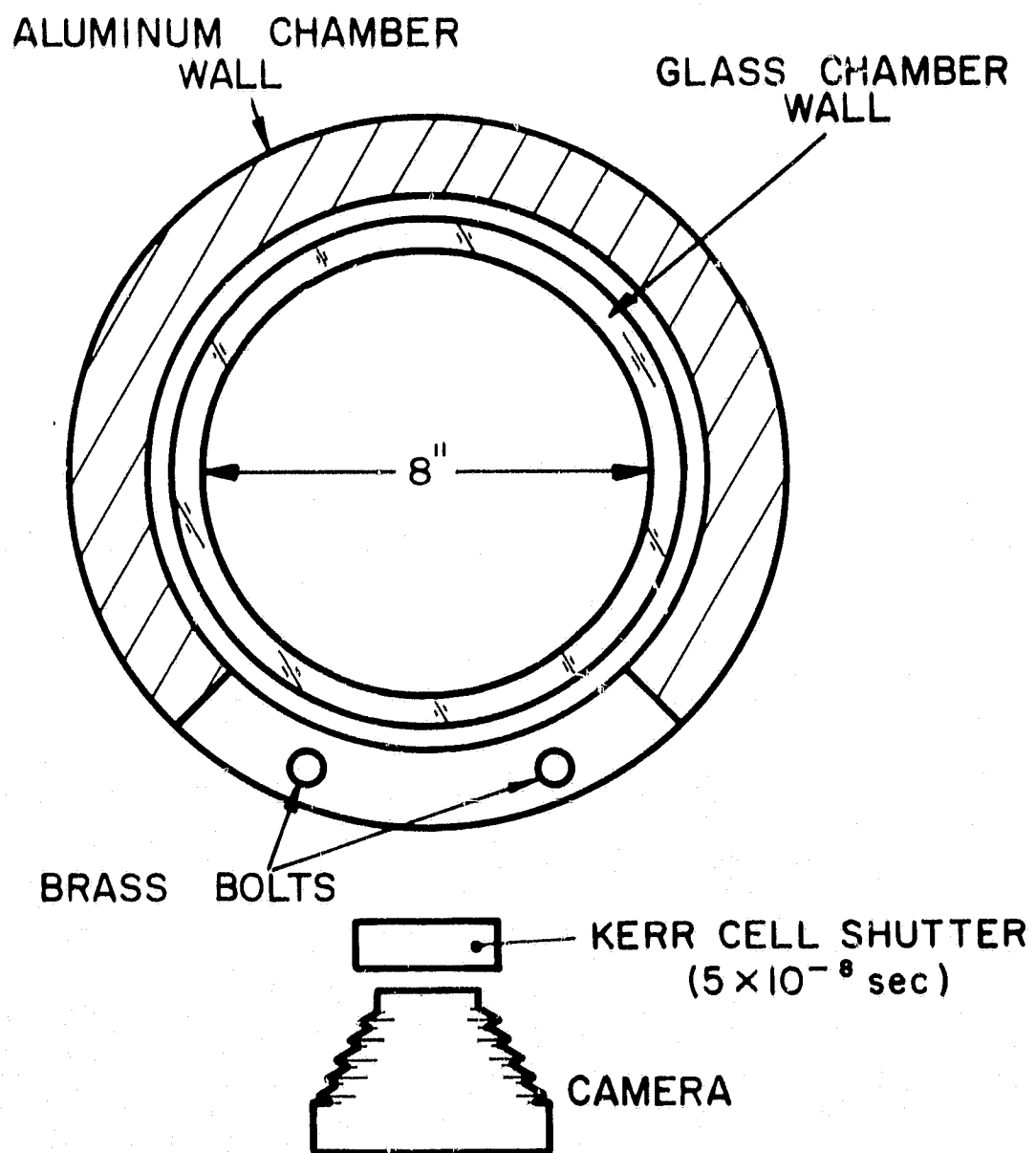
KERR CELL CAMERA ARRANGEMENT
FOR FOLLOWING PHOTOGRAPHS

FIGURE 4-1

T-2469

$I(1.78 \times 10^5 \text{AMP/Div})$

$1\mu \text{sec / Div}$
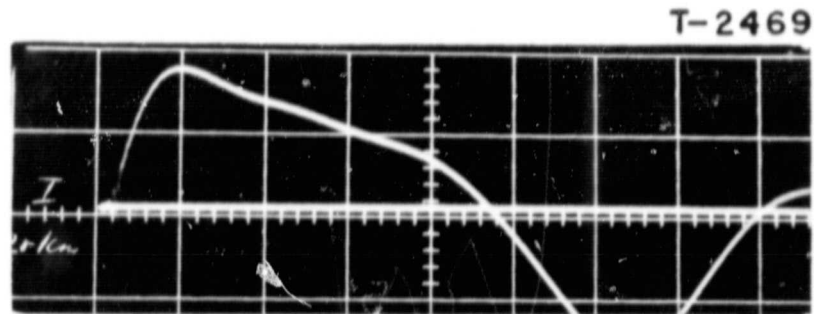
T-3119

ANODE

t=1.2 μ sec
R=3.25 in

CATHODE
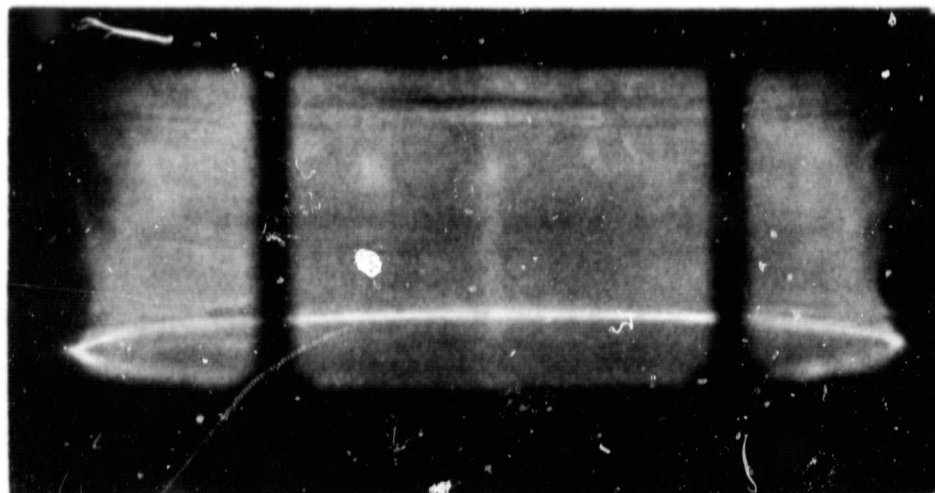
T-3120

t=1.7μ sec
R=2.50 in
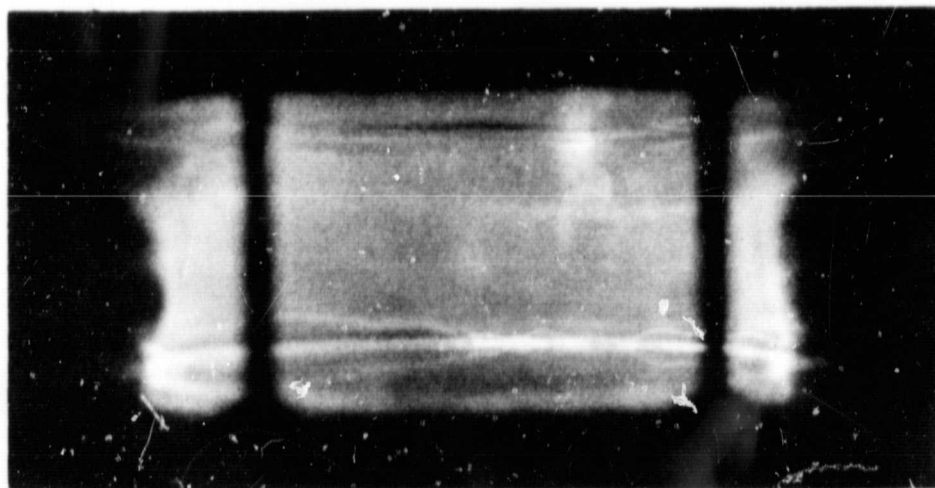
T-3121

t=2.8μsec
R=1.25 in
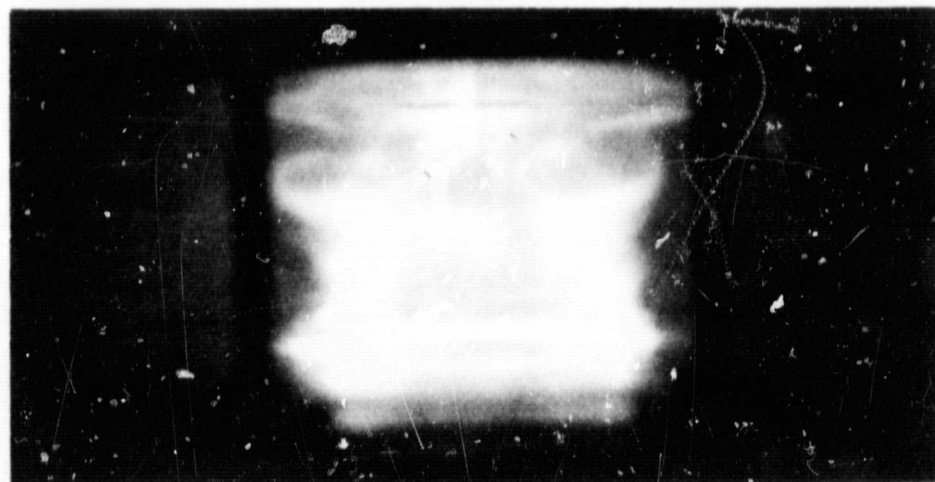
CIRCUIT CURRENT WAVEFORM AND RADIAL VIEW PHOTOGRAPHS
OF PINCH DISCHARGE

FIGURE 4-2

cation is included in Appendix A. From that outline, it will be note1 tnat $j_z \approx (\mu_o V_s)^{-1} \dot{B}_\theta$ and so j_z profiles will approximately follow $\dot{B}_\theta$ profiles. An induction coil with a 3/32-in.-i.d., wrapped with #28 Formvar coated wire, encased in a Pyrex tube for convenience, was used here. A survey of the chamber was taken at 1/2-in. radial increments and 1/4-in. axial increments; a comparison of the derived current density profiles with the luminous profiles showed general agreement of sheet trajectory, diffuse current profiles near the electrodes, and sheet tilt. A typical set of axial data at R = 2 in. and a radial survey midway between the electrodes is presented in Fig. 4-3. From this, and similar data, it was concluded that a sharp, well-defined, current density profile appropriate for sheet study could be found only in the central region of the chamber. Or. this basis, detailed studies of the current sheet were carried out between radii of 3 in. and 1 in., and close to the midplane (h = 1 in.).

4.3 LUMINOSITY STUDIES OF PROBE INTERACTION

With the understanding of current sheet behavior presented above, the problem of probe interference with the current sheet became of primary concern. As a first step, several "dummy" models of probing shapes were inserted through the chamber walls and the luminosity patterns about them were photographed. The first shape to be examined was that of a radial probe, extending through pinch position to the probing position (R = 2 in., h = 1 in.); Fig. 4-4 shows a sequence of photographs
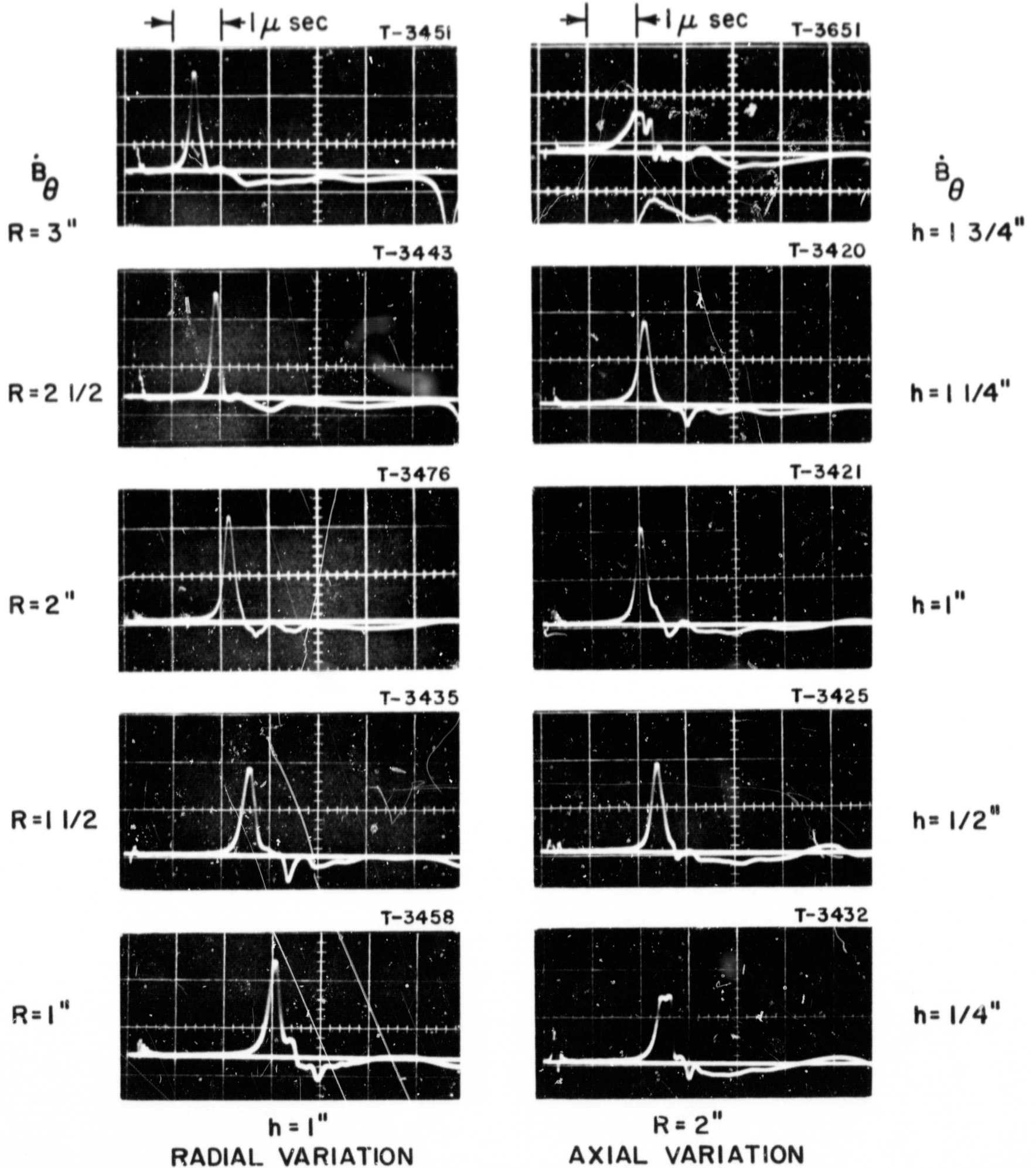
RADIAL AND AXIAL MAGNETIC PROBE SURVEYS

FIGURE 4-3

47

ANODE

1.9 μ sec

CATHODE

2.0 μsec

(4.5 X)

2.2 μsec

(4.5 X)

2.4 μsec

(4.5 X)
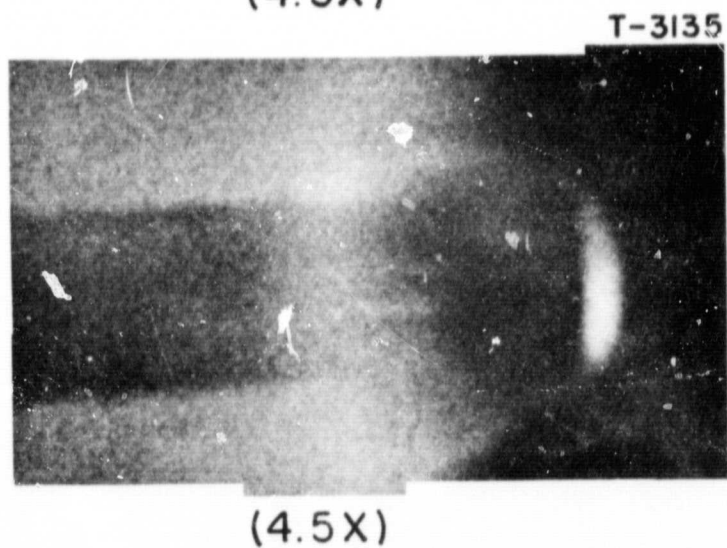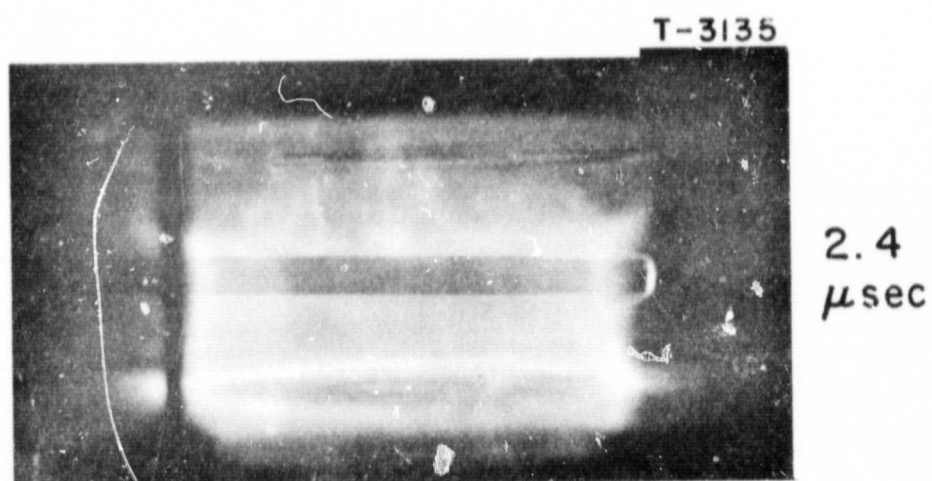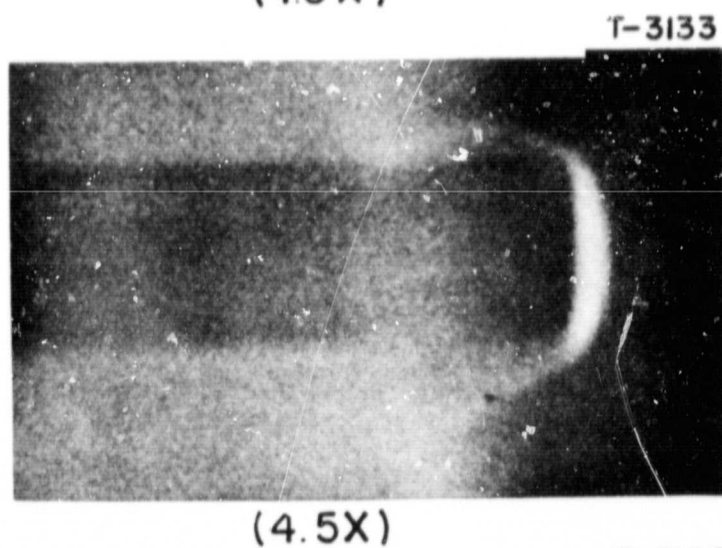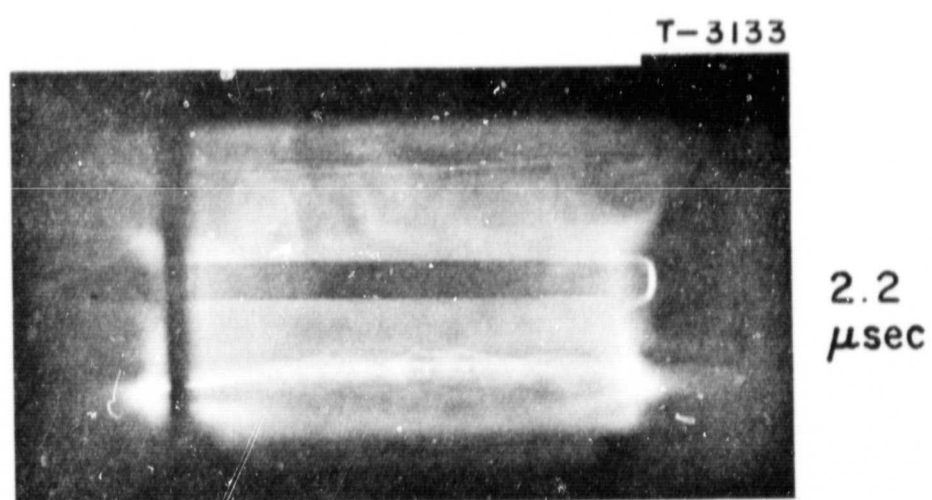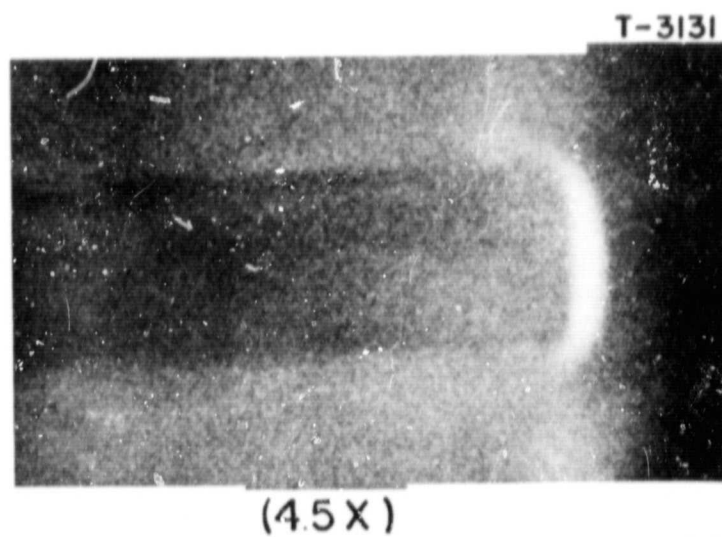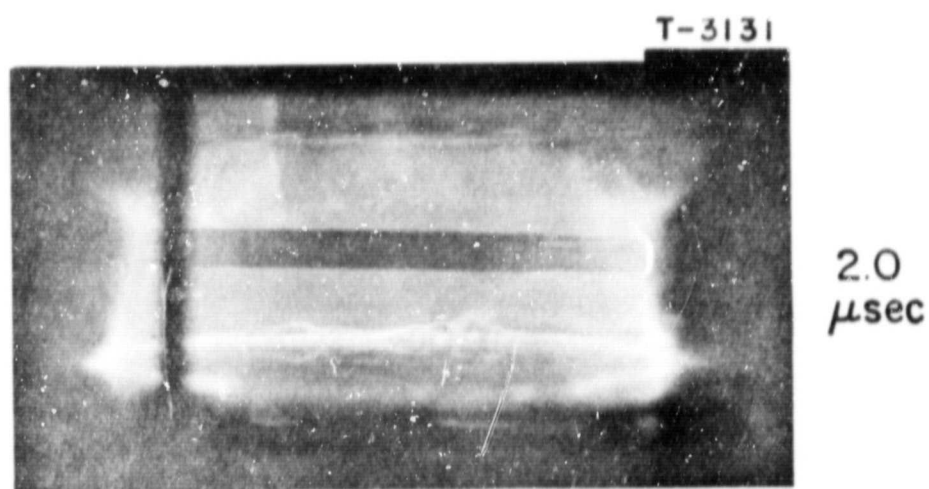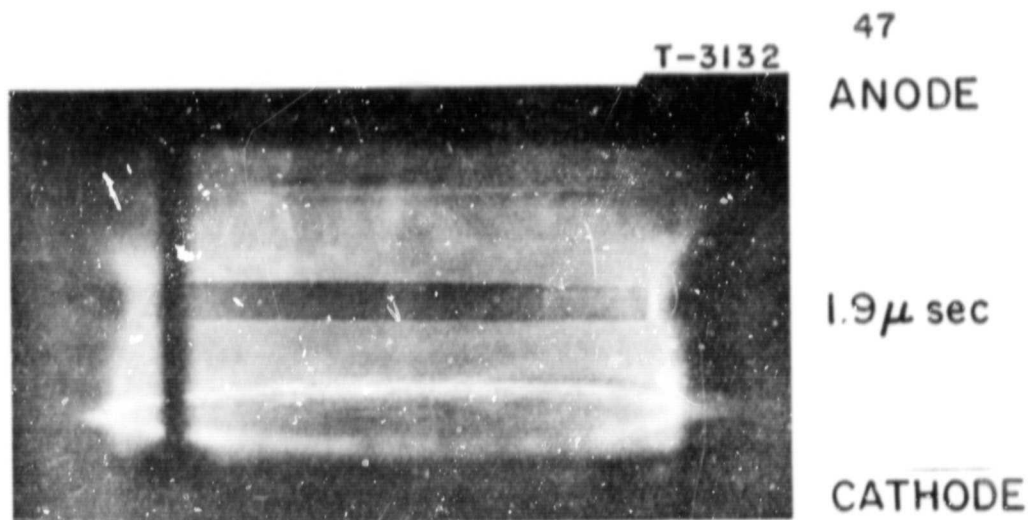
LUMINOSITY PATTERNS ABOUT RADIAL PROBE

FIGURE 4-4

with the current sheet moving past the probing shape along
with a 4.5 x magnification of the region of interest. From
these photographs it is evident that at this probing position
(R = 2 in.) the probe is not immersed in the anode foot. How-
ever, upon the arrival of the clearly defined rear surface of
luminosity, the stagnation region of the probe becomes in-
tensely luminous and at later times typical wavelike contours
of luminosity about the probe shape are evident. It should
also be noted that there is a definite asymmetry evident in
the luminous wave pattern, approximately five degrees toward
the cathode. This value is in good agreement with a measured
sheet-tilt angle of five degrees at this position, both indi-
cating an axial sheet velocity component toward the cathode.

A similar sequence of photographs was taken of an axial
probe shape; Figs. 4-5a,b, and c show luminosity patterns when
the sheet first reaches the probe and at later times. Note
that the flow again stagnates on the side (non-sensing) sur-
face of the probe and the wavelike profiles then appear after
the passage of the sheet rear surface of luminosity. In order
to determine if the wavelike contours of luminosity were the
results of expansion of a stagnated gas around the probe shape,
a thin, sharp-edged annular collar was fitted over the probe
end. Such a shape would eliminate an expansion of stagnated
gas, and also would prohibit the side of the probe shape from
communicating with the sensing surface. Several photographs
of the luminosity profiles of this arrangement are presented

T-3141

ANODE

CATHODE

a)   1.9 μ sec

T-3143

b)   2.0 μ sec
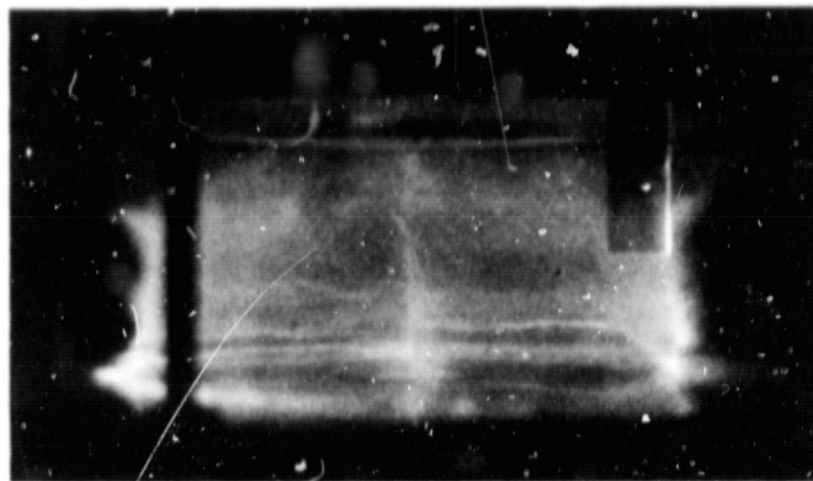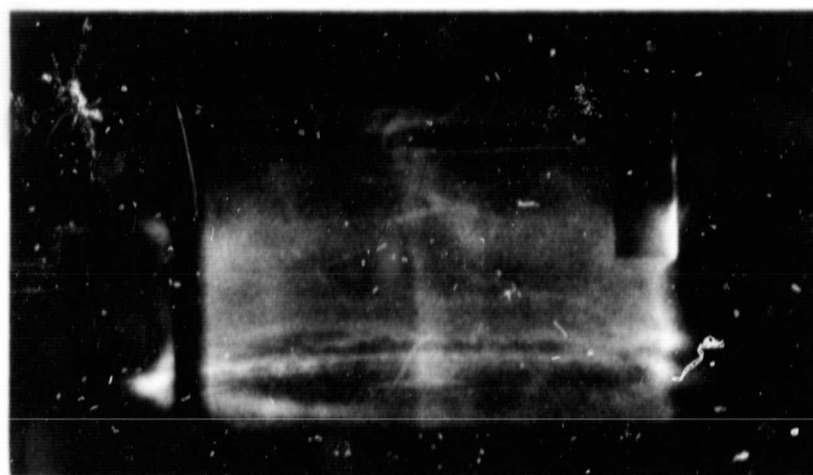
T-3144
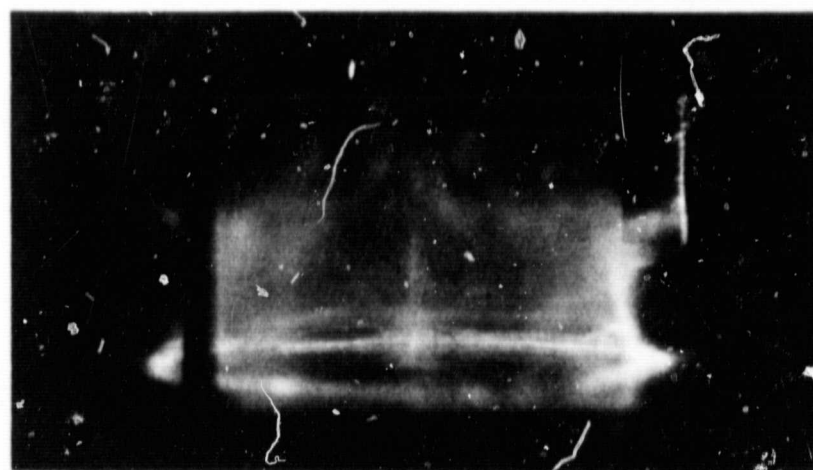
c)   2.4 μ sec

LUMINOSITY PATTERNS ABOUT AXIAL PROBE
100 μ ARGON

in Fig. 4-6. Wavelike profiles are again evident without a
stagnation region, indicating that the "waves" are represen-
tative of the gas properties behind the sheet luminous surface.

4.4 LUMINOSITY—CURRENT DENSITY CORRELATION

In order to clarify the relative positions of sheet
luminosity, the rear surface of sheet luminosity, and the re-
gion that gives rise to the wavelike contours relative to cur-
rent density profiles, simultaneous data of luminosity—$\dot{B}_\theta$ were
taken. First, in order to establish the radial distribution
of luminosity, the outer solid conducting electrode was tempo-
rarily replaced by one with a 6-in. diameter Pyrex insert that
provided an axial view of the chamber. It was found that such
an electrode produced no definable current distortion except
quite close to the electrode (cathode). Noting that the in-
tense luminosity on the axis is light bleedthrough at pinch (of
no significance here) from the axial view Kerr-cell photograph of
the discharge (Fig. 4-7). it can be seen that the sheet lumi-
nosity occurs within an annulus approximately 1.5 cm wide.
Further, from the complementary record of a magnetic probe
mounted on a radial pressure probe, it is evident that the
axial current was flowing about the probe significantly ahead
of the rear surface of sheet luminosity, the surface that is
definable in the radial view photographs.

With a metal cathode again in place, a metal grill-
work installed for the outer chamber wall to insure current
distribution, and an axial probe shape with built-in magnetic

T-3149

ANODE

1.3 μ sec

CATHODE

T-3150 A

T-3150

1.8 μsec

C

(4.5 X)

T-3161 C

T-3161

1.6 μsec

A

(4.5 X)
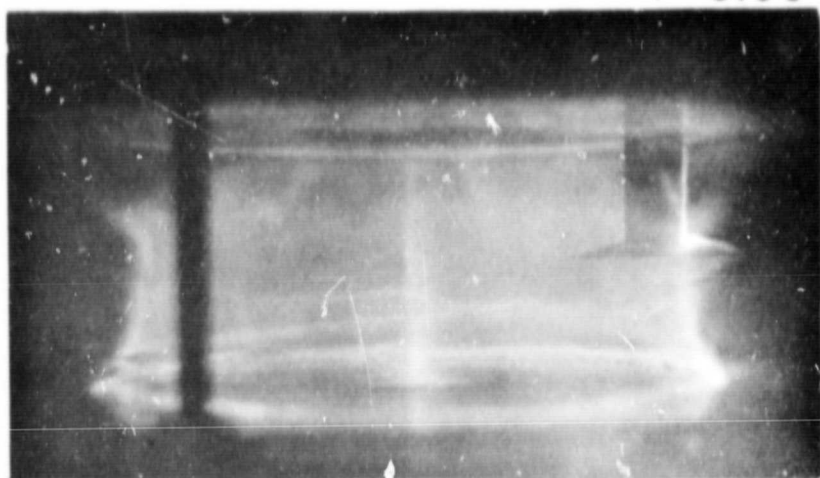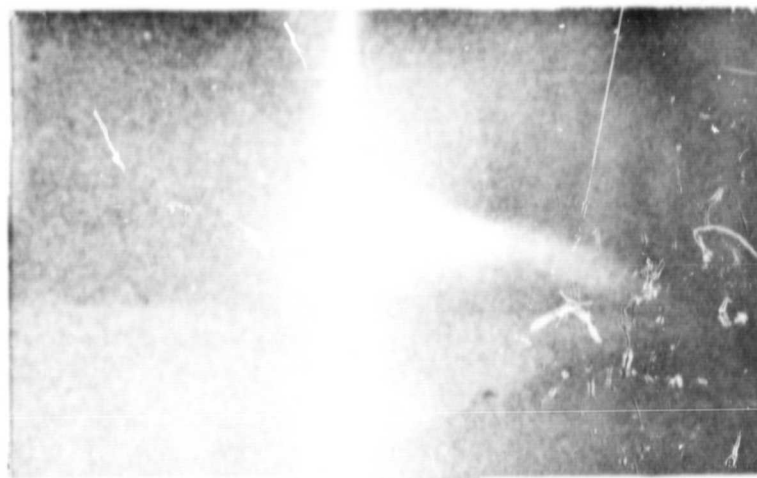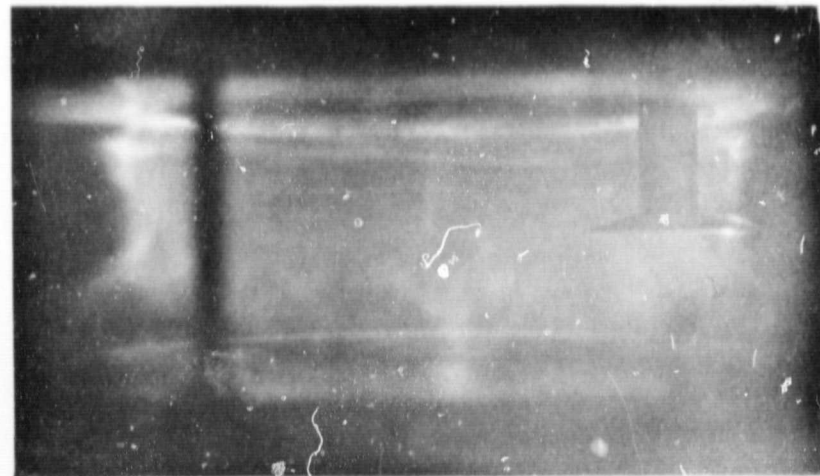
100 μ ARGON

LUMINOSITY PATTERNS ABOUT AXIAL PROBE WITH
FLOW ISOLATOR

FIGURE 4-6

T—3714

$\dot{B}_\theta$

SHUTTER OPEN
AT 1.9 μ sec

I

1 μ sec

T— 3714
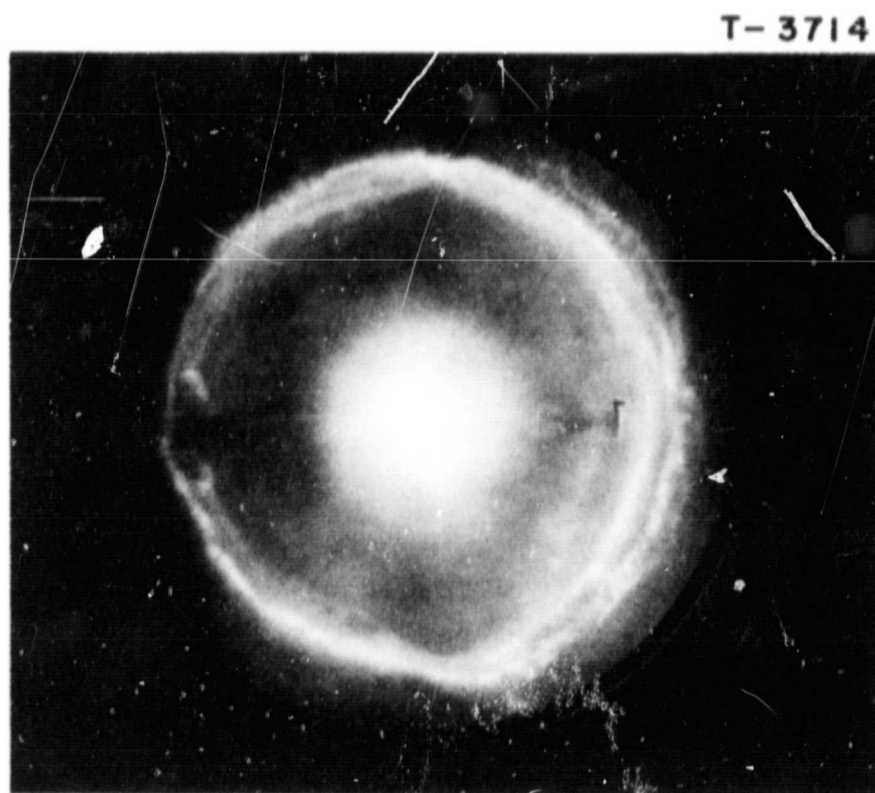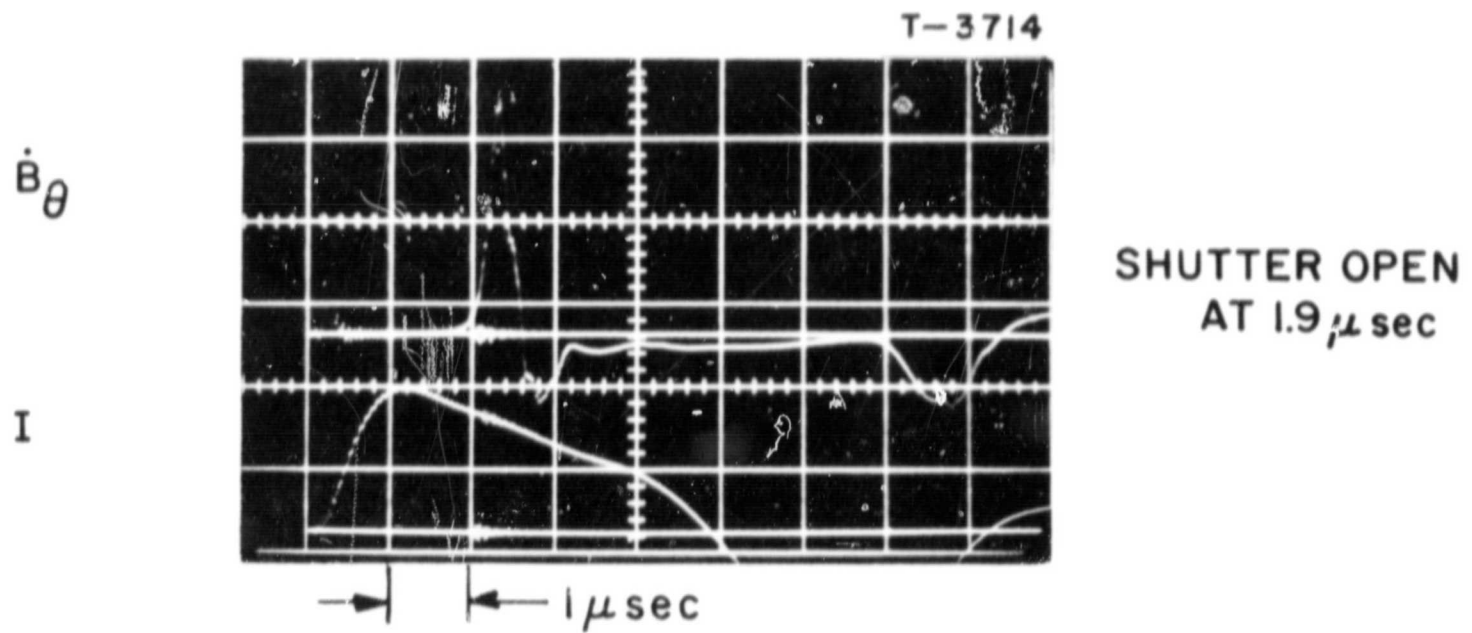
1.9 μ sec
PROBE AT R=2" ,   h=1"

AXIAL-VIEW LUMINOSITY PATTERN WITH SIMULTANEOUS
MAGNETIC PROBE RECORD

FIGURE 4-7

probe, the data shown in Fig. 4-8 were recorded. Accordingly, the rear surface of sheet luminosity can be seen to arrive approximately when $\dot{B}_\theta$ returns to zero, i.e., at the rear edge of the sharp current sheet. The implication is then, clearly, that the current sheet luminosity is directly related to the excitation of particles in the current conduction process, and, perhaps more interesting, the wavelike luminous profiles appear to be indicative of excitation of gas that has been swept over by the sheet but not completely entrained. Further, recently published work [34] with a clearly defined interaction between a projectile and an argon plasma has identified similar luminous profiles as shock wave profiles. Accordingly, the significance of these waves lies in their possible utilization as a diagnostic device for gas properties in the swept gas, if a flow velocity can be identified for that region. This topic will be given further consideration during the analysis of experimental data.

4.5 FLOW ISOLATOR STUDY

In the light of the above evidence that there is an interaction between the current sheet and probe, it is of interest to determine the most satisfactory configuration for the axial pressure probe. The radial probe shape can be considered satisfactory as it has been the subject of many gasdynamic analyses [35].

A continuum consideration of mass flow about an axial probe would predict stagnation of the gas on the forward-facing

54

T-3703

T-3705

$\dot{B}_\theta$

I

$t=1.9\mu sec$

$\dot{B}_\theta$

I
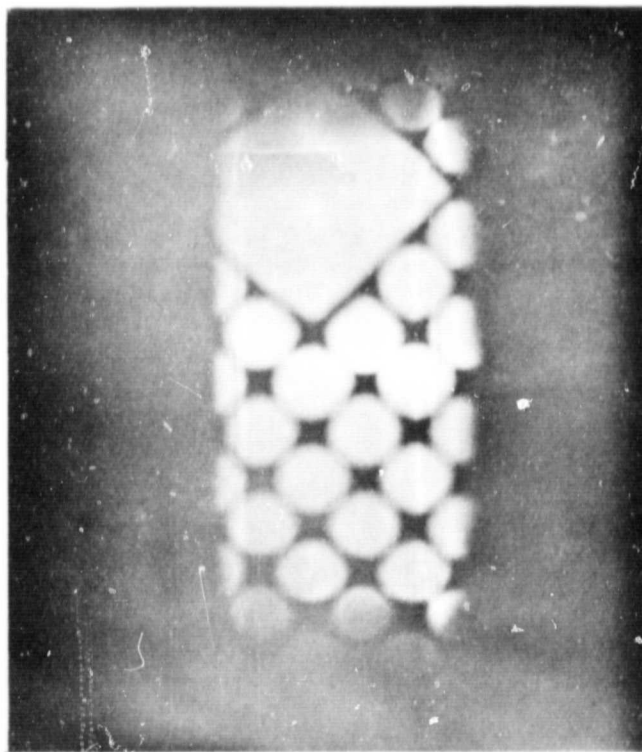
$t=2.1\mu sec$

T-3703
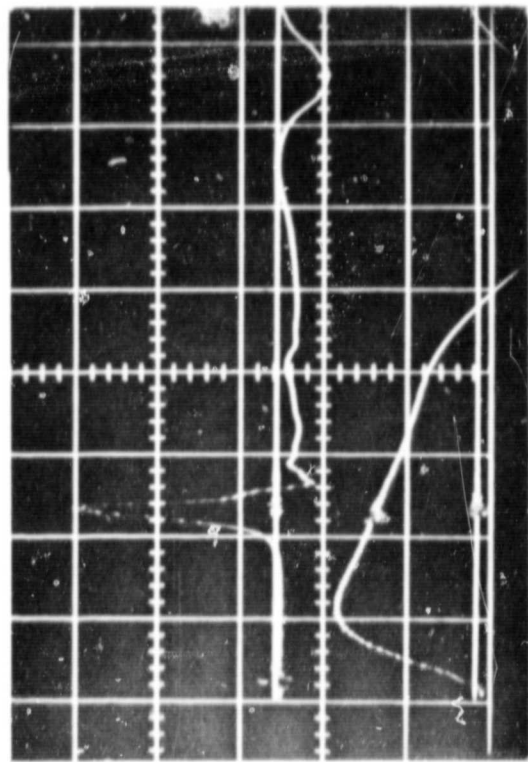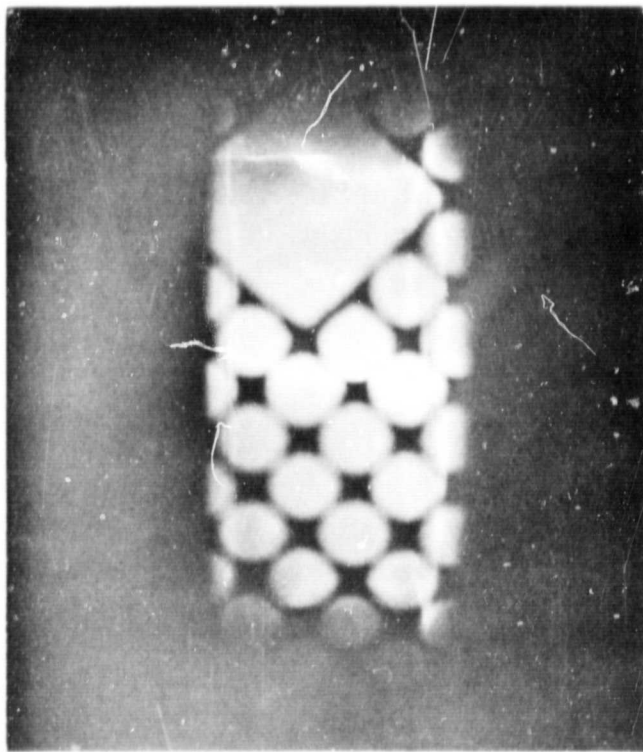
T-3705
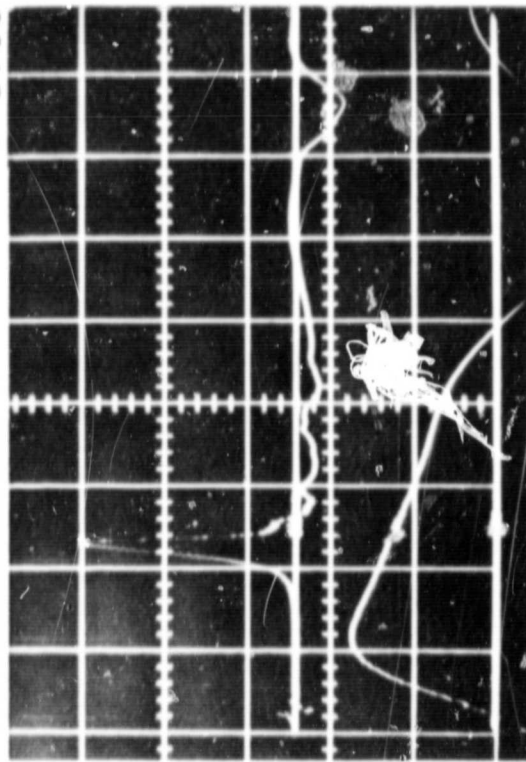
RADIAL–VIEW LUMINOSITY PATTERNS WITH SIMULTANEOUS MAGNETIC PROBE RECORDS

surface and expansion of this compressed gas over the sensing surface aligned with the flow. The expanded gas would interfere with a measurement of stream pressure, and so it would appear ideal to insulate the sensing surface from this effect by constructing such a "flow isolator" as used in the luminosity studies above. The output of adjacent magnetic and pressure probes for several isolator configurations is shown in Fig. 4-9. Comparing the results with the 1 1/2-in. isolator to those without any isolator, two important effects are evident. First, the use of the isolator produces a severe distortion of the current density profile due to the alteration of current conduction paths. On comparing the pressure records, it can be seen that the signal with the isolator indicates a uniformly low value after the current sheet passage, while an expanded flow region does appear to exist without the isolator during the same period. However, the pressure data of critical importance, that within the sheet structure, is not affected by such interference with, or without, an isolator. An intermediate size isolator (7/8 in.) can be seen to produce some distortion of the current density and to allow some expanded flow. In an attempt to evolve an optimum isolator, a 1 1/2-in.-diameter shape with sides cut away as indicated on the sketch, was evaluated; it was found to produce moderate current density distortion and to allow moderate expansion effects. In order to evaluate the effect of probe size on the data, axial data was also taken with the 5/16-in.-

T- 3576

$\dot{B}_\theta$

$P_Z(C)$

$\leftarrow$ 1 μ sec

CATHODE

MAGNETIC PROBE

ANODE

WITHOUT ISOLATOR

T - 3577

$\dot{B}_\theta$

$P_Z(C)$

$\leftarrow$ 1 μ sec

7/8"

ISOLATOR

T- 3578

$\dot{B}_\theta$

$P_Z(C)$

$\leftarrow$ 1 μ sec

1 1/2"
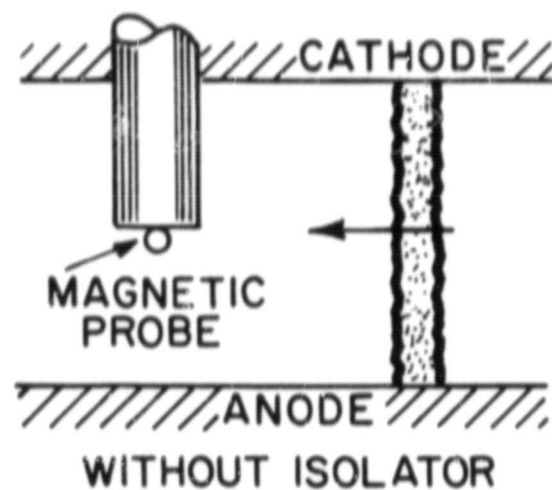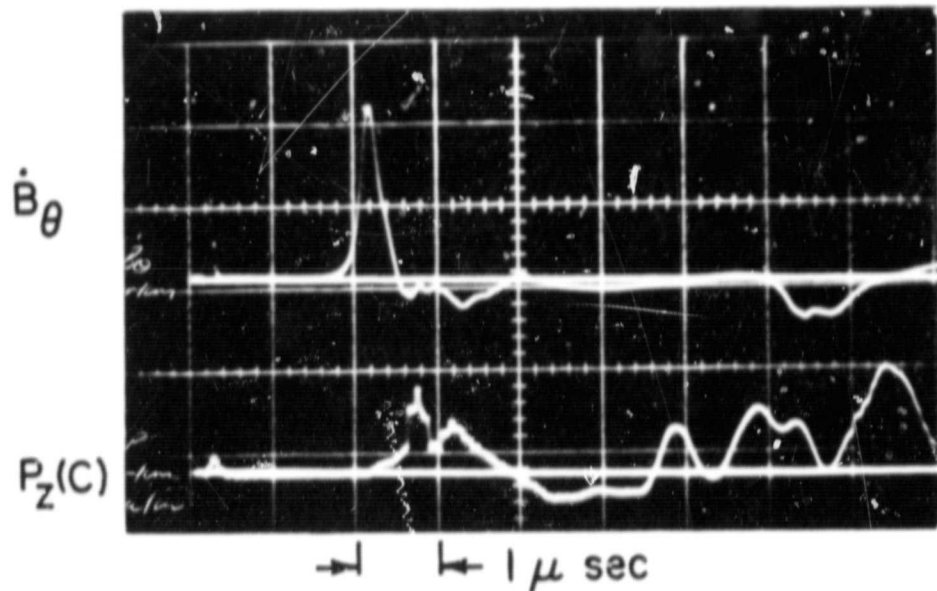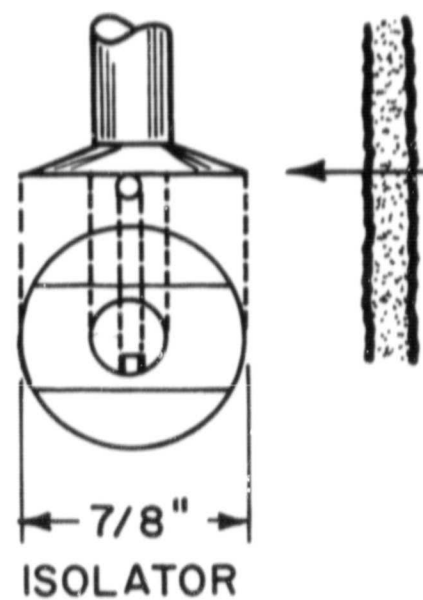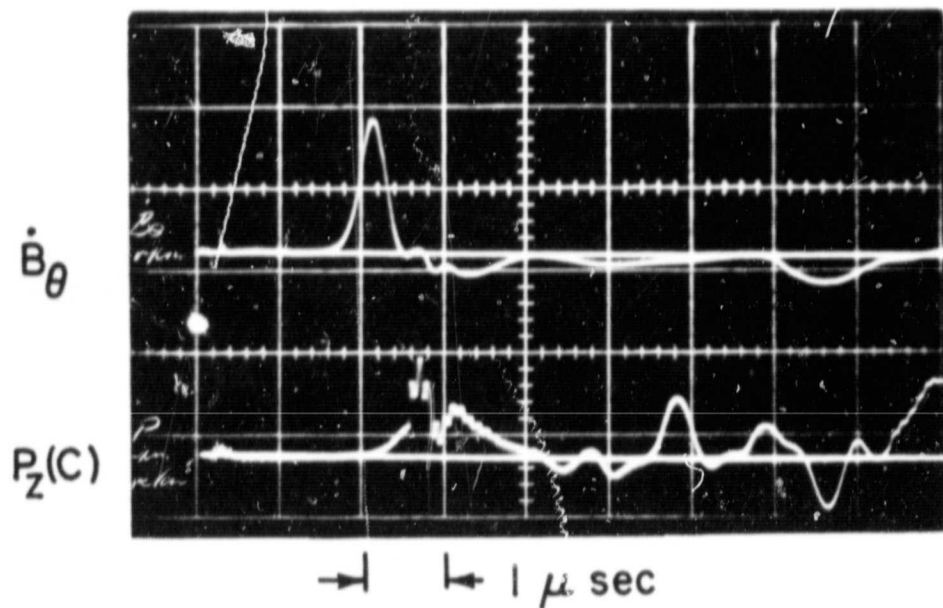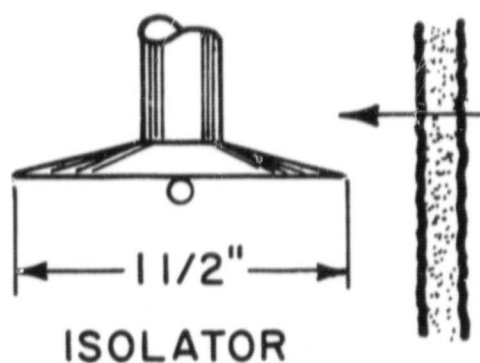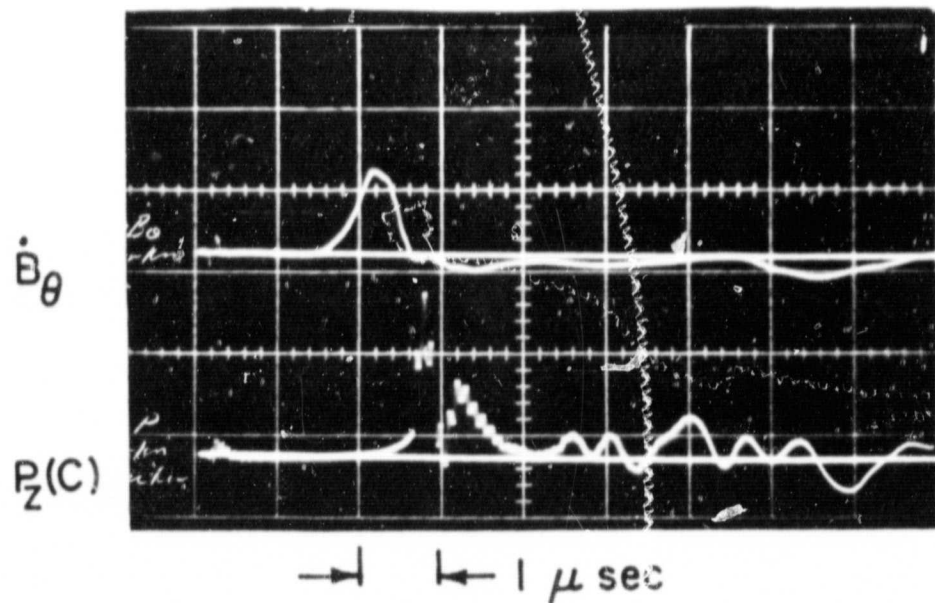
ISOLATOR

EFFECT OF FLOW ISOLATOR ON PROBE RESPONSE
(R = 2" ; h = 1")

FIGURE 1-2

o.d. radial probe; it compared favorably with data from the
1/2-in.-o.d. axial probe.

An effective probing of the current sheet interaction
can be carried out only with a current density profile free
of distortion, accordingly, the axial pressure probe must be
used without an isolator. It is evident from the above re-
sults that such a configuration does not distort the pressure
data within the current sheet profile, and for purposes of
analyses, the axial probe response can be treated as though
the element was embedded in a planar surface.

CHAPTER 5

EXPERIMENTAL DATA, EVALUATION, AND RESULTS

5.1 INTRODUCTION

In order to effectively monitor the structure of the sweeping current sheet, a compatible scheme for simultaneous probing was developed. Reduction of the data to consistent property profiles through the current sheet was carried out. In the case of pressure data, possible perturbations of sheet behavior inherent in probe response were considered. In order to provide a meaningful basis for current sheet analysis, profiles of the important variables within the current sheet will be presented.

5.2 PROBING CONFIGURATION

The effective analysis of current sheet structure requires a knowledge of a relatively large number of field and gas properties at each point. Specifically, azimuthal magnetic field records, radial and axial (anode, cathode) pressure measurements, radial and axial electric field data, along with total circuit current are of importance. It was clearly impossible to emplace probes for each of these properties and record accurate data in the same discharge; the required data were collected with several different probing arrangements and discharge shots. In order to circumvent the difficulties

of multiple shot correlation due to slight irreproducibilities in sheet arrival, the $\dot{B}_\theta$ record was specified as common, and all data were referenced to its profile. At any given point within the chamber the following data were recorded with one axial and one radial probe emplaced for each shot (Fig. 2-1); data were recorded on two dual-beam oscilloscopes:

Shot No. 1: P_r, E_z, I, $\dot{B}_\theta$

Shot No. 2: $P_z(c)$, E_r, B_θ, $\dot{B}_\theta$

Shot No. 3: $P_z(A)$, E_r, B_θ, $\dot{B}_\theta$

The basic criterion used for time correlation of any given set of records was the matching of the arrival time of 10 percent of $\dot{B}_\theta$ peak; this value was chosen since some distortion at later times was evident with magnetic probes built into axial probes. Further, P_z and E_r records were considered exact when both $\dot{B}_\theta$ and E_r reproduced from shot-to-shot.

Axial probes protruded through the ground electrode while radial probes extended through the pinch axis to the probe position on the far side to avoid distortion caused by the sheet sweeping over the probe support. In order to avoid interaction, each of these probes was separated azimuthally by a 30° angle at the same radius; at R = 2 in., this angle produced a nominal 1-in. separation. With such an arrangement, the correlation depended upon the local azimuthal symmetry of the discharge. Discharge patterns were established by axial-view, Kerr-cell photographs similar to those noted earlier (Fig. 4-7).

Specific local symmetry was established by comparison of the
data records of several variations of probe orientation. With
the radial E probe defining a reference, the axial pressure —
B_θ probe was positioned 30° clockwise off axis; a second shot
was taken with the axial probe 30° counterclockwise off axis;
and a third shot was made with the positions reversed — the
axial probe on axis and the E probe positioned 30° counter-
clockwise away. A comparison of the above data showed excellent
reproducibility of profiles and arrival time within the cur-
rent sheet; accordingly, it was concluded that the probing con-
figuration would provide accurate simultaneous current sheet
data.

5.3 CURRENT SHEET MEASUREMENTS

With the procedures defined above, current sheet data
were recorded along the electrode midplane at radii from 3 to
1 1/2 inches. At larger radii the initial burst of noise
generally obscured any real data record and at radii smaller
than 1 1/2 in. the anode "foot" extended beyond the midplane,
distorting the intense current sheet. Typical data records of
current, electric field, magnetic field, and pressure at one
point in the chamber are presented in Fig. 5-1; the data have
been corrected for the slight irreproducibility in current
sheet arrival. The notation P_z(c) refers to axial pressure
with the probe mounted on the cathode. Complementary data
showing the variation of axial (c) pressure and $\dot{B}_\theta$ with radius
are presented in Fig. 5-2. In order to clarify the detailed

REGIONS: I II III ^{61}

$\longmapsto$ I μ sec/DIV

I

E_Z
(2. v/Div)

T-3625

E_r
(2. v/Div)

B_θ

T-3620

$\dot{B}_\theta$

P_R
(20. v/Div)

T-3625

$P_Z(C)$
(.5 v/Div)

T-3620

$P_Z(A)$
(.5 v/Div)

T-3623
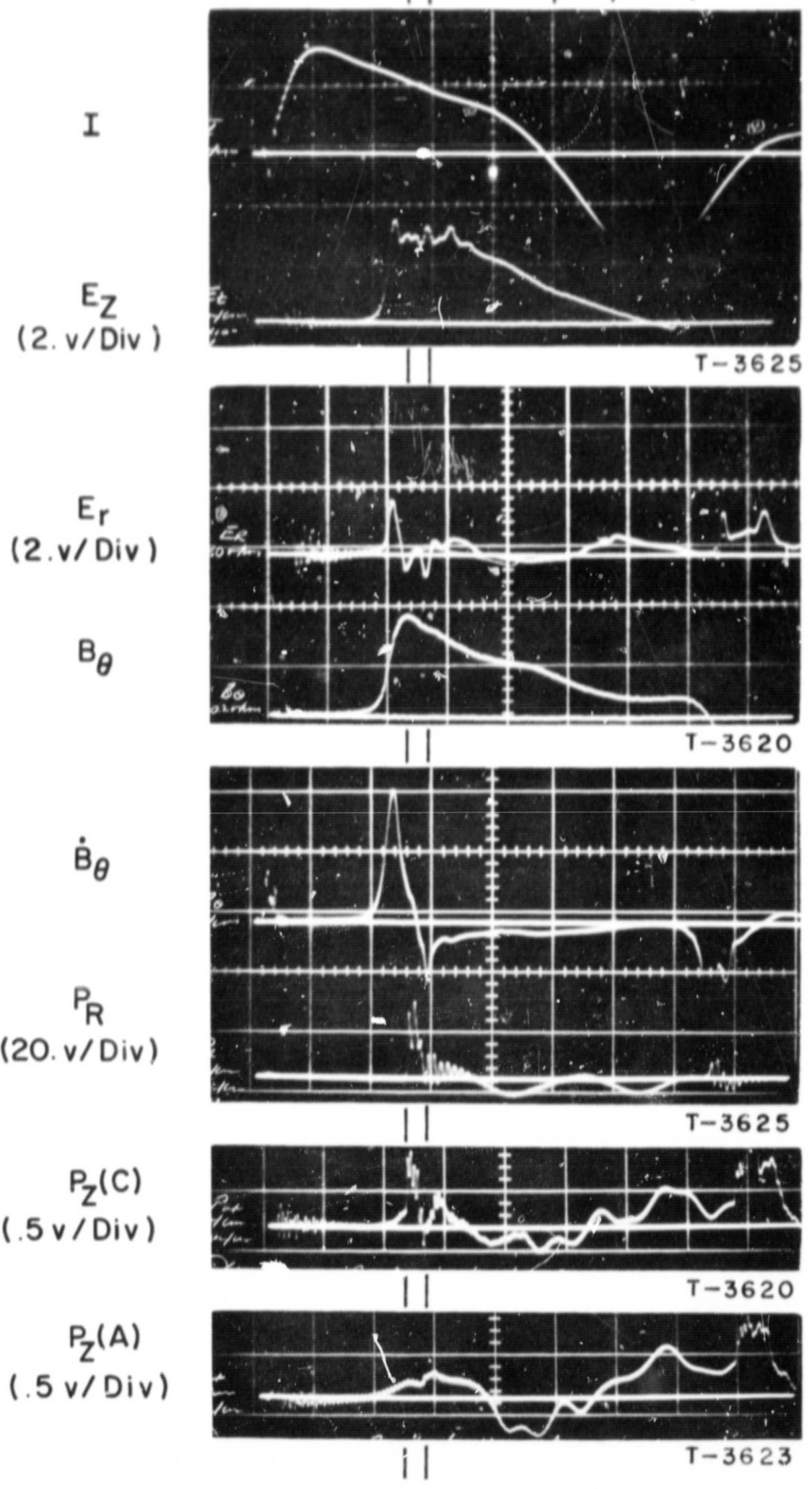
TYPICAL PROBE RESPONSES

R=2", h=1"

FIGURE 5-1

AP 25 P-197 A 68
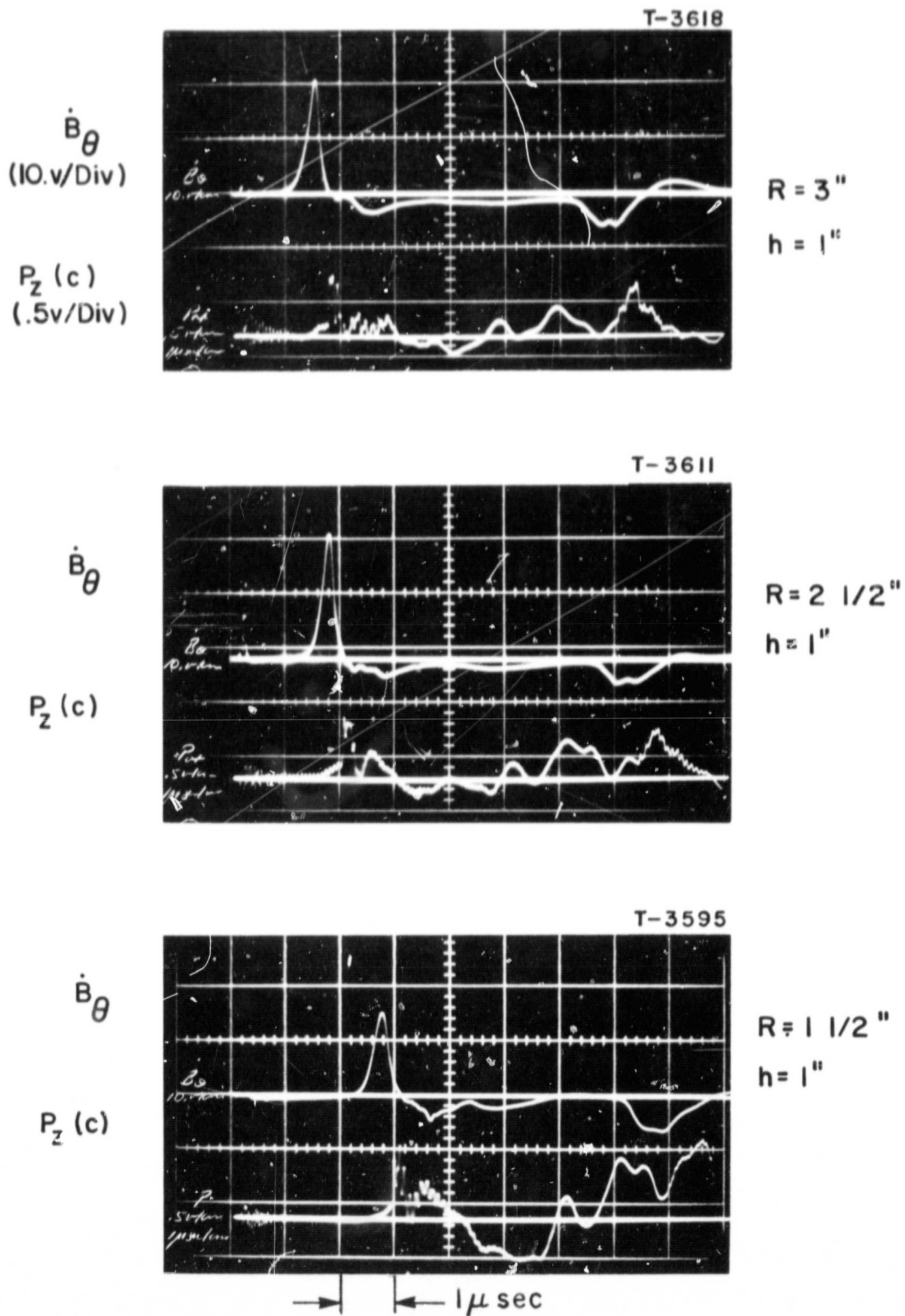
RADIAL VARIATION OF MAGNETIC FIELD AND AXIAL PRESSURE

FIGURE 5-2

response of the radial pressure probe during the critical
initial signal period, data are presented with a sensitivity
equal to that of the axial pressure measurements; Fig. 5-3
shows a typical response.

5.4 CURRENT SHEET CHARACTERISTICS

From data such as that presented above, it is possible
to define some characteristics of current sheet dynamics and
current sheet structure. First, the experimental data confirm
the existence of a discontinuous region of strong pressure re-
sponse within the current sheet. It can clearly be seen that
the discontinuous pressure rise occurs significantly after the
peak of the current density profile; moreover, following this
compression, the existence of a sharp expansion within the
sheet structure is also experimentally confirmed. In order to
establish clearly the dynamics of the current sheet, the tra-
jectories of $\dot{B}_\theta$ peak and the pressure front discontinuity are
presented in Fig. 5-4. It can be seen that the pressure dis-
continuity travels at a slightly lower velocity than the cur-
rent sheet, resulting in an increasing separation as the sheet
implodes. However, in both cases the sheet velocities are
effectively constant over the region of interest—a fact of
considerable significance in the reduction of data.

More critical than the dynamics of the current sheet
are some implications regarding current sheet structure evi-
dent in Fig. 5-1. Upon considering the two records of axial
pressure, it is clear that these pressures recorded at the

$\dot{B}_\theta$
(10.v/Div)

P_R
(.5v/Div)

$1\,\mu$ sec
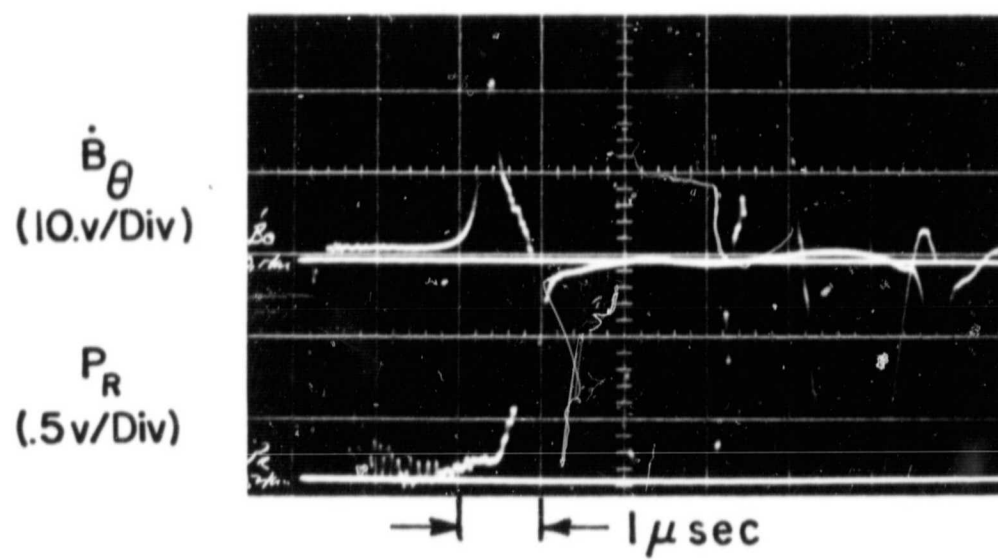
INITIAL RESPONSE OF RADIAL PRESSURE PROBE
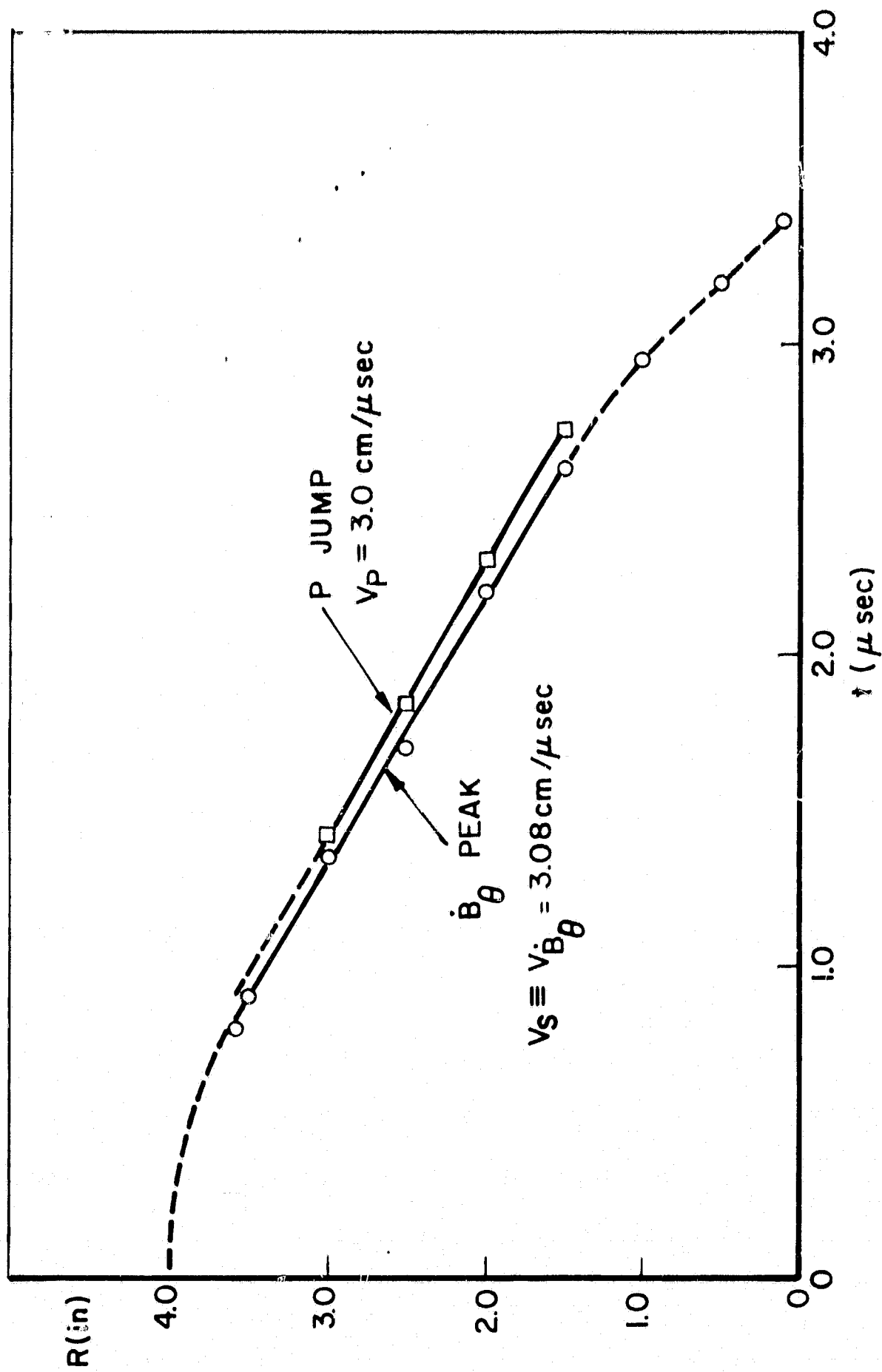
FIGURE 5-3

CURRENT SHEET TRAJECTORIES

FIGURE 5-4

same point but with opposite orientation about the electrode midplane, are not identical. The differences appear to indicate three different zones of interaction within the current sheet structure. The initial zone (I, as noted in the figure) is characterized by approximately equal pressure records with anode or cathode mounting, intense current flow $(\dot{B}_\theta)$ and strong electric fields (E_z and E_r). Further, from Fig. 5-3, the radial pressure record, which is proportional to particle density and directed particle velocity, also shows a very weak signal of the same order as the axial measurement. Such response defines region I as a zone of high-current flow but little mass accumulation. The absence of mass accumulation in this zone is further indicated by the constancy of the pressure profile in region I while the current sheet implodes, as evidenced in Fig. 5-2. The axial electric field (E_z) can be attributed to both a resistive (ohmic) voltage drop and a motional induced (u x B) component, while the radial electric field indicates charge separation and electron current conduction (Chap. 6).

The discontinuity (rise and fall) in the radial and cathode mounted pressure probe response defines the boundaries of a second (II) zone. The two axial pressure records exhibit a significant difference in their response in this region; this fact along with the magnitude of the radial probe signal suggests a region of intense particle concentration. The large values of axial electric field suggest both ohmic and motional components, but the absence of measurable radial electric fields

indicates a balance of charged particles; there are relatively
small but positive currents flowing in this region. The asym-
metry in the axial pressure measurements must be related to the
tilt of the current sheet and inclination of the flow field,
with the resultant conduction of current (streaming toward the
cathode) by ions.

The third zone of interaction (III) is typified by ap-
proximately equal axial pressure measurements, small output
signal from the radial pressure probe and very low current den-
sity. This region is made up of gas that has been passed over
by the intense current sheet layer, but not entrained. The
fact that an induced flow field exists is evidenced by the
large axial electric field measured with little current flow
and the luminous wave patterns that have been observed and in-
vestigated earlier.

The above qualitative considerations have been pre-
sented in order to clarify the general nature of the current
sheet behavior and so to provide a basis for more detailed dis-
cussion of the structure that will follow.

5.5 ESTIMATION OF NUMBER DENSITY AND PARTICLE TEMPERATURES

In order to carry out an order of magnitude evaluation
of perturbation effects on the pressure data, it is necessary
to have reasonable estimates of both particle number density
and particle temperatures. From the above discussion there
are evidently three zones of interaction, and so an estimate
of both variables for each zone is desired.

First, regarding number densities, it will be speci-
fied that electron and ion densities are effectively equal
on the basis of Gauss' law

$$\nabla \cdot \overline{E} = \frac{\rho_e}{\epsilon}$$

where ρ_e is the net charge density and $\overline{E}$ is the electric
field. With the radial electric field being the significant
electric field component in the sheet frame, Gauss' law takes
the form

$$\frac{\partial E_r}{\partial r} = \frac{\rho_e}{\epsilon}$$

With a typical electric field increment of 20 volts across
0.5 cm, a charge imbalance of 10^{-14} coulomb/cm^3 is equivalent
to a number density of 10^5 electrons/cm^3 or approximately a
ratio of 10^{-11} over the anticipated charged-particle density.
Accordingly, the approximation that $n_i \approx n_e$ will be applied
throughout the sheet.

In an attempt to establish orders of magnitude of par-
ticle densities in the various regions, the radial pressure
data will be used with the following understanding. First,
the radial pressure measurement is one of momentum transfer
from directed kinetic energy of the heavy particles with an
order of magnitude of 180 ev. Perturbations due to the sev-
eral ev electrostatic sheath drop would not greatly affect the
trajectory of such high energy particles; further, the assump-
tion of inelastic collision of non-interacting particles with

the probe surface will be made. The validity of such an

(Newtonian) assumption will be discussed in more detail later.

On this basis then, the radial pressure can be related to num-

ber density (n) and particle velocity (v) by

$$P_r \approx nmv^2$$

Taking the approximation of sheet velocity for particle veloc-

ity, the radial probe output indicates number densities of the

following order:

$$n_I < 10^{16}/cm^3$$

$$n_{II} \approx 10^{17}/cm^3$$

$$n_{III} \approx 10^{16}/cm^3$$

compared with an ambient number density of $n_o = 3 \times 10^{15}/cm^3$.

Further, on the basis of the microwave diagnostic work of

Ellis [14] in such a discharge, it will be assumed that the

ambient gas reaches a degree of ionization of 10 percent shortly

after initiation of the discharge, due to precursor effects.

The estimation of particle temperatures in the various

regions becomes a much more subtle and difficult task due pri-

marily to the high degree of nonequilibrium within the current

sheet. However, the separation of the current sheet into zones

of interaction can be used to alleviate the difficulty of such

an analysis. It has been specified that region I is a zone of

intense current conduction and apparently intense electron ac-

tivity. In a frame of reference fixed with the sheet, the elec-

tron population will receive energy primarily from ohmic heating.

An upper limit on this loss mechanism can be estimated from measurements of voltage drop across the current sheet by inner divider voltage measurement techniques (Appendix C). Such voltage records indicate a typical voltage drop across the current sheet of 80 volts and, accordingly, a power input at $R = 2$ in. to the electron swarm of

$$P(R = 2 \text{ in.}) = \Delta V_{inner} \cdot I \approx 20 \times 10^6 \text{(joule/sec)}$$

The primary loss mechanisms for the electron swarm are radiation, heat conduction, and inelastic collision with heavy particles. The radiation and conductivity losses have been estimated to be unimportant for the environment under consideration [13], and, accordingly, the inelastic energy transfer mechanism must be dominant. The excitation of argon atoms to ionization has been investigated by Petschek and Byron [37] and more recently by Harwell and Jahn [38] who established that the ionization process occurs via a two-step process. It was found that the activation energy coincided with the first excitation potential of the atom and that ionization would occur with a second inelastic electron-atom collision. Accordingly, the rate of energy loss per cubic centimeter per second to ionization by inelastic collisions can be expressed:

$$Q_{in}\left(\frac{\text{Joule}}{\text{cm}^3 \text{ sec}}\right) = 11.3 \times 10^{-28} n^2 T_e^{1/2}(11.5 + 2T_e)e^{-11.5/T_e}$$

where T_e is in ev and number density is per cm^3. For the case of a current sheet 0.5 cm wide at a 5 cm radius, the plasma volume is 80 cm^3; with a number density of $10^{16}/cm^3$, equating

power input with power loss indicates an electron temperature of

$$T_e(I) \approx 4.0 \text{ ev}$$

The corresponding time interval to excite a neutral argon atom to its first activation level is 0.12 µsec—a figure that would indicate significant levels of ionization within the current density profile due to electron-atom inelastic collisions. It should also be noted that the high energy tail of the electron distribution is providing the necessary ionization energy increment.

As a complementary indicator of ionization profiles within the current sheet, some time resolved spectroscopic studies carried out by von Jaskowsky [39] in a 5-in. diameter pinch discharge are of interest. Profiles of argon II radiation were found to peak slightly ahead of the peak in total light intensity, whereas argon III radiation was found to peak at the same time as total light. As the earlier studies have indicated a direct correlation between light and current conduction, the argon line profiles appear to reinforce the conclusion that the region of intense current flow is also a source region for ionization; significant amounts of first ionization appear to be achieved early in the current sheet structure.

In order to establish an estimate of ion temperature in the highly nonequilibrium current conduction zone, it is necessary to consider the possible heavy particle collision

processes. First, regarding the electron-ion collisions, it is of interest to examine generally the relaxation time for thermal energy transfer between the two species. Following Spitzer [40], the time to establish equipartition of energy between two groups of particles, each with a Maxwellian distribution but with different temperatures, can be approximated for $T_A/m_A \ll T_e/m_e$ as

$$t_{eq} \approx \frac{3 \, m_i \, (kT_e)^{3/2}}{8 (2\Pi m_e)^{1/2} \, n \, e^4 \, \ln \lambda}$$

Taking $T_e = 4.0$ ev, $n \approx 10^{16}/cm^3$, and $\ln \lambda \approx 6.0$

$$t_{eq} \approx 1.3 \text{ sec}$$

Accordingly, with this estimate as an order of magnitude indicator, it will be assumed that the two species are effectively thermally insulated from each other on the time scale of the event.

On the basis of the above discussion then, the primary mechanism for heating the heavy particles appears to be the argon-argon, short-range collisions. An estimate of these effects will be carried out using the collision data summarized by Jahn [15]. Considering first the case of a static argon atom colliding with entrained argon ions within the sheet at a relative kinetic energy of 180 ev, the elastic scattering cross section is $Q^{(el)} \approx 2 \times 10^{-15}$ cm^2 and the charge-transfer cross section is $Q^{(t)} \approx 2 \times 10^{-15}$ cm^2. Accordingly, with an

ion density of $n_A \approx 10^{16}/cm^3$, the mean free path for atom-ion collisions is approximately

$$\lambda_{A-i} = \frac{1}{n_A \cdot Q_{A-i}} \approx 10^{-1} \text{ cm}$$

a figure indicative of significant energy transfer in the 1 cm thick zone. Further, the atom-atom ionization cross section at 180 ev is $Q^{(i)} \approx 0.5 \times 10^{-16}$ cm^2 and the ion-ion elastic cross section $Q^{(\epsilon)} \approx Q^{(p)} \approx 10^{-12}/\epsilon^2 \approx 10^{-16}$ cm^2. While it does not appear possible to establish a single collision process as the dominant energy transfer mechanism in the collision hierarchy, it can generally be concluded that the conditions within the regions of particle concentration (I and II) are appropriate for considerable thermalization of the available relative kinetic energy of the streaming argon particles. Some limits on the heavy particle temperatures that may result in such a system can be derived by a brief consideration of an energy balance.

From a frame of reference fixed with the constant velocity current sheet, the swept particles must deposit the relative kinetic increment ($E_{kin} \approx 180$ ev) in one of the several available modes. This energy can reside as thermal energy with related radiation, and axial ion streaming. If the total energy was converted to translational (random kinetic) motion, an upper limit of $T_A \approx 100$ ev would result. However, such an extreme value suggests that a possible energy balance might be met by equating thermal gain with radiative loss for a system of

snowplowed particles. Specifically, at R = 2 in., equating

thermal gain with black-body radiated loss,

$$E_{TH} \cdot n_o \cdot \pi(R_o^2 - R^2) \cdot h = \int_0^t 2 \cdot 2\pi R \cdot h \cdot \sigma_R T^4 \, dt$$

where σ_R is the Stefan-Boltzmann constant. With E_{TH} = 100 ev,

a heavy particle temperature of about 2 ev is indicated—estab-

lishing a lower limit on the possible argon temperature. A

more detailed calculation of temperature on an energy basis

does not appear reasonable with the present state of under-

standing of such a plasma, however, a general accounting of

energy deposition within the current sheet will be presented

later.

In order to carry out the desired heavy particle tem-

perature estimate, the equilibrium equation of state, $p = nkT$,

will be used with approximate pressures and number densities.

For region I, an approximate static pressure of 0.1 atm with

a number density of $10^{16}/cm^3$ indicates a temperature of

$T_A(I) \approx 10$ ev. Similarly, for the region of mass accumulation

(II) an estimated pressure of 1.0 atm with a number density of

$10^{17}/cm^3$ implies that $T_A(II) \approx 10$ ev, in reasonable agreement

with the above energy considerations. With such a proposed

equilibrium temperature, it can be expected that an incoming

ion would reach translational equilibrium with the system in

a few collisions. However, as noted earlier, the electrons

would not be able to absorb thermal energies of this magnitude

on the time scale of the event. Accordingly, it will be
assumed that

$$T_e(II) \approx T_e(I) \approx 4.0 \text{ ev}$$

The particles that can be found in the region behind
the intense current sheet (III) have passed through the vig-
orous interaction zone but can be expected to approach thermal
equilibrium more closely because of the longer available re-
laxation time. A temperature estimate can be carried out
using the luminous wave profiles about the various probe shapes.
Henderson [34] identified such luminosity as an indicator of
heavy particle compression and heating across a shock, and
that interpretation can be applied here. Further, detailed
gasdynamic studies of low density gas flows have utilized the
glow discharge method of visualization [41], a technique with
very similar electrode components naturally available in the
pinch discharge, resulting in a close identification of such
luminous patterns with shock wave profiles. From luminosity
profiles such as those presented in Fig. 4-6, with a flow in-
clination of 5°, and an approximate shock angle of 20°, the
estimated Mach number would be $M_{III} \approx 3.5$. Taking flow ve-
locity in this region as $1/2 \ V_s$ (Chap. 7), the indicated
sound speed would then be

$$a = \frac{V}{M} \approx \frac{1/2 \ V_s}{M_{III}} = 4.3 \times 10^3 \text{ m/sec}$$

With an estimated pressure in this region of 1 atm, this value

of sound speed would correspond [42] to a temperature of

$$T_A(III) \approx T_e(III) \approx 3.0 \text{ ev}$$

which is in reasonable agreement with other data.

With the above estimates of number density and temperature, an evaluation of perturbations to the pressure measurements can be carried out.

5.6 EVALUATION AND REDUCTION OF PRESSURE PROBE DATA

The data that have been recorded with the pressure probe structure immersed in the stream of moving plasma are subject to two major perturbations: those of the electro-static sheath surrounding the probe, and those related to the viscous and compressible fluid mechanics of the gas moving past the probe surface.

Regarding the electrostatic sheath perturbation, the insulating surface of the probe will allow no net current to flow from the plasma and so the probe will assume floating potential (V_f), slightly negative with respect to the plasma (V_p). With the orderings on number density and temperature presented above, the important sheath parameters - the ion mean free path $(\sim 10^{-4} - 10^{-5} \text{ m})$ and Debye length $(\sim 10^{-7} \text{ m})$ - are related as

$$\lambda \text{ (ion mfp)} \gg h \text{ (Debye length)}$$

and since the sensing element is embedded in a plasma surface, the sheath meets the constraints of classical Debye shielding for a plane nonconductor [17]. However, the effects of such a sheath on the pressure sensed at the probe surface can be

shown to be independent of the sheath structure and detailed
particle behavior.[*] First, it will be noted that the sheaths
under consideration can be seen to demonstrate a large value of
electron flux relative to ion flux, in the ratio $(T_e/m_e)^{1/2}/(T_i/m_i)^{1/2}$.
As such, a calculation of sheath formation time must consider the
response of the ions in order to derive an upper limit for this
parameter; specifically for 10 ev ions,

$$v_i = \left(\frac{kT_i}{m_i}\right)^{1/2} \approx 10^3 \text{ m/sec}$$

and the Debye length for a sheath with 4 ev electrons,

$$h(m) = \left(\frac{\epsilon_o \, kT_e}{n_e \, e^2}\right)^{1/2} \approx 10^{-7}$$

so the time for the ion component to adjust can be approximated
as 10^{-10} sec. Accordingly, the sheath can be assumed to be al-
ways in phase with the plasma, and steady flow of the particles
through the sheath can be assumed. The physical geometry to be
considered in the sheath analysis is illustrated in Fig. 5-5
where it should be noted that surface ③ is defined where local
$\bar{E}$ is zero, and surface ① is taken within the insulator, and
includes the surface electron layer, so that $\bar{E}$ at ① is zero
also. An appropriate conservation of momentum for this control
volume can be written

$$\int_V [\nabla \cdot \rho \, \bar{v} \, \bar{v}] dV + \int_V (\nabla p) dV + \int_V [\nabla \cdot \tau] dV = 0$$

where v is the particle streaming velocity and τ is the
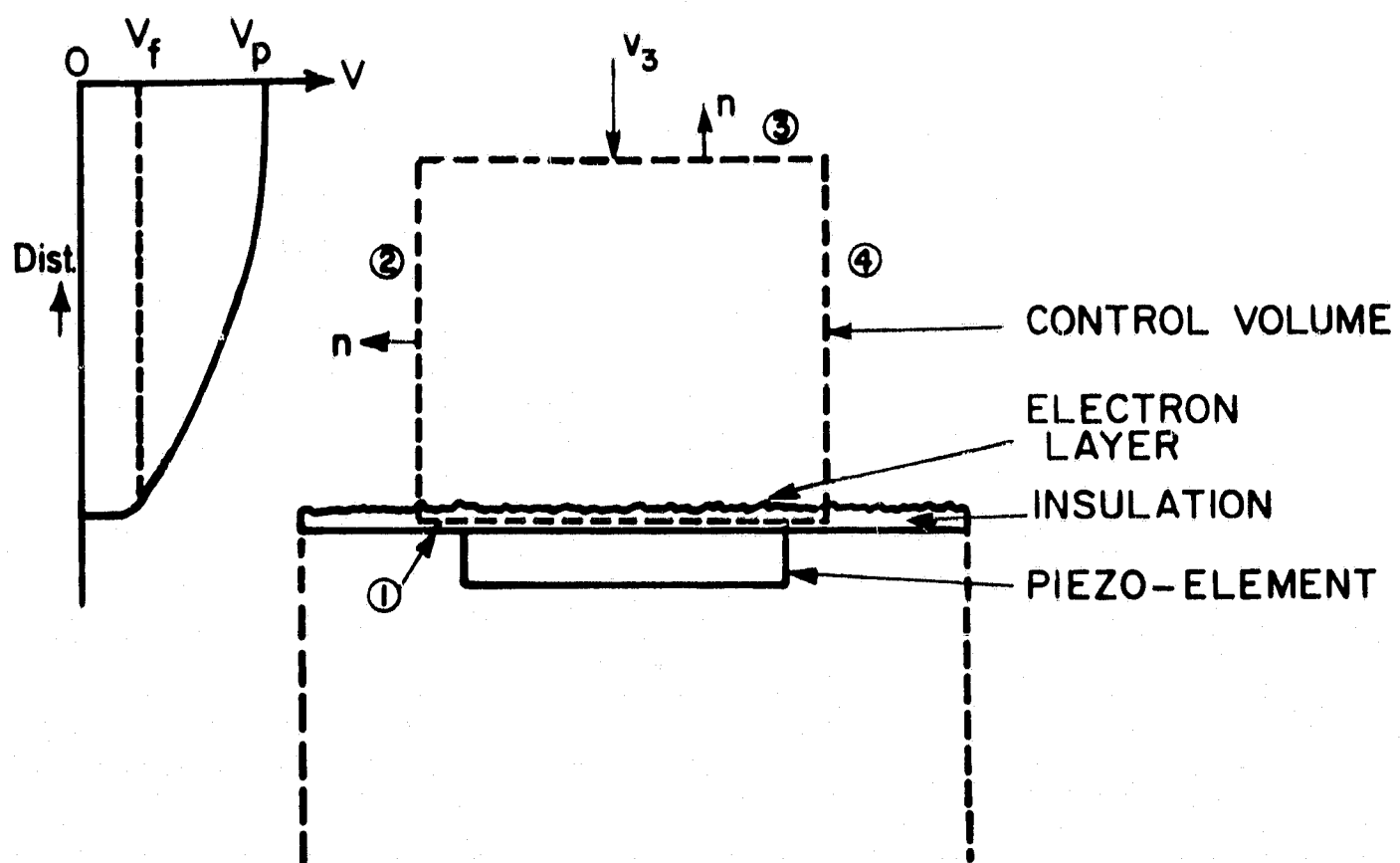
CONTROL VOLUME FOR ELECTROSTATIC SHEATH CALCULATION

FIGURE 5-5

electromagnetic stress tensor, $\tau_{ij} = D_i E_j + B_i H_j - 1/2$ $(D_k E_k + B_k H_k)\, \delta_{ij}$. The integrals can be transformed to surface integration, as

$$\int_S \rho\, \overline{v}(\overline{v} \cdot \overline{n})\, dS + \int_S p\overline{n}\, dS + \int_S [\tau \cdot \overline{n}]dS = 0$$

and the integration carried out for the four surfaces defined in the figure. Accordingly,

if $v_3 = 0$ then $p_1 = p_3$

and if $v_3 \neq 0$ then $p_1 = p_3 + nmv_3^2$

or, the pressure transmitted to the sensing element (p_1) is <u>not</u> influenced by the existence of a surface electrostatic sheath.

An analysis of gasdynamic interaction effects on the pressure data must take as its focal point the experimental results presented in Fig. 4-9, where it can be seen that very significant alterations of the probing shape produced only slight variations in the resultant axial pressure profiles within the current sheet. Apparently, the axial probe data can be treated as though the element was embedded in a flat plate. Such behavior appears to indicate that the response is related to local conditions rather than the overall flow field about the probe shape. This type of interaction can be described basically by the Newtonian approximation, valid for steady-state hypersonic flow or unsteady, adsorbing (cold wall) flow on a short time scale; the latter appears to be compatible with the present case. However, since the predictions of classical compressible flow in the limit of large M and small γ agree with Newtonian results, the general steady-state interaction will first be

considered and then evaluated for the appropriate limiting conditions.

The evaluation of gasdynamic effects will depend upon a number of parameters, most basic of which is the Mach number, defined locally as $M = v/a$, where a is acoustic velocity. Approximating the particle velocity by sheet velocity and using the heavy particle temperatures for sound speed in regions I and II, with M_{III} indicated above, there results

$$M_I \approx 3.0 \quad , \quad M_{II} \approx 3.0 \quad , \quad M_{III} \approx 3.5$$

It should be noted that the assumption of sheet velocity for evaluating M_I can be expected to be excessive for the primary phase of argon acceleration, but it is used only to establish an order of magnitude.

For the axial probe configuration, the shock wave, boundary layer analysis of the current sheet interaction will treat each sheet region independently in an attempt to estimate the gasdynamic effects on the pressure data. Because of the size ($\sim$ 1 cm) of the axial probe and the Mach numbers involved, it is of interest to consider the possible effect of viscous interaction in each of these three regions. Following Hayes and Probstein [43], the quantity of interest is the hypersonic interaction parameter

$$\overline{\chi} \equiv \frac{M^3 \sqrt{C}}{\sqrt{Re_x}}$$

where C is a constant dependent on the temperature-viscosity law, and Re_x is a Reynolds number based on length. When the

viscosity is evaluated for highly ionized argon [40], and approximate values are taken for the remaining variables, the following results are indicated:

$$\overline{X}(I) \approx 2.0 , \qquad \overline{X}(II) \approx 0.6 , \qquad \overline{X}(III) \approx 0.15$$

Accordingly, each of the three regions can be approximated by weak interaction theory, i.e., the effects produced by the self-induced (i.e., boundary layer growth) pressure gradient are small.

The pressures recorded in region I with both axial probe orientations and the radial probe are all effectively equal. The fact that there is little evident difference between stagnation and static pressures is a clear indication that gasdynamic interaction has little measurable influence on the pressure recorded in region I. Such behavior would be more compatible with a lower (< 1) Mach number flow than that indicated above. In this context, where estimates of number density determined independently (Chap. 6) and the indicated pressure are combined in the equation of state, p = nkT, a temperature variation from zero to 30 ev is indicated. When these estimates are combined with a velocity variation from zero to $1/2V_s$ (Chap. 6), lower Mach numbers (< 1) are indicated. Accordingly, it will be assumed that the pressures measured in this zone are approximately equal to pressures within the sheet for this region (I).

The relationship between measured pressure and sheet pressure in the more dense region can be carried out in the following manner. It has been noted [43] that the inequality

$$\left(\frac{\delta}{x}\right)^2 << \epsilon$$

where δ is boundary layer thickness, and $\epsilon = \rho_\infty / \rho_s$ specifies the condition for separation of the flow field into regions of classical shock wave and classical boundary layer behavior. Further, since

$$\frac{\delta}{x} \approx \frac{\gamma - 1}{2} \frac{M_\infty^2 \sqrt{C}}{\sqrt{Re_x}} \approx \frac{\overline{\chi}}{M}$$

Then

$$\left(\frac{\delta}{x}\right)_{II} \approx 0.2$$

and

$$\left(\frac{\delta}{x}\right)_{III} \approx 0.04$$

With reasonable estimates of the density ratio, the above inequality is satisfied in both regions II and III and so a separated flow field analysis can be applied. Further, with the boundary layer approximation, the variation of pressure across the viscous layer can be considered negligible, and the primary perturbation between the current sheet and measured pressure values is then the pressure change across a shock wave or an expansion wave. Taking the R = 2 in. data as typical, from the current sheet tilt and wave deflection data, a flow inclination of 5° toward the cathode is indicated. Accordingly, the probe data on the cathode would be subject to compression, and that on the anode to expansion through that angle. With the given flow inclination and approximate Mach number, the pressure ratio across a shock with small flow deflection angle (θ)

can be expressed [35] as

$$\frac{p}{p_\infty} = 1 + \frac{2\,\gamma}{\gamma + 1}\,(K_s^2 - 1)$$

where

$$K_s = M\,\beta = \frac{\gamma + 1}{4}\,(M\theta) + \sqrt{\left(\frac{\gamma + 1}{4}\,M\theta\right)^2 + 1}$$

and for an expansion through angle θ as

$$\frac{p}{p_\infty} = \left(1 + \frac{\gamma - 1}{2}\,M\theta\right)^{-\frac{2\,\gamma}{\gamma - 1}}$$

An approximate $\gamma = 1.2$ is selected based on tabulated high

temperature argon properties [42] for the conditions compat-

ible with the indicated ionization and the compatible relation-

ship of shock angle (β), θ, and M from experimental estimates.

Accordingly, for region II with $M_{II} \approx 3.0$, the pressure ratios

of 1.33 and 0.70 are indicated for the compression and expansion,

respectively. For region III, it is more convenient to use the

measured wave angle, $\beta \approx 20°$, with $M_{III} \approx 3.5$ to estimate

$p/p_\infty \approx 1.5$ for the compression and 0.68 for the expansion.

Before the relationship of probe output to sheet static

pressure can be carried out, the spatial resolution of the probe

must be considered. Again, the probe surface is about 4 mm in

diameter, which with sheet speeds of 3×10^4 m/sec indicates a

period of 0.125 μsec for an infinitesimally thin profile to

sweep past that surface. Since the signal response in regions

I and III varies continuously on such a time scale, the output

in these regions can be assumed to be directly proportional
to the average sheet pressure being sensed. However, region
II is unique with its evident discontinuity at beginning and
end of the signal, so that the output signal is proportional
to the average pressure on the probe surface, and not average
pressure in the sheet region. Specifically, the time interval
between signal rise and fall in region II (Δt) can be taken as
an indicator of the thickness of the dense region (δ), as

$$(\Delta t - t_{sweep})\ V_s \approx 1.3\ mm$$

for the 2-in. radius. Taking a plane-slab approximation of the
dense layer 1.3 mm thick, the slab area in contact with the
transducer (A_p) can be calculated as a function of time from
simple geometrical considerations. Accordingly, recalling that
the probe output is proportional to the ratio ($\bar{A}_p/A_s$), Eq. (3-3),
the value of sheet pressure can be determined when A_p is known
for an appropriate probe signal.

The evaluation of average static pressure within region
II is determined from analysis of the axial pressure data, based
on estimates of number density and argon temperature from radial
pressure data. The basic data (Fig. 5-1) indicate values of
measured pressures of $P_Z(c) = 3.0$ atm and $P_Z(A) = 1.0$ atm. With
a dense layer thickness of 1.3 mm, the area in contact with the
crystal can be calculated; accordingly, $A_p/A_s \approx 1.5$. This
factor, along with a factor to account for the gasdynamic com-
pression or expansion, when applied to the measured values of
pressure, indicates an average pressure in the entrained region

of $P_{stat}(II) = 3.5$ atm. It is also of interest to note that
the axial (c) pressure corrected for the area ratio becomes
4.5 atm.

The pressure data that have been recorded with the radial
probe configuration must also be evaluated for gasdynamic effects.
However, the gasdynamic interaction of a right-cylinder of revo-
lution, with its axis aligned in the flow direction, can be con-
sidered well-known [35,43]. The sensing surface was mounted
within the cylinder end--perpendicular to the flow direction--
and so a blunt-body analysis is appropriate. A steady-state
hypersonic analysis for such a configuration [44] predicts
stagnation surface pressures as

$$p = \left[1 - \frac{1}{2}\left(\frac{\gamma - 1}{\gamma + 1}\right)\right]\rho_0 v^2$$

In the present application with $\gamma \approx 1.2$,

$$p \approx \rho_0 v^2$$

in agreement with the Newtonian approximation to the flow-field
interaction. Such an approximation also appears most appro-
priate when the transient nature of the event is considered.
Specifically, the impingement of a plane pressure-temperature
discontinuity on a plane wall has been considered experimentally
and analytically by Baganoff [45] for the shock wave reflection
application. On the (μsec) time scale of the reflection event,
it was demonstrated that the process of heat transfer from the
gas will affect the pressure history and inhibit the reflection

event. Extending these concepts to the present case, the thick-
ness of the impinging layer (δ) is then a critical parameter as
the wall (probe surface) could effectively absorb the available
energy; an estimate of the characteristic time for heat transfer
($\tau_{HT} \sim \mu/_\rho a^2$) is of the same order of magnitude as the char-
acteristic fluid mechanical time. On the basis of the above
discussion, the Newtonian approximation will be applied, as

$$P_r = n \ m \ v^2$$

where n is argon number density and v is particle velocity.

The analysis presented above for the evaluation of pres-
sure and density from experimental data are based upon a number
of approximations which can be estimated to produce cumulative
results correct within a factor of two. While not exact, such
results will serve to provide a generally correct indication of
property profiles within the sheet structure.

5.7 SUMMARY OF REDUCED RESULTS

Using the procedures outlined above, profiles of static
pressure and radial pressure were reduced and are presented in
Fig. 5-6 along with current density variation. Current density
and electric field data were reduced following the outlines pre-
sented in the appendices. The profiles of magnetic induction (B)
and force density (j x B) are given in Fig. 5-7 and those of
electric fields (E_z and E_r) in Fig. 5-8. Since they are signif-
icant indicators of the general mode of mass accumulation, the
variation of peak radial pressure and thickness of the dense
accelerated region (II) are given in Fig. 5-9.
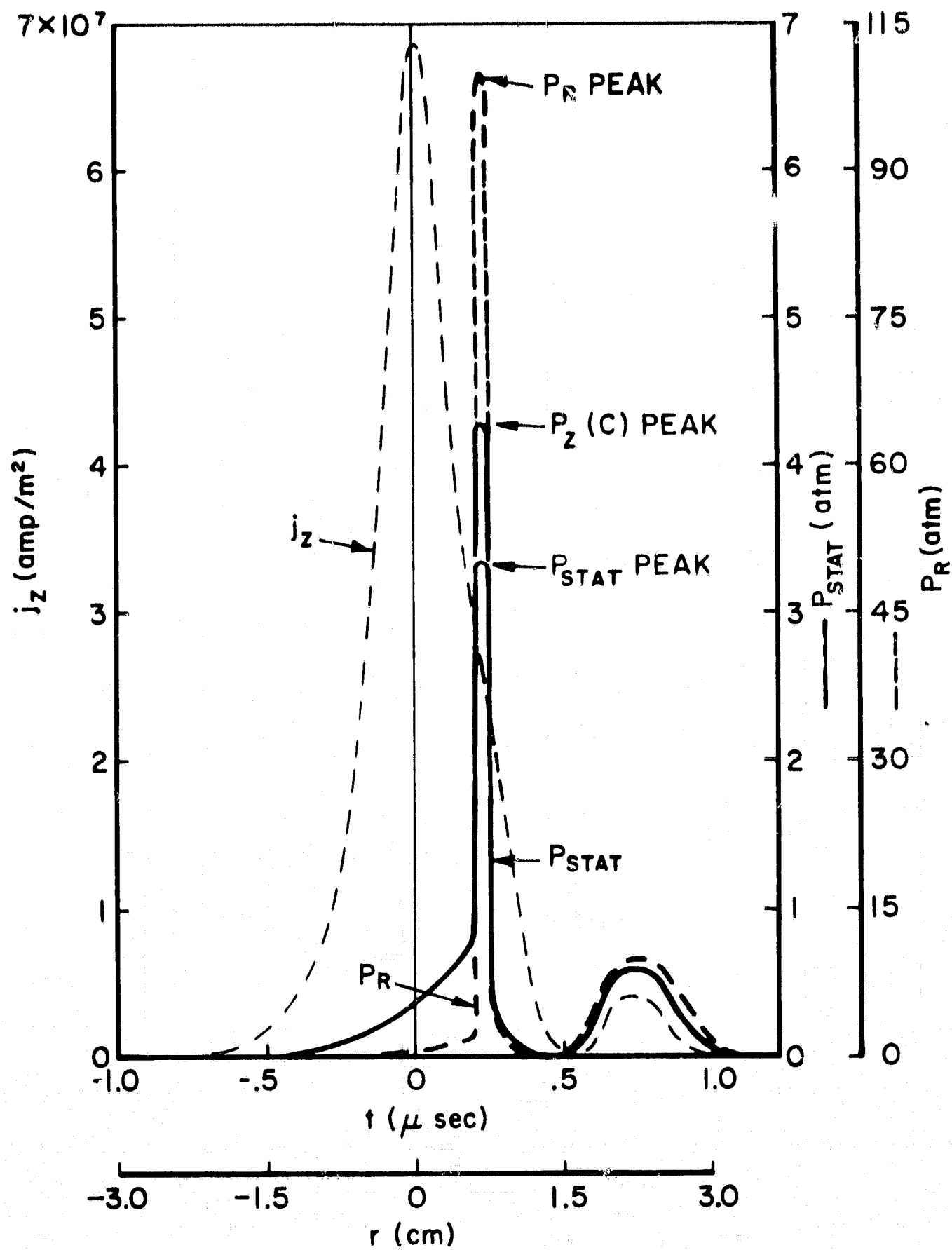
$R = 2''$, $h = 1''$, $t \approx 2\,\mu sec$

CURRENT DENSITY, RADIAL AND AXIAL PRESSURE PROFILES

FIGURE 5-6

CURRENT DENSITY, MAGNETIC INDUCTION, AND FORCE DENSITY
PROFILES

FIGURE 5-7

R = 2", h = 1", t ≈ 2. μ sec

CURRENT DENSITY, RADIAL AND AXIAL ELECTRIC FIELD PROFILES

FIGURE 5-8
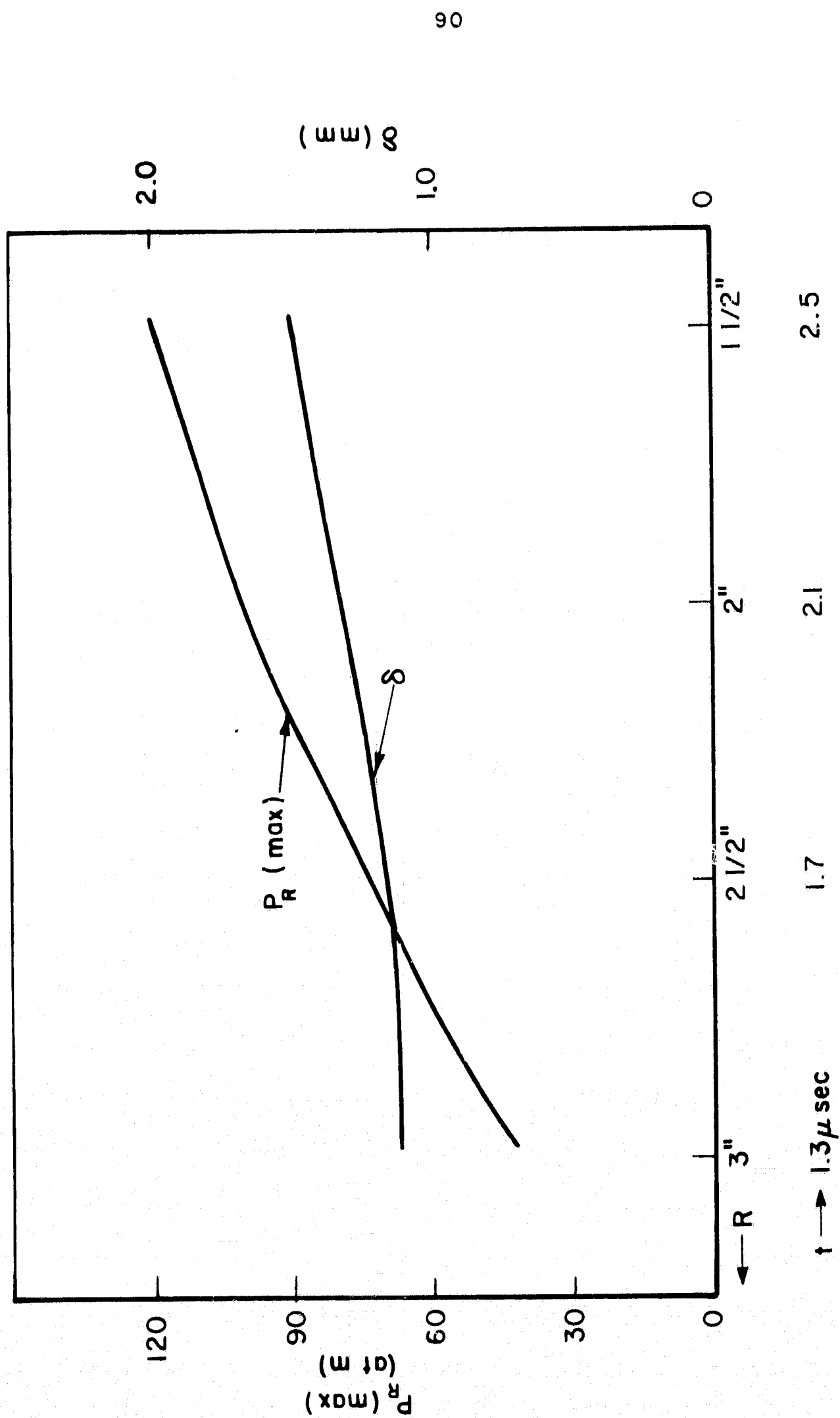
VARIATION OF PEAK RADIAL PRESSURE AND δ WITH RADIUS

FIGURE 5-9

CHAPTER 6

ANALYSIS OF CURRENT SHEET STRUCTURE AND DYNAMICS

6.1 INTRODUCTION

The two most important points to be considered in an analysis of the data that have been presented are the indications of absolute mass entrainment and the development of a compatible sheet model to explain the acceleration process. The establishment of the current carriers within the sheet is basic to any understanding and will be considered first. From the measured electromagnetic field and pressure variation, estimates of particle velocities through the sheet will be made. Further, profiles of number density through the current sheet will be derived and sweeping efficiency estimated. As the question of energy deposition is critical to any acceleration scheme, a general energy balance within the system will be discussed. A momentum balance across the current sheet will be carried out; the experimental force and mass distributions will then be compared with various analytical models that have been proposed.

6.2 CURRENT CONDUCTION PROCESSES

The conduction of current by charged particles is interrelated with the mechanics of particle acceleration, and so it is of importance to establish the species of the dominant current carrier. On the basis of the time resolved spectroscopic

results and collisional excitation noted earlier, an estimation
of the degree of ionization will be made. The time and space
resolved spectroscopy indicated dominant AII(1st ion) radiation
in the forward part of the sheet and significant AIII radiation
in the region of the current density peak; little AI(atom) ra-
diation was observed in any part of the sheet. The estimates
of energy transfer from inelastic electron collision indicated
that the high-energy tail of the electron distribution con-
trolled the ionization process; such a mechanism for argon elec-
tronic excitation would be compatible with the observed spec-
troscopic behavior. On the basis of these results, it is evi-
dent that there are nonuniformities in the ionization profile
through the sheet, however, it appears reasonable for purposes
of analysis to make the approximation that the argon is uni-
formly singly ionized in the forward part of the sheet and
that the degree of ionization remains constant through the
sheet profile.

One model of the conduction process is that of colli-
sionless particles moving under the influence of electric and
magnetic fields; it is accordingly useful to establish the
order of magnitude of some parameters of such motions. Specif-
ically, the radius of gyration of a charged particle in a mag-
netic field,

$$r_B = \frac{m \, v_\perp}{qB} \tag{6-1}$$

where $v_\perp$ is the particle velocity perpendicular to the magnetic

field, B, takes values of $r_B(+) = 10^{-2}$ and $r_B(-) = 10^{-6}$ m in

the region of maximum magnetic field, with $v_\perp = V_s$ for in-

coming particles in the sheet frame. Accordingly, since

the ion gyro radius is of the order of the sheet thickness,

it is indicated that the ion can be accelerated by the mag-

netic field interaction within the sheet. An order of mean

free path for ion collisions of about 0.1 mm in the dense region

indicates that the ions cannot be expected to behave as colli-

sionless particles. It would then appear that the ions are

collisionally coupled once they have entered the entrained re-

gion. For the electrons, in the approximately fully ionized

plasma, electron-ion collisions become dominant ($\lambda_{ei} \approx 0.1$ mm)

and result in randomization of electron motion; this fact along

with the estimated Debye length at 10^{-7} m indicate that the

electrons would not appear collisionless.

In the light of the above considerations, it appears

most appropriate to adopt a continuum treatment to describe the

current conduction process. This approach is embodied in the

generalized Ohm's law [46]:

$$\bar{j} = \sigma_o \left[\bar{E} + \bar{v} \times \bar{B} + \frac{\nabla p_e}{n_e e} - \frac{\bar{j} \times \bar{B}}{n_e e} \right] \qquad (6-2)$$

where $\sigma_o = \dfrac{n_e e^2}{m_e \nu_{ei}}$, $\bar{E}$ is the electric field measured in the

laboratory frame, and $\bar{v}$ is the mass averaged velocity of the

plasma in the laboratory frame. By expressing total current

as the sum of axial and radial components, the following equations can be developed:

$$j_z = \sigma_o \left[E_z - v_r B_\theta + \frac{1}{n_e e} j_r B_\theta \right]$$

$$j_r = \sigma_o \left[E_r + v_z B_\theta - \frac{1}{n_e e} j_z B_\theta + \frac{1}{n_e e} \frac{\partial P_e}{\partial r} \right]$$

where only azimuthal B fields are considered because of axial symmetry and the axial electron pressure gradient is neglected. On the basis of experimental evidence $j_r \ll j_z$ and so in order to carry out some estimates of the conduction process, j_r will be neglected here; further, in region I where the bulk of current is conducted, the electron pressure gradient can be shown to be negligible, thus implying

$$j_z = \sigma_o [E_z - v_r B_\theta] \qquad (6\text{-}3)$$

$$\frac{j_z B_\theta}{n_e e} = E_r + v_z B_\theta \qquad (6\text{-}4)$$

Considering Eq. (6-4), since

$$j_z = n_e e (v_{ze} - v_{zi}) = j_{ze} + j_{zi}$$

and $v_z \approx v_{zi}$, then

$$E_r = \frac{B_\theta}{n_e e} \cdot j_{ze} \qquad (6\text{-}5)$$

Accordingly, it can be seen that there is a direct correlation between radial electric field and electron current. From measured E_r, B_θ and estimated n_e substituted in Eq. (6-5) and com-

pared with j_z, it can be concluded that the bulk of the current (region I) is carried by electrons. This conclusion is reinforced by the simultaneous symmetric axial pressure records and similar radial records for this same region as discussed earlier. The accuracy of radial electric field measurements in the later regions will be affected by gasdynamic interaction [36] and so this analysis will not be applied there. It should also be noted that the radial E_r field, due to charge separation, drops sharply at the exact same time that the radial pressure record begins demonstrating a significant ion concentration (Fig. 5-3). Further, it will be noted that Eq. (6-5) can be used as an indicator of number density in region I, with measured E_r, B_θ, and j_z.

An indication of the current carriers in the dense, entrained region (II) can be derived from the axial pressure records. For this zone, there is a substantial difference between the pressure sensed on the cathode compared to that with an anode mounting (Fig. 5-1). The difference must be accounted for by the axial streaming of heavy particles, that is, substantial currents are conducted by the ions in the dense entrained region. Specifically, the definition that

$$j_{zi}(II) = n_A e \, v_{zi} \qquad (6-6)$$

where n_A is the number density of argon particles, all assumed singly ionized, will be used in a compatible calculation of both number density and axial ion velocity.

The measured current density in the after region (III) is relatively small but with currents in the same direction as the main conduction zone. There is only a slight asymmetry in the axial pressure data which can be accounted for by the flow inclination as evidenced by the luminous wave patterns. Accordingly, it will be assumed that the electrons are the primary current carriers in region III.

Regarding the radial current component, its magnitude was estimated from the appropriate component of Ampere's law, as:

$$j_r = -\frac{1}{\mu_o} \frac{\partial B_\theta}{\partial z} \qquad (6\text{-}7)$$

With appropriate values for R = 2 in., $j_r = 5 \times 10^6$ amp/m^2 as compared to $j_z = 7 \times 10^7$ amp/m^2. These figures indicate the justification for neglecting radial current, but also show agreement with the approximation

$$\frac{j_r}{j_z} \approx \phi \qquad (6\text{-}8)$$

where ϕ is the current sheet tilt from luminosity or magnetic probe records.

6.3 ESTIMATIONS OF PARTICLE VELOCITY

The model that has been developed of the current sheet interaction with the ambient argon atoms is one where the approximately static atom is approached by the imploding current sheet, ionized by electron collision, passes through the current zone with some thermalization of its kinetic energy, meets

a very strong ion collisional interaction in the dense zone
(II) and is entrained at sheet velocity or "leaks" through
the current sheet after having been accelerated to a fraction
of sheet velocity. Clearly, if a particle is entrained it
will be traveling at sheet velocity (V_p), but an estimation
of particle velocities prior to and after this region are
of interest.

The relative energy between a static ion and one en-
trained in the current sheet is 180 ev, as noted earlier. In
zone I an ion overtaken by the current sheet would collide pri-
marily with electrons which would produce little effect on its
trajectory because of the mass discrepancy, however, the colli-
sions with argon particles would randomize an increment of the
incoming ion velocity. With the electrons carrying the cur-
rent, the j x B force is applied to the electrons and trans-
ferred to the ions by the measurable charge-separation radial
electric field. Again, it is desired to establish limiting
profiles of ion velocity and number density on this region.
On this basis, the _minimum_ ion velocity in the current zone
will be calculated as defined by its collisionless motion
through the electric field. By equating particle kinetic
energy with the field energy increment, the ion velocity in
the sheet frame as a function of position in the current sheet
is

$$u_{ri}^2 = v_s^2 - \frac{2}{m_A} \int_0^{r_s} eE_r d_r$$

and since sheet position can be transformed to the time of sheet passage at a fixed position

$$u_{ri}(I) = \left\{ v_s^2 - \frac{2eV_s}{m} \int_0^t E_r dt \right\}^{1/2} \qquad (6-9)$$

From measured profiles of E_r (Fig. 5-8) the lab velocity $v_i = V_s - u_i$ in Fig. 6-1 was derived. The maximum value of $\sim 1/5V_s$ should be noted as conservatively low because of the gasdynamic distortion noted (Appendix B) for radial electric probe measurements and the effects of collisions.

An estimation of particle velocity in region III, behind the intense current zone, can be carried out using Eq. (6-3), where for $n_e \approx 10^{16}/cm^3$ and $T_e \approx 3$ ev, $\sigma_o \approx 10^4$ mho/m and so $j_z/\sigma_o \approx 10^2$ v/m which can be neglected compared with the magnitude of the remaining terms. Rearranging, the particle velocity then becomes

$$v_{ri}(III) \approx \frac{E_z}{B_\theta} \qquad (6-10)$$

and from the field profiles (Figs. 5-7 and 5-8) the variation presented in Fig. 6-1 is implied.

6.4 NUMBER DENSITY PROFILE AND SWEEPING EFFICIENCY

The derivation of profiles of particle number density compatible with the profiles of pressure, electric and magnetic fields, is desired. As in the earlier treatments it is most
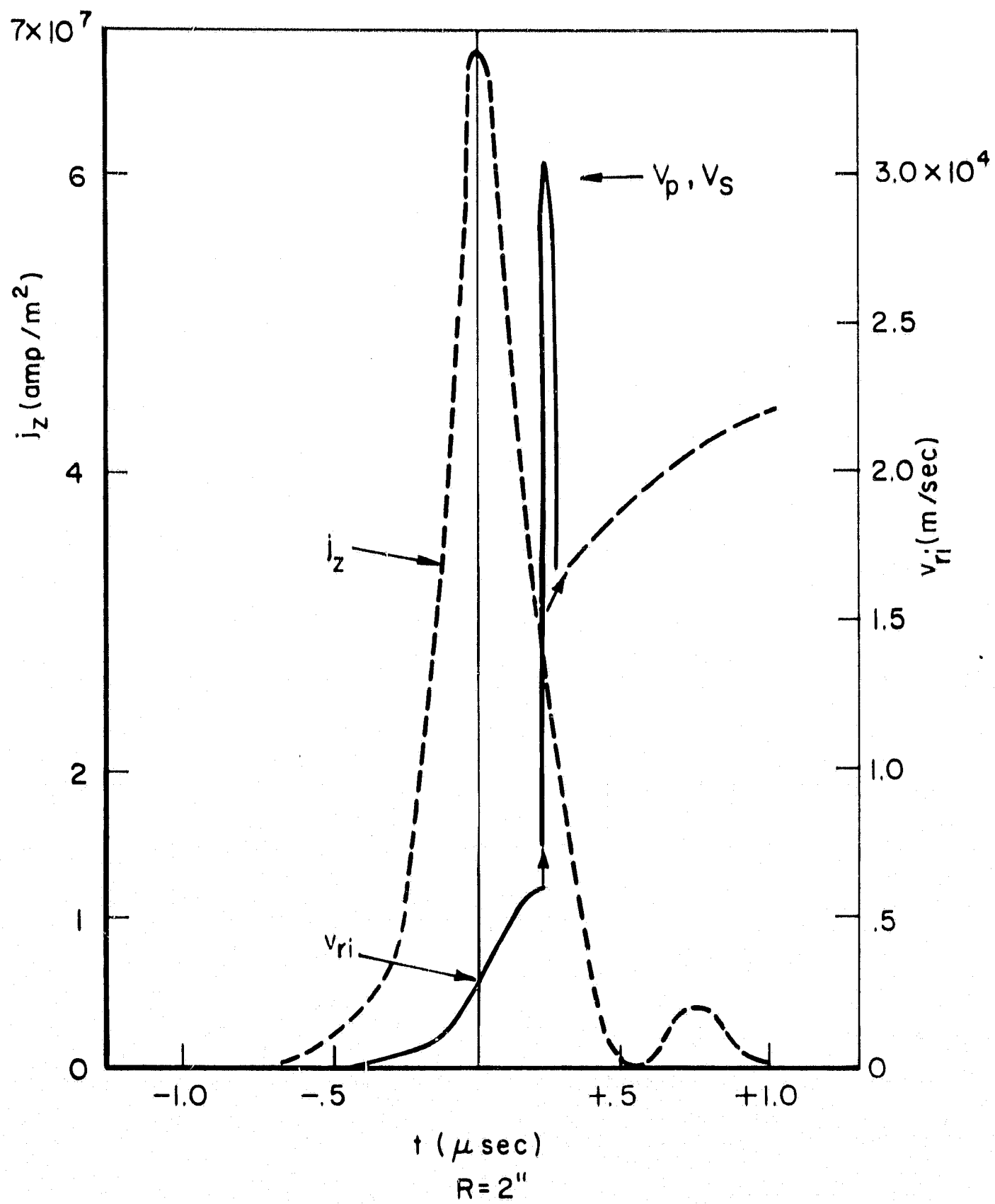
ESTIMATED RADIAL ION VELOCITY AND CURRENT DENSITY PROFILES

FIGURE 6-1

convenient to discuss the distinct zones of the sheet separately.

Region I

The leading edge of the current sheet has been identified as one with intense electron current conduction. Further, the simultaneous drop in E_r (Fig. 5-1) and rise in P_r (Fig. 5-3) at the instant of $\dot{B}_\theta$ peak both indicate the arrival of significant numbers of ions with the related increase in number density. The increment of radial pressure between $\dot{B}_\theta$ peak and the major pressure discontinuity does not appear on the axial pressure records, leading to the identification of this increment with a directed motion of ions. Experimentally then, this initial zone (I) appears as a primary region of isotropic pressure and a secondary region with small but definable increment of impact pressure that can be used to indicate number density. Since the isotropic pressure can be attributed to either density or temperature effects, it appears necessary to evaluate a more general density profile. This evaluation can be carried out by appealing to the apparent absence of mass accumulation and resulting steady flow of particles through the zone. Taking a frame of reference fixed with the sheet, to good approximation:

$$\text{(Zone I)} \quad n_o V_s = nu \quad\quad\quad (6\text{-}11)$$

where n_o is ambient number density, n is ion number density through the zone as a function of particle velocity, $u \equiv V_s - v_r$. Taking the variation of v_r presented in Fig. 6-1, the number

density profile indicated in Fig. 6-2 was derived. Since the
particle velocities were derived from a radial E field integral
(collisionless), the region of questionable accuracy is shown
dashed. However, it is to this subregion that the radial pres-
sure increment can be applied, with the following formulation

$$\Delta P_r = n_A m_A v_r^2$$

where v_r is the local field-induced ion velocity. It can be
seen that there is reasonable agreement between the two sets of
data when they overlap. It will again be noted that the derived
results represent a minimum velocity profile and a maximum num-
ber density profile according to the model. As a further check
on the indicated profiles, number density was calculated from
Eq. (6-5) and was found to be in reasonable agreement when the
experimental error in E_r was considered.

Region II

The number density in the entrained region will not be
treated as a distribution but as an average due to the inade-
quate resolution of the measurements within the estimated 1.5 mm
thick zone. Because of the large pressure discontinuity on both
the radial and axial records, it must be expected that the dis-
tribution is actually sharply peaked at the leading edge of the
region; the implications of this effect will be discussed later.
The derivation of number density from radial pressure measure-
ments will first be presented, and then the relationship of axial
measurements to axial ion velocity will be outlined.
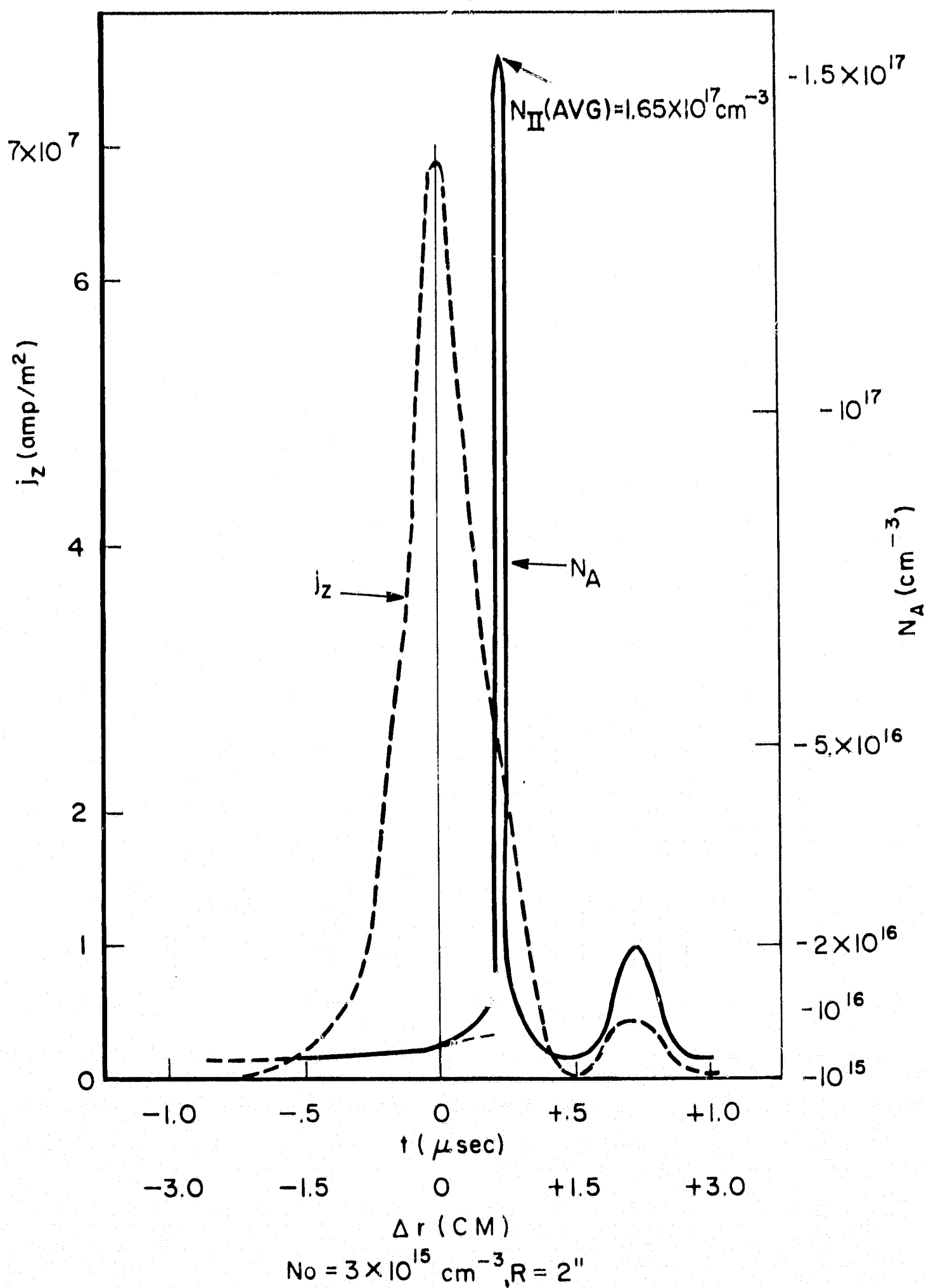
ESTIMATED NUMBER DENSITY AND CURRENT DENSITY PROFILES

FIGURE 6-2

The reduction of an average density from radial pressure measurements is carried out from an impact analysis,

$$P_r = n_A m_A v_r^2$$

where v_r for the entrained mass is equal to sheet (V_p) velocity. Taking the appropriate value for R = 2 in. of P_r = 100 atm, the indicated average number density is $n_A(II) = 1.65 \times 10^{17}/cm^3$, (Fig. 6-2).

As has been noted earlier, the difference between the static response, P_{stat}, and $P_Z(C)$ can be related to the ion number density and axial velocity. Again equating pressure increment to impact momentum transfer,

$$\Delta P_Z = n_A m_A v_{zi}^2$$

where, when appropriate values are substituted (ΔP_Z = 1 atm) then $v_{zi} = 3 \times 10^3$ m/sec is indicated. This value compares favorably with the tilt component of axial velocity, $V\sin\phi = 2.7 \times 10^3$ m/sec. A further check on the magnitude of the axial velocity can be carried out on the basis of an axial momentum balance,

$$f_z = \rho \frac{D}{Dt} v_z$$

and if the force field to the leading edge of region II is considered, steady flow conditions can be applied to give

$$j_r B_\theta = n_o m_A V_s \frac{\partial v_z}{\partial r}$$

Recalling that $j_r \approx \phi j_z$, then

$$dv_z = \frac{\phi j_z B_\theta}{n_o m_A V_s} dr$$

and across the region of interest $r \approx$ constant, so from Ampere's law,

$$\int_I dv_z = \int_I \frac{\phi B_\theta dB_\theta}{\mu_o n_o m_A V_s}$$

then at the leading edge of Zone II

$$v_z \approx \frac{\phi B_\theta^2}{2\mu_o n_o m_A V_s} = 2.8 \times 10^3 \text{ m/sec}$$

in reasonable agreement with the results derived from pressure measurements.

The above value of axial ion velocity can be related to current density through Eq. (6-6), as

$$j_{zi} = n_A e v_{zi} \approx 8 \times 10^7 \text{ amp/m}^2$$

compared with the total current density, $j_z = 2.5 \times 10^7$ amp/m^2, it is apparent that negative electron currents are flowing, with axial velocity $v_{ze} \approx 2 \times 10^3$ m/sec. It would appear that the negative electron current is due to collisional coupling of the electrons with streaming ions in the dense, entrained region.

Region III

The gas that has been passed over by the intense current

sheet appears to have a significant induced velocity as evidenced by the axial electric field. Using the particle velocities indicated in Fig. 6-1, the number densities in this region were estimated using the radial probe data, with

$$P_r = n_A m_A v_r^2$$

The indication of number density from the axial probe measurement and the estimated temperature are in reasonable agreement with the impact profiles.

Mass Entrainment

The analysis presented to this point serves to identify the reservoir of entrained mass as contained within region II, since the primary region (I) appears to support steady flow, and since the swept region (III) is evidently not directly coupled to the intense acceleration zone. A calculation of entrained mass, then, is effectively a calculation of the mass in region II. Analytically, it is appropriate to define the ratio of mass entrained in the current sheet layer (II), to that originally in the annular swept volume as the sweeping ratio

$$S \equiv \frac{n_{ent} \cdot m_A (2\Pi R \cdot \delta) \cdot h}{n_o \cdot m_A \cdot \Pi (R_o^2 - R^2) \cdot h}$$

Accordingly, the density in region II can be expressed as

$$n_{II} = n_o + \frac{n_o (R_o^2 - R^2) S}{2R \cdot \delta}$$

as a function of radius and δ ; or, with measured values of n_{II}.

$$S = \left(\frac{n_{II}}{n_o} - 1\right) \frac{2R \cdot \delta}{(R_o{}^2 - R^2)}$$

The variation of measured values of n_{II} and δ with radius, and the derived variation of S is presented in Fig. 6-3.

6.5 ESTIMATED TEMPERATURE PROFILE AND ENERGY BALANCE

From the measured static pressure profile and the number density variation reduced from radial pressure records, it is possible to estimate particle temperatures from the equation of state, $p = nkT$. Since it has been assumed that $n_i = n_e$, a calculation of total particle temperature $T_t \equiv T_a + T_e$ can be carried out directly. Species temperatures can be distinguished by estimation of electron temperatures in the various regions as proposed above. On this basis, the estimated temperature profiles are presented in Fig. 6-4. These results are meant to serve only as general indications of thermal energy deposition and not as exact profiles. Specifically, it should be noted that it is only possible to consider average values for region II because accurate resolution of details is impossible. However, the data do appear to indicate that this is not a region of constant pressure, density, and temperature, but is sharply peaked at its leading edge in all these variables. This effect could help to explain the estimated 34 ev ion temperatures at the leading edge and the average of 12.5 ev for the zone. A
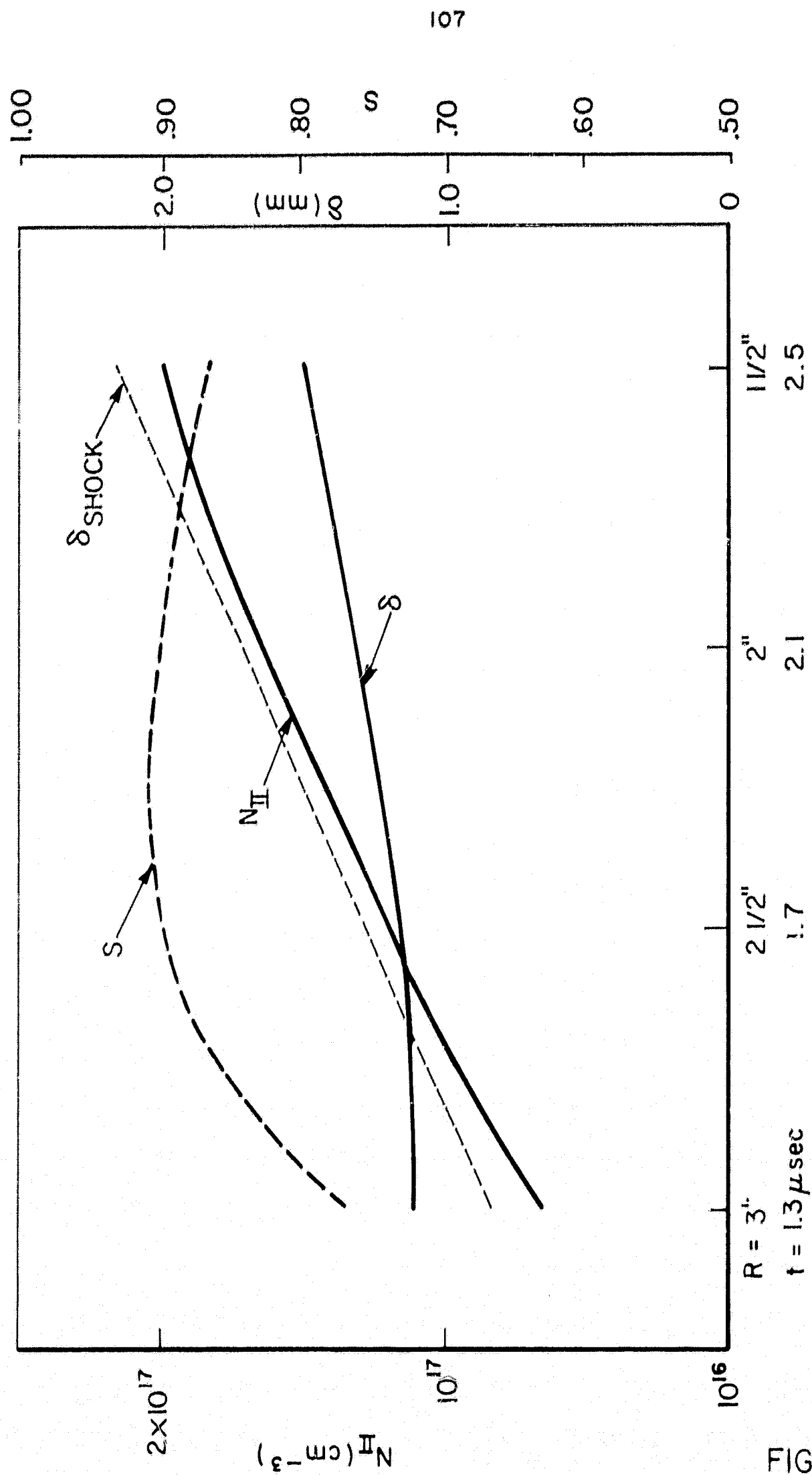
RADIAL VARIATION OF PEAK DENSITY, WIDTH OF ENTRAINED ZONE, AND SWEEPING EFFICIENCY

FIGURE 6-3
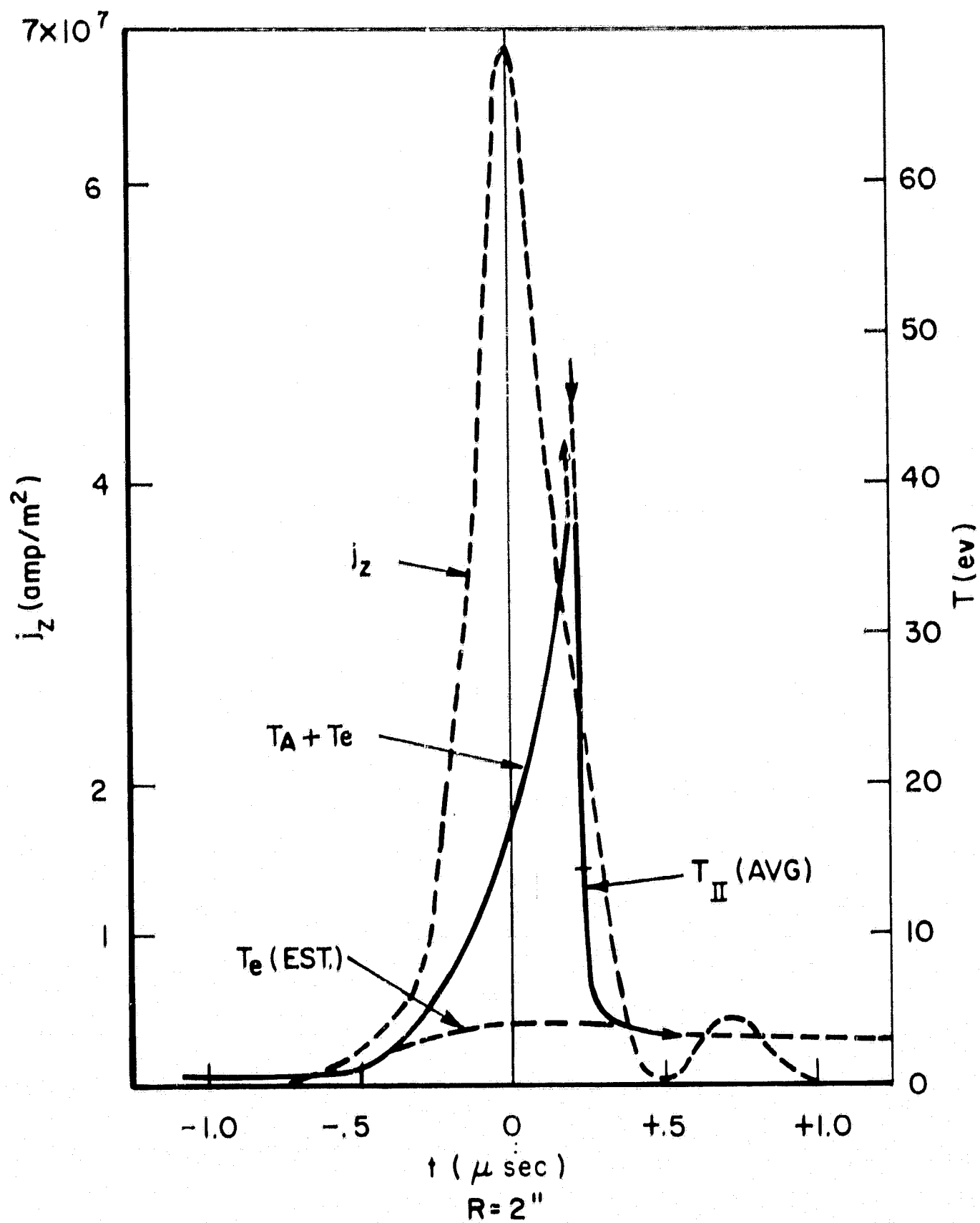
ESTIMATED TEMPERATURE AND CURRENT DENSITY
PROFILES

FIGURE 6-4

sharply peaked profile could still exhibit a temperature jump at the leading edge to be compatible with the pressure and density discontinuity and yet satisfy the temperature estimates presented.

With an estimate of particle temperatures through the current sheet, it is now possible to carry out a general energy balance within the discharge system in an attempt to corroborate the sheet behavior postulated and to clarify further the sheet interaction mechanics. Calculations of energy components will be carried out for the R = 2 in. sheet position.

The total energy input to the discharge chamber can be estimated from measurements of voltage drop across the electrodes (V_{ch}) and circuit current (I), as

$$E_{ch} = \int_{0}^{t} I \cdot V_{ch} \, dt \approx 400 \text{ joules}$$

where t is the time required for the sheet to reach radius R. The energy deposited in the magnetic field system behind the sheet can be expressed as

$$E_{B} = \int_{0}^{R} \frac{B^2}{2\mu_o} (2\Pi rh) \, dr \approx 200 \text{ joules}$$

The kinetic energy of the particles accelerated by the current sheet is

$$E_{kin} = 1/2 \, n_o s m_A V_s^2 \cdot \Pi(R_o^2 - R^2) \cdot h \approx 100 \text{ joules}$$

Accordingly, the thermal energy increment can be evaluated as

$$E_{TH} = E_{ch} - (E_B + E_{kin}) \approx 100 \text{ joules}$$

in agreement with the equipartition of sheet energy between kinetic and thermal components expected for the constant velocity trajectory [12]. When the 100 joule energy increment is averaged over the available atoms the value of 180 ev per particle is arrived at, in agreement with the thermal component calculated from ion kinetic energy in the sheet frame; it is much more appropriate to examine the component parts of the thermal energy deposited within the sheet.

As a first step, the kinetic energy of axial streaming will be evaluated as

$$E_{kin}(z) = 1/2 \ m_A n_{II} v_{zi}^2 \cdot 2\Pi R \cdot \delta \cdot h \approx 1 \text{ joule}$$

a negligibly small component, accordingly, in the sheet frame

$$E_{TH} \approx E_{int} = E_T + E_{el} + E_{ion} + E_\nu$$

where the so-called internal energy is broken into translational (temperature), ionization, electronic excitation and radiated energies. Now the translational and ionization energies can be calculated separately using the estimated temperature profile (Fig. 6-4) and the assumption of complete single ionization:

$$E_T = \sum n \cdot 3/2 \ k(T_A + T_e) \cdot vol. \approx 15 \text{ joules}$$

$$E_{ion}(1st) = e_i \cdot n_o \cdot \Pi(R_o^2 - R^2) \cdot h \approx 10 \text{ joules}$$

with e_i = 15.75 ev. The energy deposited within the electronic
excitation mode has not yet been considered; i.e., if this term
was neglected there would exist complete nonequilibrium between
the electronic states and the translational states. For the
other limiting case, assuming complete equilibrium between the
translational and electronic modes as would be expected because
of electron activity, the internal energy can be estimated from
the work of Knoche [47,48] who considered the thermodynamic
properties of argon plasma to temperatures exceeding 10^5 $^\circ$K.
This work assumes complete thermal equilibrium, including equal
electron and ion temperatures, resulting in dominant sixth and
seventh stage ions at 10^5 $^\circ$K. In order to estimate the elec-
tronic energy investment in the present case with dominant first
and second stage ions, the appropriate internal energy for that
condition was estimated as

$$E_{el} \approx 15 \text{ joules}$$

The thermal energy balance must be completed, then, by a term
to account for energy loss by radiation. The components can be
tabulated and summed to complete the energy balance, as:

$$E_{kin}(z) \quad \approx \quad 1 \text{ joule}$$

$$E_T \quad \approx \quad 15 \text{ joules}$$

$$E_{ion}(1st) \quad \approx \quad 10 \text{ joules}$$

$$E_{el} \quad \approx \quad 15 \text{ joules}$$

$$E_\nu \quad \approx \quad 60 \text{ joules}$$

$$\sum E = E_{TH} \quad \approx \quad 100 \text{ joules}$$

The radiated energy component can be used to define an effective "brightness" temperature, T_{ν}, as

$$E = \int_0^t 2 \cdot 2 \pi R \cdot h \cdot \sigma_r T_{\nu}^4 \, dt$$

where with $E_{\nu} = 60$ joules, $kT_{\nu} = 1.2$ ev indicating an optically thin body of gas. The significant percentage (60%) of thermal energy lost in radiation agrees with the experimental observation of intense light emission from the sweeping discharge.

6.6 ACCELERATION MECHANICS

The analysis of the current sheet presented above has established the distribution of mass and the distribution of energy within the current sheet. The analysis of acceleration mechanics is basically concerned with the establishment of a radial momentum balance within the sheet system. Accordingly, a differential formulation of momentum conservation will first be presented and the application of this relationship to the current sheet will then be carried out.

The radial momentum balance, neglecting boundary effects, can be written most generally (per unit volume) as

$$f_r = \rho \, \frac{D v_r}{Dt}$$

or

$$f_{em} - \frac{\partial p}{\partial r} = \frac{\partial (\rho v_r)}{\partial t} + \frac{\partial}{\partial r} (\rho v_r^2)$$

where f_{em} is the electromagnetic force applied to the streaming

particles. This expression will be applied in a frame of reference fixed with the current sheet. It has been established that the electrons are the primary current carriers in the sheet and accordingly, that the j x B momentum increment received by the electrons is transmitted to the ions through the radial electric field. Since the radial E field drops rapidly toward zero at the time of $\dot{B}_\theta$ peak, it can be presumed that the local j x B increment is applied directly to the heavy particles without measurable charge separation after that point. Accordingly, for a momentum balance between the sheet leading edge (R_1) and a point later than $\dot{B}_\theta$ peak (R_2)

$$-\int_{R_1}^{R_2} j_z B_\theta dr - \int_{R_1}^{R_2} \frac{\partial p}{\partial r} dr = \int_{R_1}^{R_2} \frac{\partial \rho}{\partial t} \cdot v_r dr + \int_{R_1}^{R_2} \frac{\partial (\rho v_r^2)}{\partial r} dr$$

since

$$\frac{\partial}{\partial t}(\rho v_r) \approx v_r \frac{\partial \rho}{\partial t}$$

Further, in the sheet frame, $v_r = 0$ for the region of entrained mass ($\partial \rho/\partial t \neq 0$), and taking ambient properties (o) as initial conditions ($p_o \approx 0$, $v_{ro} = V_s$), then

$$\int_{R_1}^{R_2} j_z B_\theta dr + p_2 + \rho_2 v_{r_2}^2 - \rho_o V_s^2 = 0$$

Now the experimentally derived profile of entrained mass has indicated mass concentrations within a thin, discontinuous region, accordingly, it appears most appropriate to apply the

above relationship between ambient conditions and an interface
defined slightly behind region II, where in the near vacuum,
$p_2 \approx 0$, then

$$\int_{R_1}^{R_2} j_z B_\theta dr = \rho_o V_s^2 - \rho_{III} v_{rIII}^2$$

This expression can be further reduced by applying the expression
of mass conservation, as

$$\frac{\partial \rho}{\partial t} + \frac{\partial}{\partial r}(\rho v_r) = 0$$

which, when integrated between the points of interest gives

$$\rho_{III} v_{rIII} = \rho_o V_s - \frac{\partial \rho_{III}}{\partial t} \cdot \delta = \rho_o V_s (1 - s)$$

Substituting into the momentum balance

$$P_{jB} \equiv \int_{R_1}^{R_2} j_z B_\theta dr \approx \rho_o V_s^2 s$$

where S is the sweeping efficiency defined earlier, and P_{jB}
is the effective pressure acting on the entrained mass due to
the j x B force field. Taking experimental values,
$P_{jB} = 3.36 \times 10^5$ n/m^2, implying a sweeping efficiency of
S $\approx$ 1.8, in obvious contradiction with measured S $\approx$ 0.9 and
a limiting value of S'(max) = 1. The above calculation must
be interpreted from the point of view that the equation does
not describe a complete momentum balance. Specifically, a
momentum increment due to the boundary layer effects at the

electrodes can be expected, which within the general orders
of magnitude of the problem could account for the excessive
momentum increment. It will also be noted that there is
apparent agreement between effective driving pressure and the
average static pressure of the entrained mass, i.e., $P_{jB} \approx P_{stat}$.

It would appear, then, that the current sheet interacts
with the ambient gas as a slightly porous piston. In the con-
text of that observation, it is of interest to consider the
state of the gas left behind (III) by the intense current sheet
interaction. Following region II, there is an evident low pres-
sure region followed by a gradual continuous compression and a
second expansion. For purposes of analysis, this behavior will
be compared with that predicted for gas behind a real, physical
piston. For such a case, the important parameter for the gas
behind the piston is the characteristic velocity, U_L. A piston
moving with a velocity greater than U_L will be followed by a
region of vacuum and then a continuous compression. The char-
acteristic velocity can be evaluated as

$$U_L = \frac{2a_o}{\gamma - 1}$$

Taking approximate values of $\gamma \approx 1.3$ and $a_o \approx 4 \times 10^3$ m/sec
for $T \approx 3$ ev [42], then $U_L \approx 3 \times 10^4$ m/sec -- very near sheet
velocity, indicating that this effect could significantly in-
fluence the swept gas. Accordingly, the behavior of the un-
swept gas is in general agreement with the concept of the cur-
rent sheet acting upon the ambient gas as a porous piston.

6.7 DISCUSSION OF ANALYTICAL MODELS

The analysis of the current sheet that has been carried out has been based exclusively on the compatible interpretation of simultaneous experimental profiles through the sheet. It is now of interest to consider the profiles that have been derived within the structure and to compare them with those predicted by more general analytical models that have been proposed.

Snowplow Model

The snowplow model provides perhaps the simplest model for dynamic current sheet interaction. It is based on the assumption of an infinitely conducting body of plasma, through which the current must flow through a thin surface layer. This surface current layer is presumed to act as an impermeable "magnetic piston" that entrains the swept mass in a very thin layer on the surface and carries it along. The model, then, predicts an infinitesimally thin current sheet with no magnetic field in front and no mass in the rear; across that interface the gas kinetic pressure, P, will equal the magnetic pressure, P_{mag}, as

$$P = \int_{R_1}^{R_2} j_z B_\theta \, dr = \frac{B^2 (R_2)}{2\mu_o} = P_{mag}$$

Accordingly, it can be seen that such a model would not provide an exact analysis for the present experiments for several reasons. First, the current sheet is not infinitesimally thin, but has a finite width ($\sim$ 2 cm) with mass concentration

(~ 2 mm) in the rear of the force field. Since there is no definable interface where there is a balance between gas kinetic and magnetic pressure, there are conceptual difficulties in defining the snowplowing surface. Further, the basic model does not consider leakage, however, such effects can be included in a straightforward manner. It should be noted that while this model is not exact, it does agree approximately with a correct momentum balance outlined above, applied as jump conditions across the current conduction region.

Shock Wave Models

When the specification of finite compressibility of the gas is introduced into a piston-sweeping model, it can be expected that a shock wave will emerge from the interaction. Accordingly, the experimental results will be compared with the predictions of such a model. It should be noted that it is well established that shock waves can be generated in 100 μ ambient argon [49], however, the conditions required for classical shock formation in electromagnetic shock tubes are not clearly understood [50]. The present experimental results define a density discontinuity imbedded in the current sheet, with no measurable change in the magnetic field corresponding to the density variation. Accordingly, since analysis of MHD shocks invariably predicts a change in magnetic fields across such a density discontinuity [51], the experimental results will be compared with classical gasdynamic shocks as a valid approximation. However, it will again be emphasized that there is no clear delineation

between piston and shock in the present experiments, in fact, the shock is imbedded in the rear of the force field.

Detailed calculations of the flow field produced by a pressure discontinuity in a cylindrical shock tube have been presented in the literature [52,53], however, the results do not clearly define the behavior of an effective piston and so application to the present case is not straightforward. However, the conditions of the present experiment can be directly compared with the results of a **self-similar** solution of the multidimensional piston problem presented by Chernyi [35]. The analysis presented is based on a Lagrangian formulation and expansion of gas properties in terms of the strong shock density ratio. When that solution is adapted to the cylindrical imploding geometry with a constant velocity piston, a constant velocity shock with constant pressure and density behind the shock are predicted. The theoretical separation of piston and shock (δ shock) predicted by this analysis is presented in Fig. 6-3 for purposes of comparison. This solution, then, predicts a constant post-shock pressure with linearly increasing shock separation (δ shock). This behavior is in direct conflict with the present experimental evidence, where it is observed that the region of entrained mass is approximately constant thickness while its density significantly increases with implosion. From this comparison, it is evident that the sweeping current sheet, although acting to entrain a very high percentage of mass encountered, does not interact in detail as a classical piston during the discharge initiation period observed.

Compatible analytical models for the cylindrical electromagnetic discharge have been presented by Greifinger and Cole [54] for the infinite conductivity case, and Hoffman [9] for specialized finite conductivity cases. Both solutions are based upon the application of similarity techniques to the complete equations. However, the infinite conductivity assumption with the implicit infinitesimally thin sheet does not accurately describe the experimental configuration of a diffuse current sheet providing a distributed force field. The finite conductivity calculations [9] include predictions of number density profiles for perfectly sweeping sheets; the theoretical solution for parameters appropriate to the present experimental results show reasonable agreement up to the pressure discontinuity, which is a singular point. On the basis of this theoretical study and related experimental studies, it was concluded that shocks would not form in the forward portion of the current sheet in argon. The trends evident in the present experimental study do indicate an approach toward an entrained gas region of constant density and increasing thickness (δ) as the sheet implodes, but any prediction of eventual shock wave separation from the current sheet does not appear to be warranted. Regarding the significance of the present results to a purely analytic treatment, there are clear indicators of conductivity profile and boundary conditions within the sheet, both of which are critical elements in the development of any similarity solution.

CHAPTER 7

SUMMARY

The interaction of a dynamic current sheet propagating into ambient argon has been examined experimentally in a linear z-pinch device and the results were incorporated into a compatible sheet interaction model. Some specific aspects of the study are as follows.

Measurement of pressure profiles through the current sheet required the development of a high-speed piezoelectric pressure transducer. This study resulted in the determination of a new criterion for matching the piezo material to the probe body and the utilization of a unique high voltage insulation.

The examination of probe-discharge interaction resulted in the discovery of luminous profiles about the probe in the swept gas region and their tentative identification as shock waves resulting from a sheet induced flow.

Simultaneous measurements of pressure, current density, and electric field served to identify three regions of dominant behavior within the current sheet; in sequence, regions of current flow (I), mass accumulation (II), and induced flow of unswept gas (III) were defined. The primary current carriers were found to be the electrons; however, significant axial

streaming of ions was identified in the rear of the sheet (II),
corresponding to ion current conduction.

Profiles of particle density, temperature, and velocity
through the sheet were derived from the data. With these re-
sults the current sheet was seen to entrain a large percentage
of the mass it encountered; a momentum balance established the
existence of a substantial loss mechanism, such as electrode
drag; an energy balance was in agreement with temperature and
ionization models and defined a significant radiation loss.

The momentum balance across the current sheet was found
to agree in concept, but not in detail, with a snowplow formu-
lation. Experimentally derived variation of pressure, density,
and width of the entrained gas zone during the initial discharge
period observed did not agree with separated piston-shock wave
models of current sheet interaction. The significance of the
experimental results to a general theoretical analysis of cur-
rent sheet interaction was concluded to be the definition of
the dominant mechanisms for each of the regions within the
sheet structure.

APPENDIX A

MAGNETIC PROBE TECHNIQUES

A.1 INTRODUCTION

A knowledge of magnetic field distribution profiles is an important element in the analysis of any electromagnetic event. The determination of these profiles for a transient, self-field discharge can be carried out with simple inductive loops. The performance of such devices has been well-documented in the literature [17], and so the present outline will be directly concerned with basic performance, perturbations of probe output, and evaluation of current density from the basic magnetic field data.

A.2 BASIC PERFORMANCE OF THE INDUCTIVE LOOP

An inductive loop is simply a length of conducting wire turned to form a closed contour with twisted leads. The relationship between voltage output and magnetic induction is provided by Faraday's law,

$$\nabla \times \overline{E} = -\frac{\partial \overline{B}}{\partial t}$$

which when integrated over the loop area indicates a voltage

$$V_B \text{ (emf)} = -\int_A \frac{\partial \overline{B}}{\partial t} \cdot d\overline{A}$$

$$\approx A \cdot \frac{\partial B}{\partial t} \text{ for B constant, normal to A}$$

The magnetic induction can be most easily determined by in-
tegrating the above signal in a passive RC network with ter-
minating resistance R_o, integrator resistance R, and inte-
grator capacitance C, resulting in a signal voltage

$$V_B \text{ (emf)} = \frac{1}{RC} \int V_{\dot{B}} \, dt$$

$$\approx \frac{A}{RC} \cdot B \text{ for a single-turn coil}$$

On the basis of providing satisfactory spatial resolution
with the 5/32-in. diameter pressure probe, all magnetic probes
were fabricated with either two or three turns of #27 Formvar-
coated copper wire and wrapped with a 3/32-in. (2.4 mm) in-
ternal diameter. Several inches of twisted lead connected the
coil to 50-Ω cable for transmission to the oscilloscope. The
primary constraint on the probe system is related to frequency
response, defined in terms of $\tau = L/R_o$, the time it takes a
suddenly applied field to enter the coil. Taking approximate
values for the above circuit, $\tau = 10^{-10}$ sec, well within the
time scale of the current sheet event. In order that the error
introduced by the integrator would be small [17], the constraint
τ_e (experiment) << RC = 200 μsec was satisfied.

Probe coils were calibrated by discharging several
lumped capacitors through a shorting post in the discharge cham-
ber; the output was compared with the magnetic fields calculated
from known currents and radial position.

A.3 PERTURBATIONS OF MAGNETIC PROBE OUTPUT

As with any probe technique which requires immersion of the sensing element within a moving plasma, the magnetic probe signal is subject to distortion. Effects such as thermal heating of the probe covering, ablation and its consequences, distortion of current patterns have been discussed generally by Lovberg [17] and specifically for the present application by Burton and Ellis [13,14]. Ideal magnetic diffusion times were calculated to be well within acceptable limits; however, the effects of plasma diffusion in the environment of a gasdynamic interaction with the probe structure are of some concern. Simultaneous measurements of $\dot{B}_\theta$ and pressure are intended, and any delay in $\dot{B}_\theta$ due to diffusion would be unsatisfactory. In order to evaluate this effect, a series of shots was taken in the pinch chamber, varying the thickness and type of insulating covering over the magnetic probe while maintaining every other parameter constant. A highly reproducible current sheet was developed for this purpose by altering the circuit current waveform; the results of this study are presented in Fig. A-1. It can be seen that there is a significant reduction in the magnitude of $\dot{B}_\theta$ peak with the heavier insulation. Further, there also appears to be a noticeable broadening effect in the $\dot{B}_\theta$ profile with covering thickness; this implies that for detailed sheet studies, a magnetic probe coil should be given only thin coverings of insulation. Accordingly, the magnetic probe coils built into

T-1636

I

$\dot{B}_\theta$

FORMVAR INSULATION

|←1 μsec

T-1638

$\dot{B}_\theta$

0.5 mm DUCO COVERING
OVER FORMVAR —
LOOP OPEN

T-1640

$\dot{B}_\theta$

1mm DUCO COVERING
OVER FORMVAR—
DUCO FILLED LOOP

T-1647

$\dot{B}_\theta$

5mm DIA PYREX TUBE
OVER FORMVAR
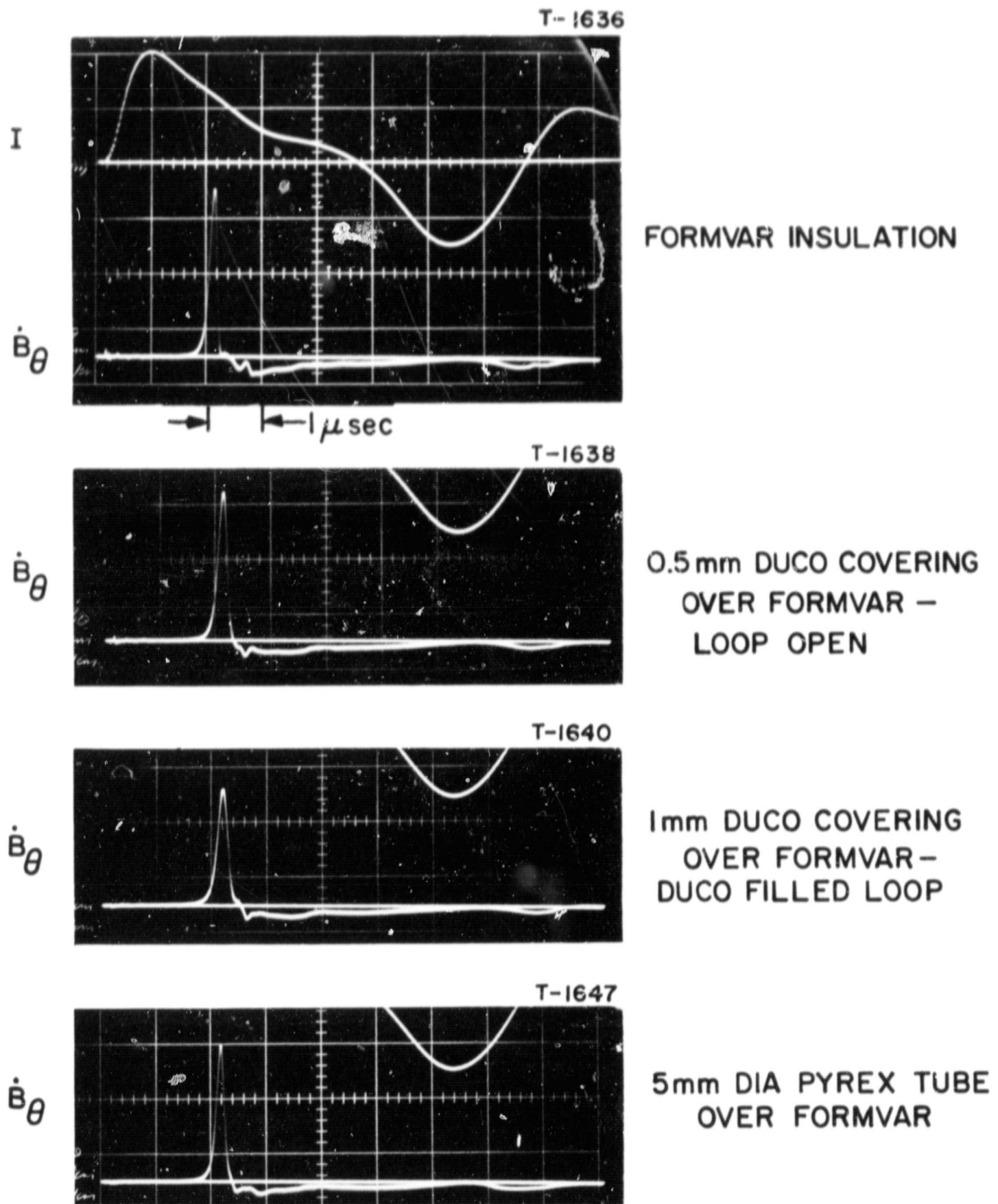
RESPONSE OF MAGNETIC PROBE WITH VARIOUS
INSULATOR COVERINGS

FIGURE A-1

the pressure probe structure were insulated only by heavy Formvar and a very thin covering of epoxy. For the general chamber survey, a coil encased in a 5 mm diameter Pyrex tube was employed.

A.4   CURRENT DENSITY DISTRIBUTION

The output from an induction coil can be related to current density through Ampere's law, neglecting displacement current,

$$\mu_o \overline{j} = \nabla \times \overline{B} \qquad (A-1)$$

or in its appropriate form for the cylindrical geometry,

$$j_z(r,t) = \frac{1}{\mu_o r} \frac{\partial}{\partial r} (rB_\theta) \qquad (A-2)$$

The above equation can be integrated over a surface in the r — θ plane to give

$$\mu_o I_{enc}(r,t) = 2\pi r \, B_\theta(r,t) \qquad A-3)$$

which when substituted into (A-2) provides

$$j_z(r,t) = \frac{1}{2\pi r} \frac{\partial}{\partial r} (I_{enc}) \qquad (A-4)$$

Following Ellis [14], (A-3) will be differentiated with respect to time, and the enclosed current variation at a fixed radius will be expressed as

$$\dot{I} = \dot{I}_{circuit} + \dot{I}_{convection}$$

$$\approx \dot{I}_{Rog} \cdot \frac{I_{enc}}{I_{Rog}} - v_s \frac{\partial I_{enc}}{\partial r}$$

which when combined and substituted into (A-4) for $\partial/\partial r$ (I_{enc}) gives

$$j_z(r,t) = \frac{1}{u_o V_s} \left[\dot{B}_\theta - \left(\frac{\dot{I}_{Rog}}{I_{Rog}} \right) B_\theta \right] \qquad (A-5)$$

where V_s is current sheet velocity, and the subscript Rog refers to Rogowski coil (total circuit current) data. The current density profiles evaluated by the above technique were checked for accuracy by comparison with enclosed current profiles; the enclosed current calculated from a time integration of current density, compared with a more direct calculation from Eq. (A-3) were generally found to be in agreement. The distribution of chamber current for the given waveform was found to result in approximately 75 percent of the current flowing within the sheet, with the remainder distributed in the swept area.

APPENDIX B

ELECTRIC PROBE TECHNIQUES

B.1 INTRODUCTION

The existence of finite electric fields within sweep-
ing current sheets has been experimentally established by the
application of the double floating probe device [4,8,13,17].
The principles of operation and the application to the study of
current sheet structure can be considered well-known and will
not be repeated here. The unique aspect of such a measurement
in this study is that it will be made simultaneously with both
pressure and magnetic probes. Accordingly, the questions of
primary significance are those relating to the accuracy of
the measurement in both time and magnitude.

B.2 BASIC PERFORMANCE OF THE ELECTRIC PROBE

The floating double probe is a device that measures
the difference between floating potential at two points in a
plasma. To accomplish this measurement, two closely spaced
electrodes are allowed to float in the plasma with a signal
proportional to their difference being recorded. Specifically,
a conically shaped probe was used with a 2.5 mm diameter ring
electrode separated by a 1.85 mm gap from the second electrode
at the tip; electrode surface areas were equal. The components

of the system are shown in Fig. B-1. The design of the transformer and performance of that unit have been clearly outlined by Burton [13]. The frequency response and calibration of the circuitry with R = 0 was carried out with a square wave generator; frequency response was found to be satisfactory and the voltage reduction factor was 0.125.

While the probe circuit will produce a signal proportional to the difference of floating potential (V_f), the quantity of direct interest is the difference in plasma potential (V_p). The relationship between these two quantities is the difference in sheath potential drop (V_s), as

$$(V_{f_2} - V_{f_1}) = (V_{p_2} - V_{p_1}) + (V_{s_2} - V_{s_1})$$

The sheath potential drop will be of the order of kT_e/e; accordingly, with $kT_e(max) \approx 4$ ev, an electron temperature gradient greater than about 1 ev in 2 mm would not be expected. Such a temperature difference would be negligible compared to measured signals of about 20 volts in the center of the sheet. Accordingly, the local electric field will be evaluated as

$$E = -\nabla V \approx \frac{V_{f_2} - V_{f_1}}{\delta_E}$$

where δ_E is the electrode separation.

B.3 PERTURBATIONS OF ELECTRIC PROBE OUTPUT

The basic advantage of the double probe is that the currents drawn from the plasma are quite small in order to
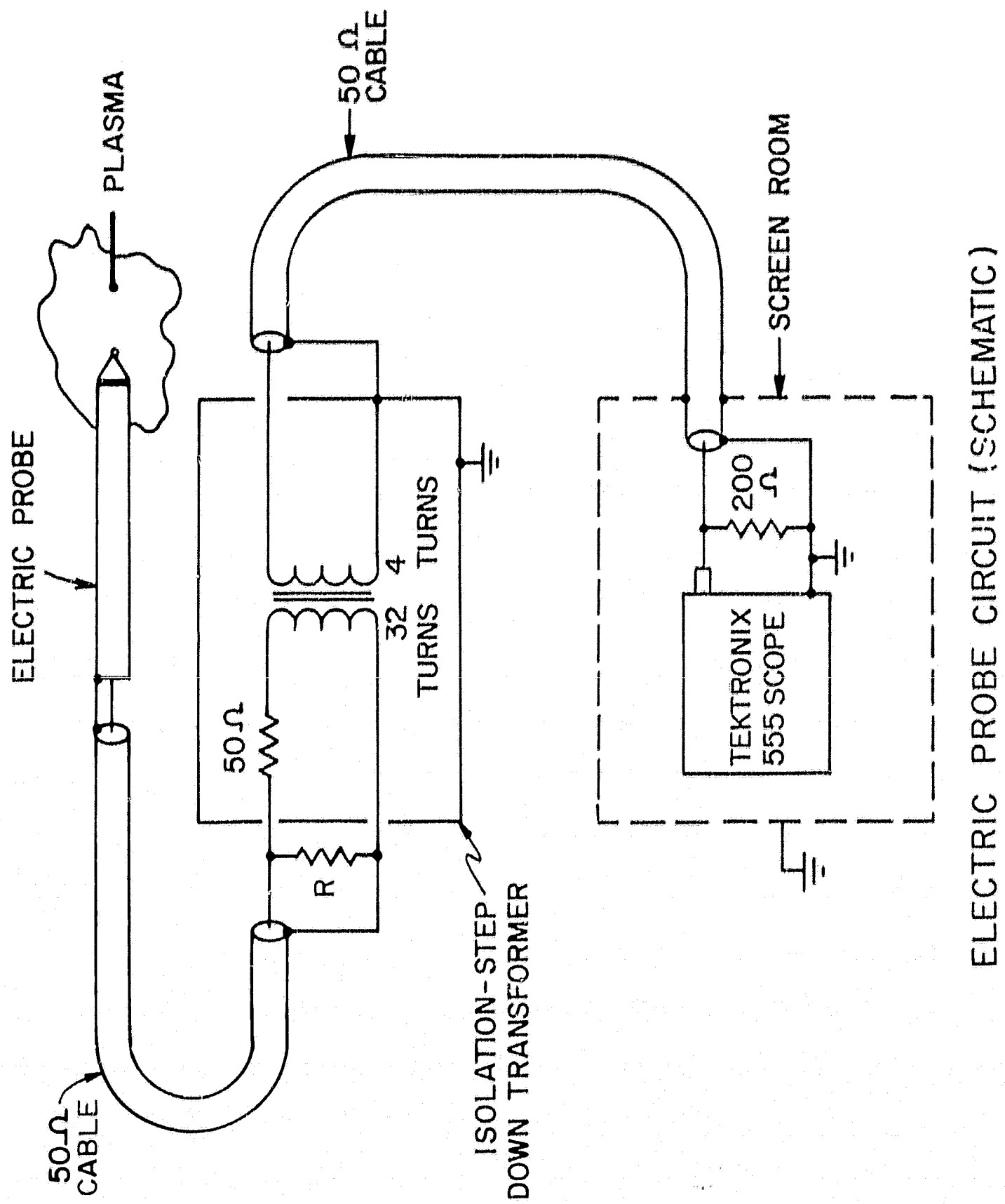
ELECTRIC PROBE CIRCUIT (SCHEMATIC)

FIGURE B-1

AP25-4055-66

avoid distortion of the medium. However, the finite size of
the probe may result in gasdynamic interaction as a serious
source of error. As a guide to interpretation of such effects,
the results of some preliminary work reported by Turchi [36]
are of interest. In a series of carefully executed experi-
ments, it was found that the indicated electric field signal
of a floating probe is dependent upon electrode separation
and on the shape of insulating surfaces surrounding the elec-
trodes. Specifically, for a conically shaped probe as used
in the present experiments, the electric field was found to
be lower than that obtained with small, spherical electrode
tips by a factor of up to 0.63. The trends noted in these
experiments will be useful in the evaluation of electric probe
data.

APPENDIX C

VOLTAGE PROBE TECHNIQUES

C.1 INTRODUCTION

The significance of voltage measurements in this
study lies in their direct relationship to energy deposi-
tion. Specifically, a knowledge of the resistive drop across
the current sheet allows an estimation of ohmic heating, and
a knowledge of the total drop across the chamber allows an
estimation of total energy supplied to the current sheet and
magnetic field system. For all voltage measurements that were
taken, a Tektronix type P6013 probe was connected to a termi-
nal from the chamber system and to the oscilloscope. A gen-
eral discussion of voltage probing principles has been pre-
sented in the literature [17] and a specific application to
the linear z-pinch is also available [13]; accordingly, the
emphasis in the present outline will be simply to indicate
the specific probing circuit.

C.2 EXTERNAL VOLTAGE MEASUREMENTS

The measurement of the total voltage drop across the
chamber (V_{ch}) was accomplished as indicated in Fig. C-1. For
this case, the voltage probe was connected to the lower elec-
trode of the discharge chamber and to the ground electrode.
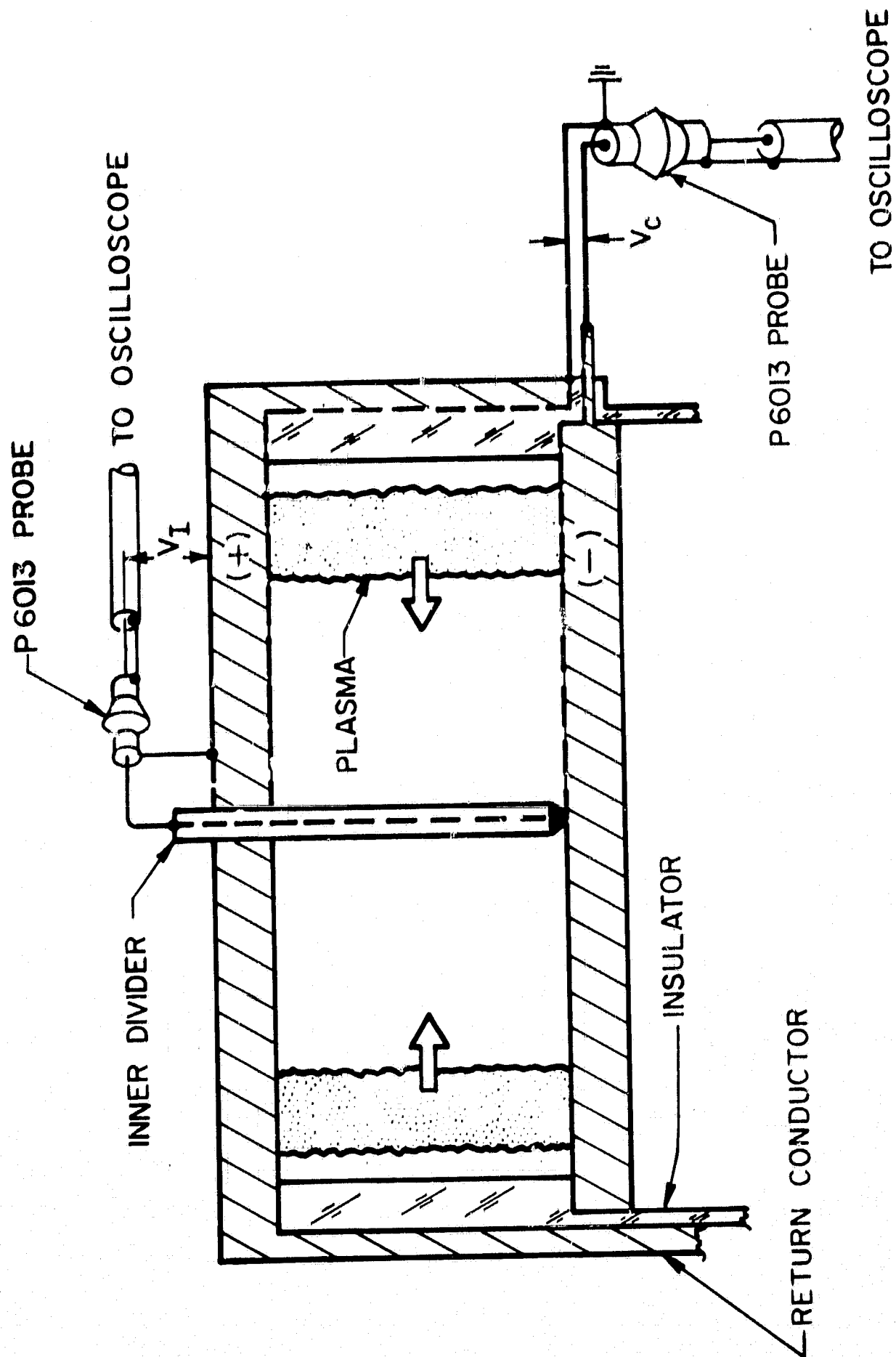
DISCHARGE VOLTAGE MEASUREMENTS

FIGURE C-1

The output signal was then proportional to the chamber voltage:

$$V_{ch} = \frac{d}{dt} (\varphi_{chamber} + \varphi_{insulator}) + IR_{plasma}$$

C.3   INNER DIVIDER VOLTAGE MEASUREMENTS

In order to measure the voltage drop across the current sheet, a metal rod with insulating covering was fitted through the outer electrode on the chamber axis to contact the inner electrode at one point (Fig. C-1). The probe was connected to the axial conducting rod and ground, so the circuit path was through the electrodes and current sheet and did not include any changing flux within its contours. Ideally the probe output was then proportional to plasma resistance, as:

$$V_I \approx IR_{plasma}$$

BIBLIOGRAPHY

1. M. Rosenbluth et al., "Infinite Conductivity Theory of the Pinch," Los Alamos Scientific Laboratory Rept. LA-1850, Los Alamos, N. Mex., 1954.

2. K. Hain et al., "Fully Ionized Pinch Collapse," Zeitschrift fur Naturforschung, Band 15a, Heft 12, 1960.

3. N. V. Fillipov, "Investigation of Pressures in a Powerful Pulsed Gas Discharge Using a Piezoelectric Measuring Device," vol. 3 of Plasma Physics and the Problems of Controlled Thermonuclear Reactions, Pergamon Press, Inc., New York, 1959.

4. L. C. Burkhardt and R. H. Lovberg, "Current Sheet in a Coaxial Plasma Gun," Phys. Fluids, vol. 5, March, 1962.

5. R. H. Lovberg, "Investigation of Current-sheet Microstructure," AIAA J., vol. 4, July, 1966.

6. G. C. Vlases, "Experiments in a Cylindrical Magnetic Shock Tube," J. Fluid Mech., vol. 16, 1963.

7. G. C. Vlases, "Shock and Current Layer Structure in an Electromagnetic Shock Tube," Phys. Fluids, vol. 10, November, 1967.

8. F. Y. Sorrell, "Current Sheet Dynamics in an Inverse Pinch Shock Tube," Phys. Fluids, vol. 11, May, 1968.

9. A. L. Hoffmann, "MHD Shock Production and Current Sheet Diffusion," Ph.D. thesis, Calif. Inst. of Tech., Pasadena, Calif., 1967.

10. R. G. Jahn and W. F. von Jaskowsky, "Current Distribution in Large-radius Pinch Discharges," AIAA J., vol. 2, October, 1964.

11. R. G. Jahn et al., "Current Pattern Stabilization in Pulsed Plasma Accelerators," (to be published) AIAA J., 1968.

12. N. A. Black, "Dynamics of a Pinch Discharge Driven by a High Current Pulse-forming Network," Ph.D. thesis, Dept. of Aerospace and Mechanical Sciences, Princeton Univ., Princeton, N. J., 1966.

13. R. L. Burton, "Structure of the Current Sheet in a Pinch Discharge," Ph.D. thesis, Dept. of Aerospace and Mechanical Sciences, Princeton Univ., Princeton, N. J., 1966.

14. W. R. Ellis, "An Investigation of Current Sheet Structure in a Cylindrical Z-Pinch," Ph.D. thesis, Dept. of Aerospace and Mechanical Sciences, Princeton Univ., Princeton, N. J., 1967.

15. R. G. Jahn, _Physics of Electric Propulsion_, McGraw-Hill Book Company, New York, 1968.

16. R. G. Jahn et al., "Gas-triggered Pinch Discharge Switch," Rev. Sci. Instr., vol. 36, January, 1965.

17. R. H. Huddlestone and S. L. Leonard, _Plasma Diagnostics_, Academic Press, Inc., New York, 1965.

18. "Pulsed Electromagnetic Gas Acceleration," 11th Semi-annual Progress Rept. No. 634j, Guggenheim Laboratories for the Aerospace Propulsion Sciences, Princeton Univ., Princeton, N. J., 1967.

19. T. G. Jones and G. C. Vlases, "Pressure Probes for Research in Plasma Dynamics and Detonation," Rev. Sci. Inst., vol. 30, August, 1967.

20. M. O. Stern and E. N. Dacus, "A Piezo-electric Probe for Plasma Research," Rev. Sci. Instr., vol. 32, p. 140, 1961.

21. R. M. Measures, "Acoustical Propagation of Thermally Induced Stresses," Acustica, vol. 15, March, 1965.

22. W. Katsaros, "Entwicklung and Erprobung Einer Hochauflosenden Piezoelektrischen Drucksonde," Institut für Plasmaphysik, IPP 1/46, March, 1966.

23. C. T. Chang, "Shock Wave Phenomena in Coaxial Plasma Guns," Phys. Fluids, vol. 4, September, 1961.

24. W. H. Rudderow, "Pressure Measurements in a Magnetically Driven Shock Tube," J. Appl. Phys., vol. 39, January, 1968.

25. T. F. Hueter and R. H. Bolt, Sonics, John Wiley & Sons, Inc., New York, 1955.

26. D. S. Johnson, "Design and Application of Piezoceramic Transducers to Transient Pressure Measurements," A. E. thesis, Calif. Inst. of Tech., Pasadena, Calif., 1963.

27. "Modern Piezoelectric Ceramics," Clevite Corp., Piezo-electric Division Bull. 9247, August, 1962.

28. S. Timoshenko and J. N. Goodier, Theory of Elasticity, 2nd ed., McGraw-Hill Book Company, New York, 1951.

29. H. Kolsky, Stress Waves in Solids, Oxford University Press, London, 1953.

30. H. Mirels and W. S. King, "Series Solution for Shock-tube Laminar Boundary Layer and Test Time," AIAA J., vol. 4, May, 1966.

31. R. E. Duff, "Shock-tube Performance at Low Initial Pressure," Phys. Fluids, vol. 2, March-April, 1959.

32. M. Friedman, "The Use of Piezoelectric Probes for Direct Measurement of Plasma Pressure," Plasma Phys., vol. 10, May, 1968.

33. H. V. Malmstadt et al., Electronics for Scientists, W. A. Benjamin, Inc., New York, 1962.

34. D. B. Henderson, "Aerodynamic Study of an Argon Plasma," Phys. Fluids, vol. 10, September, 1967.

35. G. G. Chernyi, Introduction to Hypersonic Flow, Academic Press, Inc., New York, 1961.

36. "Pulsed Electromagnetic Gas Acceleration," 12th Semi-annual Progress Rept. 634k, Guggenheim Laboratories for the Aerospace Propulsion Sciences, Princeton Univ., Princeton, N. J., 1968.

37. H. Petschek and S. Byron, "Approach to Equilibrium Ionization Behind Strong Shock Waves in Argon," Graduate School of Aeron. Eng., Cornell Univ., Ithaca, N. Y., 1955.

38. K. E. Harwell and R. G. Jahn, "Initial Ionization Rates in Shock-heated Argon, Krypton, and Xenon," Phys. Fluids, vol. 7, February, 1964.

39. "Pulsed Electromagnetic Gas Acceleration," 4th Semi-annual Progress Rept. 634c, Guggenheim Laboratories for the Aero-

space Propulsion Sciences, Princeton Univ., Princeton,
N. J., 1964.

40. L. Spitzer, Physics of Fully Ionized Gases, 2nd ed.,
Interscience Publishers, New York, 1962.

41. W. J. McCroskey, "An Experimental Model for the Sharp Lead-
ing Edge Problem in Rarified Hypersonic Flow," Dept. of
Aerospace and Mechanical Sciences Rept. 771, Princeton
Univ., Princeton, N. J., 1966.

42. K. S. Drellishak et al., "Partition Functions and Thermo-
dynamic Properties of Argon Plasma," AEDC-TDR-63-146,
August, 1963.

43. W. D. Hayes and R. F. Probstein, Hypersonic Flow Theory,
Academic Press, Inc., New York, 1959.

44. N. C. Freeman, "...Hypersonic Flow Past Plane and Axially
Symmetric Bluff Bodies," J. Fluid Mech, vol. 1, 1956.

45. D. Baganoff, "Experiments on the Wall-pressure History in
Shock-reflection Processes," J. Fluid Mech., vol. 23, 1965.

46. G. W. Sutton and A. Sherman, Engineering Magnetohydro-
dynamics, McGraw-Hill Book Company, New York, 1965.

47. K. F. Knoche et al., "Gas-plasma Research at the Institute
for Thermodynamics, Braunschweig," AGARD Rept. 320,
September, 1959.

48. K. F. Knoche, "Thermodynamics Charts for Argon Plasma Up
to 10^5 $^\circ$K With Illustrative Examples," ARL Rept. 171,
December, 1961.

49. M. Camac, "Argon Shock Structure," J. H. DeLeeuw (ed.),

vol. 1 in *Advances in Applied Mechanics*, supplement 3 of *Rarified Gas Dynamics*, Academic Press, Inc., New York, 1965.

50. J. A. Thornton, "Electric and Electromagnetic Shock Tubes," Anderson, et al. (eds.), in *Physico-Chemical Diagnostics of Plasmas*, Northwestern Univ. Press, Evanston, Ill., 1963.

51. C. K. Chu and R. A. Gross, "Shock Waves in Plasma Physics," Plasma Laboratory Rept. No. 41, Columbia Univ., New York, 1968.

52. R. B. Payne, "A Numerical Method for a Converging Cylindrical Shock," J. Fluid Mech., vol. 2, March, 1957.

53. R. F. Chisnell, "The Motion of a Shock Wave in a Channel, With Application to Cylindrical and Spherical Shock Waves," J. Fluid Mech., vol. 2, May, 1957.

54. C. Greifinger and J. D. Cole, "On Cylindrical MHD Shock Waves," Phys. Fluids, vol. 4, May, 1961.